COLLINEAR LASER SPECTROSCOPY OF NEUTRON-RICH NIOBIUM

by

MAREIKE RÜFFER

A thesis submitted to
The University of Birmingham
for the degree of
DOCTOR OF PHILOSOPHY

School of Physics and Astronomy
The University of Birmingham

May 21, 2010.

Abstract

Hyperfine structure spectra and isotope shifts of the neutron-rich nuclei ^{99}Nb, ^{101}Nb, ^{102}Nb and ^{103}Nb were obtained at the IGISOL (Ion Guide Isotope Separator On-Line) facility at the accelerator laboratory of the University of Jyväskylä. The data were taken using collinear laser spectroscopy of bunched beams. Optical pumping from the ground state to populate metastable atomic states in the ion beam cooler allowed efficient spectroscopy of the ionic system that would otherwise be inaccessible due to a lack of suitable ground state resonance lines. The measurements of the hyperfine structure and the isotope shifts contribute valuable nuclear information to the understanding of the $A \sim 100$ region which displays a sudden onset of deformation that cannot be explained by the single particle shell model. It was possible to confirm the spin assignments for ^{99}Nb, ^{101}Nb and ^{103}Nb as $I = 9/2$, $I = 5/2$ and $I = 5/2$ respectively. The extracted information on the mean square charge radii, $\delta\langle r^2\rangle$, the magnetic dipole moments, μ, and the electric quadrupole moments, Q, confirm a shape change of nuclei at $N = 60$ from soft and oblate (for $N < 60$) to more rigid and strongly prolate shapes (for $N \geq 60$).

Acknowledgements

When I came to the University of Birmingham as an exchange student I never thought that I would end up staying in this department for nearly six years - but after the warm welcome that I encountered in this friendly department staying was easy. In many ways these acknowlegements can not only include the people that were involved in and around my thesis but I have to thank everybody that was involved in my decision to stay here in Birmingham and who helped me settle in and in the end caused that I ended up writing this thesis.

During my time as a PhD student, I was very lucky to have had my supervisor Dr Garry Tungate and I would like to thank him from my heart for his guidance and support during all this time. My exploratory ways were never straight forward and whichever turn I decided to take I found myself supported and an open door whenever needed. I am very grateful to have had such a supervisor.

I also would like to thank Dr Dave H Forest for many fruitful discussions. How lucky to have his office right next door, a mine of knowledge hidden in the furthest corner of the building. It surely can't have been easy to accept that instead of pints at the bar he had to get me litres of tab water.

Over the last years, I was fortunate to have been involved in many interesting and fruitful experiments at the accelerator laboratory of the University of Jyväskylä in Finland, both on-line and off-line. I would like to thank everybody that was there, especially on the experiments when my data were taken. My thank you belongs especially to Prof Jon Billowes, Dr Paul Campbell and Dr Bradley Cheal from the University of Manchester and Dr Iain Moore from JYFL for expertise, card games, pints - and tab water.

I would like to thank Kasia, Mark and Richard for sharing the Birmingham office with me, for discussions and good times. Not to mention that I will miss the sound of Barrys guitar from next door. Thank you to everybody on the third floor of Physics East for the welcome after my viva.

Outside from physics I would like to thank my parents who enabled my studies abroad. I would like to thank the friends that have been there for me over the last time, Inga, Cornelia, my brother and everybody that I just haven't got the space to mention. I am very glad to have become part of the Crescent Theatre here in Birmingham and I will miss all my friends there and the crazy shows I have been part of, that took my mind off when a different angle on things was required.

I also would like to mention the EPSRC, the laser spectroscopy group and the University of Birmingham who have kindly funded my studies.

Contents

List of Figures

List of Tables

Chapter 1

INTRODUCTION

The nature and properties of atomic nuclei have been the subject of investigation for nearly one hundred years now. Since their discovery by Rutherford in 1911, much research has gone into establishing nuclear models by experimental and theoretical means.

The nuclear chart as it is known today consists of more than 3000 nuclei, of which only a tiny number are stable, and our understanding of them is still incomplete. A wide variety of experimental techniques have been developed over time, each contributing important measurements to broaden and to refine our understanding of nuclear behaviour across the nuclear chart. Experiments nowadays are usually carried out at large accelerator facilities such as CERN, GSI or Brookhaven National Laboratory. Also smaller scale sites such as the accelerator laboratory of the University of Jyväskylä, JYFL, Finland, a Centre of Excellence under the national centre of excellence program, have established a distinct reputation by carrying out world-class research.

The Collinear Laser Spectroscopy work at JYFL is carried out at the IGISOL (Ion Guide Isotope Separator On-Line) by a collaboration of the Universities of Birmingham, Manchester and Jyväskylä. Collinear Laser Spectroscopy investigates the change of nuclear size and shape across isotopic chains. The technique takes advantage of the fact that, as electrons have got a quantum mechanical probability

of being inside the atomic nucleus, the binding energies of the atomic electrons are influenced by the size of the nucleus. However, where the energies for electronic transitions are in the range of several electron volts, the shifts in the electronic binding energies from one isotope to another are less than one part in a million. By taking high-precision measurements of electronic transitions the effects of the changing nuclear size can be investigated using laser spectroscopic techniques. The change in the mean squared charge radius can be extracted in a model independent way from the isotopic shift in the measured transitions.

To a first approximation one would expect the change in mean square charge radius, $\delta\langle r^2\rangle$, to be a volume effect. As nuclear matter has been found to be incompressible, $\delta\langle r^2\rangle$ should be proportional to $A'^{2/3} - A^{2/3}$ where A' and A are the mass numbers of the heavier and the lighter nucleus respectively. Where this is not the case, nuclear deformation and nuclear shell effects have to be taken into account. The change in the nuclear mean squared charge radius itself can be interpreted in terms of static and dynamic nuclear deformation.

Another effect that is measured by Laser Spectroscopy is the hyperfine structure of atomic energy levels. This splitting of the levels is caused by interaction of the nucleus' electromagnetic field with the electromagnetic fields of the electrons. The effect of this interaction is of the same order of magnitude as the isotope shift and it is sensitive to the magnetic dipole moment and the electric quadrupole moment of the nucleus. The magnetic moment gives information about the single particle orbits inside the nucleus and is therefore sensitive to the shell structure. The electric quadrupole moment can be interpreted in terms of the static deviation of the nucleus from spherical shape.

Radioactive isotopes on either side of the nuclear valley of stability can be produced and investigated at the IGISOL. The often short-lived isotopes are created by colliding the high energy ion beam of a K-130 cyclotron with a target of sta-

ble atoms. Helium gas is used to extract the reaction products which are then accelerated along the beam line towards the interaction region where spectroscopic investigations take place. To prevent Doppler broadening spoiling the resolution of the atomic spectrum in question, several techniques along the laser beam-line are employed to reduce the energy spread; in particular the introduction of an ion-beam cooler allows a reduction of the energy spread to as little as 1 eV. A further minimisation is achieved by accelerating the ions along the collinear beam line up to 30 keV. The velocity spread of the ions in the direction of acceleration is now so small that the natural linewidth of the atomic transition is easily resolved by the collinearly incoming beam of a high-resolution dye laser.

In recent experiments, the Collinear Laser Spectroscopy Collaboration of the Universities of Birmingham and Manchester has paid particular attention to isotopes with $Z = 37 - 42$. At $N = 60$, ten neutrons after the shell closure at $N = 50$, a sudden change in systematics had been observed in both mass measurements [1, 2] and the change in mean squared charge radii of rubidium ($Z = 37$) [3] and strontium ($Z = 38$) [4], as well as B(E2; $2_1^+ \rightarrow 0_1^+$) rates [5]. The onset can be described as an increase in quadrupole-deformation and has been confirmed in zirconium ($Z = 40$) [6, 7], and yttrium ($Z = 39$) [8, 9]. Recent laser spectroscopic measurements of the molybdenum chain ($Z = 42$) [10] do not show the sudden onset of deformation in the mean squared charge radii at $N = 60$ but a very gradual increase in size from the $N = 50$ closed shell to a maximum value at $N = 66$.

Unfortunately, the investigation of the niobium chain ($Z = 41$) was not experimentally feasible with conventional laser spectroscopy due to the non-availability of suitable ionic transitions. The efficiency with which an ionic transition is measured in laser spectroscopy is determined by its transition strength and the initial population of the lower electronic level. Following the Boltzmann distribution, the electronic population in thermal equilibrium is naturally highest in the ground state

of any atomic system. For a long time, this circumstance restricted the technique to transitions from atomic ground states and very low lying excited states. Where suitable atomic ground state transitions are available this does not pose a problem, however, in niobium all but one ground state transition proved to be too short in wavelength in order to be accessible with the available dye laser system; and this one ground state transition proved too weak to be useful for spectroscopic purposes.

This was one motivation that led to the development of the optical pumping technique. A laser beam with a broad linewidth of 5 GHz is introduced into the ion beam cooler and optically pumps ions from the ground state into excited states. From there they de-excite through allowed decay branches and populate low lying metastable states as well as falling back to the ground state to be re-excited. This method allows one to artificially enhance the population of low-lying metastable states sufficiently to perform laser spectroscopic measurements from them. This newly developed technique significantly extends the scope of collinear laser spectroscopy at the IGISOL and allows one to access many atomic systems that were not manageable before. The application of the new technique had its premiere in the spin determination of ^{100}Y [11] and was used to measure the charge radii systematics of neutron-deficient niobium isotopes [11, 12].

In July 2008, Collinear Laser Spectroscopy was successfully performed on neutron-rich niobium isotopes at the IGISOL. The isotopes were produced via proton induced fission of uranium and the analysis of the isotope shifts and the hyperfine structures and the subsequent extraction of the change in mean squared charged radius, the magnetic dipole and electric quadrupole moments will be the subject of this thesis.

Chapter 2

THEORY

The data that are obtained by spectroscopic means are the isotope shift and the hyperfine structure of ionic transitions. An introduction to these terms is given below. It is also explained how they connect to the nuclear information that is extracted from them, namely the change in nuclear mean squared charge radius, the magnetic dipole moment, the electric quadrupole moment and the nuclear spin.

Nuclei are known to show single particle behaviour that is described by independent particle shell models. Nucleons outside filled shells are called valence nucleons and determine the spin of the nucleus. Nuclei with filled shells are known to be very stable and show a spherical shape that can be modelled well by the spherical shell model. Further information about the single particle motion of the nucleons in a nucleus can be retrieved from the interpretation of the magnetic moment of the nucleus. However, nuclear matter also shows collective behaviour and outside closed shells the collective motion of all nucleons leads to statically deformed nuclei. The deformation is quantified by the quadrupole moment and is incorporated in independent particle models such as the Nilsson model [13].

Laser spectroscopy deals with the charge radius of the nucleus rather than its matter radius. In most cases neutrons and protons are distributed equally in the nucleus and the charge and the matter distribution have nearly equal shape. The charge radius is thus directly affected by changes of the nuclear volume from one

isotope to another or by changes in the deformation. As nuclear matter is incompressible, a change in deformation will lead to an increase or decrease in the measured mean square charge radius.

2.1 The Hyperfine Structure

The hyperfine structure is a splitting of the atomic fine structure levels, caused by the interactions of the nucleus with the electrons. On the nuclear side, the interaction is governed by the magnetic dipole moment μ and the electric quadrupole moment Q. Higher order terms have been found to be mostly negligible [14].

Following the classical idea, a static dipole moment is produced from current loops. The current I produced by an orbiting proton with charge e over the time T of one orbit is

$$I = \frac{e}{T} = e\frac{\omega}{2\pi} \tag{2.1}$$

where ω is the angular frequency. The magnetic moment μ_l through the area $A = \pi r^2$ which is enclosed by the current loop is

$$\mu_l = AI = r^2 e\omega/2 \tag{2.2}$$

The magnitude of the orbital angular momentum l of the proton with mass m_p is

$$l = m_p \omega r^2 \tag{2.3}$$

Combining μ_l and l and using the eigenvalue for the quantum mechanical angular momentum $l\hbar$:

$$\mu_l = \frac{e\hbar}{2m_p} l \tag{2.4}$$

In the nucleus, the orbital magnetic moment $\boldsymbol{\mu_l}$ and the spin magnetic moment

$\boldsymbol{\mu_s}$ combine vectorially to give the magnetic moment

$$\boldsymbol{\mu_j} = \boldsymbol{\mu_l} + \boldsymbol{\mu_s} \tag{2.5}$$

In the nucleus, the orbital angular momentum $\mathbf{l}$ and the spin $\mathbf{s}$ of a single nucleon combine to give the angular momentum $\mathbf{j} = \mathbf{l} + \mathbf{s}$. Vectorial summation over all nucleons gives then the total angular momentum of the nucleus $\mathbf{I} = \sum \mathbf{j}$. This modifies equation (2.5) to

$$\boldsymbol{\mu_j} = g_l \mathbf{l} + g_s \mathbf{s} \tag{2.6}$$

where g_l and g_s are the g-factors of the orbital angular momentum and the spin respectively. Due to the g-factors, the total magnetic moment $\boldsymbol{\mu}$ of the nucleus and the spin $\mathbf{I}$ are not parallel. However, the magnetic moment precesses around the nuclear axis $\mathbf{I}$ and the only component that is not averaged out is the component $\boldsymbol{\mu_I}$ along the nuclear spin direction $\mathbf{I}$ [15]

$$\boldsymbol{\mu_I} = g_I \mathbf{I} \tag{2.7}$$

The nuclear magnetic dipole moment is sensitive to the contributions of single particle orbits of the protons. As neutrons are not charged, there will be no orbital contribution to the dipole moment and $g_l = 0$ for a neutron, whereas $g_l = 1$ for protons. Both the proton and the neutron have spin contributions to the total magnetic moment which indicates their underlying quark structure ($g_s(\mathrm{p}) = 5.5858$, $g_s(\mathrm{n}) = -3.8261$).

Quantum mechanically, the expectation value $\langle \mu \rangle$ of the magnetic dipole moment operator $\boldsymbol{\mu}$ for a nucleon can be expressed as

$$\langle \mu \rangle = \int \Psi^*(r', m = I)\ \boldsymbol{\mu}\ \Psi(r', m = I) dv' \tag{2.8}$$

where Ψ is the wave function of the respective nucleon and the integration is over the full nuclear volume. Per definition the magnetic moment is measured for maximum projection onto an arbitrary z-axis of the nucleus.

In the spherical shell model, valence nucleons are seen as single particles outside an inert core. Due to the strong pairing force, the magnetic moment of every two identical nucleons should be equal and opposite, so that the value of the total magnetic moment of the nucleus is determined by the last unpaired nucleon. This value can be estimated and was first done so by Schmidt in 1937 [16]. For a single nucleon in a spherical shell model configuration, the total angular momentum of a single nucleon with orbital angular momentum l and spin 1/2 is $j = l \pm s$. The Schmidt estimate is calculated as follows

$$\begin{aligned} \langle\mu\rangle &= [g_l(j-1/2)+1/2g_s]\mu_N \qquad \text{for} \qquad j = l+1/2 \\ \langle\mu\rangle &= [g_l\frac{j(j+3/2)}{(j+1)} - 1/2\frac{j}{j+1}]\mu_N \qquad \text{for} \qquad j = l-1/2 \end{aligned} \tag{2.9}$$

where μ_N is the nuclear magneton. For odd-odd nuclei, the vector sum of the moments of the odd neutron and the odd proton are taken since

$$g_1\mathbf{j_1} + g_2\mathbf{j_2} = g_J\mathbf{I} = \boldsymbol{\mu_I} \tag{2.10}$$

Experimentally, the measured value of the magnetic moment can be considerably different from the Schmidt-estimate. This is due to a mixture of quantum mechanical states in single particle levels and contributions from "core" nucleons. An example for the quantum mechanical mixing of states is the deuteron, where 4% of a d-wave is required to explain the experimental value of the magnetic moment. For a full explanation see [13].

In order to measure the magnetic moment of the nucleus by probing atomic elec-

trons, an interaction energy needs to exist between the two. This interaction energy is caused by the interaction of the nuclear magnetic moment with the magnetic field $\mathcal{B}_e$ of the electrons at the nucleus. The interaction Hamiltonian is

$$\hat{\mathcal{H}} = -\boldsymbol{\mu_I} \cdot \mathcal{B}_e \tag{2.11}$$

As the magnetic moment μ is proportional to nuclear spin I (equation (2.7)) and the magnetic field of the electrons is proportional and anti-parallel to the total angular momentum of the electrons J, the Hamiltonian can be re-written as

$$\hat{\mathcal{H}} = A\mathbf{I} \cdot \mathbf{J} \tag{2.12}$$

where

$$A = \frac{\mu_I B_e}{IJ} \tag{2.13}$$

and $\mathbf{I}$ and $\mathbf{J}$ are the vectors of the nuclear spin and the electronic total angular momentum respectively and they do not commute with $\hat{\mathcal{H}}$. $\mathbf{I}$ and $\mathbf{J}$ couple vectorially to a total angular momentum $\mathbf{F}$, causing a splitting of the atomic fine structure levels.

Thus

$$\begin{aligned} \mathbf{F} &= \mathbf{I} + \mathbf{J} \\ \therefore \mathbf{F}^2 &= \mathbf{I}^2 + \mathbf{J}^2 + 2\mathbf{I} \cdot \mathbf{J} \\ \Rightarrow \mathbf{I} \cdot \mathbf{J} &= \frac{1}{2}(\mathbf{F}^2 - \mathbf{I}^2 - \mathbf{J}^2) \end{aligned} \tag{2.14}$$

The quantum mechanical expectation value of $\mathbf{I} \cdot \mathbf{J}$ is found using their associated quantum numbers I, J and F

$$\langle \mathbf{I} \cdot \mathbf{J} \rangle = \frac{1}{2}[F(F+1) - I(I+1) - J(J+1)] \tag{2.15}$$

The energy ΔE_{HFS} of the hyperfine interaction is the expectation value of the Hamiltonian $\hat{\mathcal{H}}$

$$\begin{aligned} \Delta E_{HFS} &= \langle \hat{\mathcal{H}} \rangle = A \langle \mathbf{I} \cdot \mathbf{J} \rangle \\ \Delta E_{HFS} &= \frac{A}{2}[F(F+1) - I(I+1) - J(J+1)] = A\frac{K}{2} \end{aligned} \tag{2.16}$$

where $K = F(F+1) - I(I+1) - J(J+1)$. F can take on all values from $|I-J| \leq F \leq |I+J|$ in integer steps and thus determines the number of resulting hyperfine levels.

In atoms, where nuclei have spin $I > 1/2$ and electronic energy levels have angular momentum $J > 1/2$, an additional interaction allows the measurement of the electric quadrupole moment, Q_s, of the nucleus. As the nucleus is usually rotating in the lab frame, it is the spectroscopic quadrupole moment Q_s that interacts with the gradient of the electric field created by the electrons at the nucleus $\langle \frac{\partial^2 V}{\partial z^2} \rangle$, where V is the electric potential.

The Hamiltonian of the interaction energy between the nuclear quadrupole moment and the electric field gradient is [17]

$$\hat{\mathcal{H}} = eQ_s \left\langle \frac{\partial^2 V_e}{\partial z^2} \right\rangle \frac{[3(\mathbf{I}\cdot\mathbf{J})^2 + \frac{3}{2}\mathbf{I}\cdot\mathbf{J} - I(I+1)J(J+1)]}{2I(2I-1)(2J-1)} \tag{2.17}$$

where $\mathbf{I}$ and $\mathbf{J}$ are the operators of the nuclear spin and the total atomic angular momentum respectively, while I and J are their respective eigenvalues. The magnitude of the quadrupole interaction is usually smaller than the dipole interaction.

Via projection, the intrinsic quadrupole moment, Q_0, of the nucleus can be inferred from the spectroscopic quadrupole moment Q_s. The intrinsic electric quadrupole moment stems from a non-spherical charge distribution of the nucleus. A small contribution can arise from a single valence proton orbiting outside a spherically

symmetric nucleus. Large quadrupole moments arise from collective motion of all nucleons and the nucleus would then be seen as statically deformed. Statically deformed nuclei occur in mid-shell regions.

Quantum mechanically the expectation value Q_0 of the intrinsic quadrupole moment can be obtained from the quadrupole operator

$$eQ_0 = \sum_{i=1}^{Z} e \int \Psi^*(3z_i^2 - r_i^2)\Psi \; d\nu \tag{2.18}$$

where Ψ is the collective wave function of the protons and the integral is over the whole nuclear volume.

Here, the nuclear symmetry axis is taken to be in the z-direction. For a spherical charge distribution the quadrupole moment would vanish as $r^2 = x^2 + y^2 + z^2$ and $x^2 = y^2 = z^2$, therefore $3z^2 - r^2 = 0$. For a particle orbiting in the xy-plane, $z^2 = 0$ and $Q_0 \propto -r^2$ giving a negative quadrupole moment which corresponds to an oblate deformed nucleus. A positive quadrupole moment corresponds to a prolate deformed nucleus.

The spectroscopic quadrupole moment Q_s is connected to the intrinsic quadrupole moment Q_0 of the nucleus via the nuclear spin I and Ω

$$Q_s = Q_0 \frac{3\Omega^2 - I(I+1)}{(I+1)(2I+3)} \tag{2.19}$$

where Ω is the projection of the spin onto the intrinsic nuclear symmetry axis. Normally, $\Omega = I$ for ground state nuclei and long lived isomers, but $\Omega \neq I$ for excited nuclear states that involve rotational energy.

The total interaction energy of the hyperfine splitting can be summarized as

$$E_{HFS} = \frac{A}{2}K + \frac{B}{4}\frac{\frac{3}{2}K(K+1) - 2I(I+1)J(J+1)}{I(2I-1)J(2J-1)} \tag{2.20}$$

where A is defined in eqn (2.13) and K in eqn (2.16) and

$$B = eQ_s\langle\frac{\partial^2 V}{\partial z^2}\rangle \tag{2.21}$$

Figure 2.1 shows how a fine structure level splits into several hyperfine structure components under the influence of the electron-nuclear interaction. Experimentally, transitions between electronic levels are being measured and instead of measuring the transition between two fine structure levels, transitions are now possible between a range of non-degenerate hyperfine structure levels, leading to a stretched out spectrum of several hyperfine structure peaks.

The number of peaks seen in such a case is determined by the selection rules. Transitions of $\Delta F = 0, \pm 1$ are allowed between the hyperfine levels of two different fine structure levels with the exception of $F = 0 \rightarrow F = 0$. As well as the number of components, I, J and F also govern the relative intensities of the observed transition peaks [18]. The absolute magnitude of the splitting is determined by the interval factors A, eqn (2.13), and B, eqn (2.21), and is typically between a few hundred MHz and a few GHz. The frequency shift $\delta\nu_i$ of one hyperfine component i relative to the unsplit centroid frequency ω - which would be existent without the hyperfine interactions - is given by

$$\delta\nu_i = f^u_{1,i}A^u + f^u_{2,i}B^u - f^l_{1,i}A^l - f^l_{2,i}B^l \tag{2.22}$$

Here $A^{u,l}$ and $B^{u,l}$ are the interval factors of the upper level u and the lower level l and [19]

$$\begin{aligned} f^j_{1,i} &= \frac{F^j_i(F^j_i+1) - J^j(J^j+1) - I(I+1)}{2} = \frac{K^j_i}{2} \\ f^j_{2,i} &= \frac{3/2K^j_i(K^j_i+1) - 2I(I+1)J^j(J^j+1)}{4I(2I-1)J^j(2J^j-1)} \end{aligned} \tag{2.23}$$

are functions of the angular momentum that determine the relative splitting of the hyperfine levels in one energy level and $j = u, l$. Using measurements of the hyperfine structure, it is usually possible to extract the nuclear spin as well as the magnetic dipole moment and the electric quadrupole moment.

Figure 2.1 shows the hyperfine structure of a transition in stable ionic niobium. The nuclear spin is $I = 9/2$ and $J = 1$ in the lower and $J = 1$ in the upper level. This leads to the seven hyperfine structure peaks that are displayed in the spectrum. The hyperfine coefficients A and B (eqn (2.13) and eqn (2.21) respectively) are the observables and the magnetic moment and quadrupole moment can be determined for an unstable nucleus N' if a value for the stable isotope N is known. In this case

$$\frac{A^N_{u,l}}{A^{N'}_{u,l}} = \frac{\mu^N/I}{\mu^{N'}/I} \tag{2.24}$$

which allows $\mu^{N'}$ to be extracted. Similarly

$$\frac{B^N_{u,l}}{B^{N'}_{u,l}} = \frac{Q^N}{Q^{N'}} \tag{2.25}$$

In 1950, Bohr and Weisskopf [20] discovered that the ratio A_i/A_j is not as constant as would be expected from equation (2.24), as it assumes that both nuclei are point dipoles. Bohr and Weisskopf showed that the anomaly can be accounted for if the magnetic moments are allowed to be some distribution of magnetism over the whole nuclear volume rather than a point dipole. As the nuclear magnetic moment is probed by the electronic wave function, a magnetic moment that is smeared out over the whole nuclear volume would have a measurable effect. However, the electronic wave function has to have a high density at the nucleus itself which is the case for s- and $p_{1/2}$-wave functions. The extended magnetisation will lead to a changed

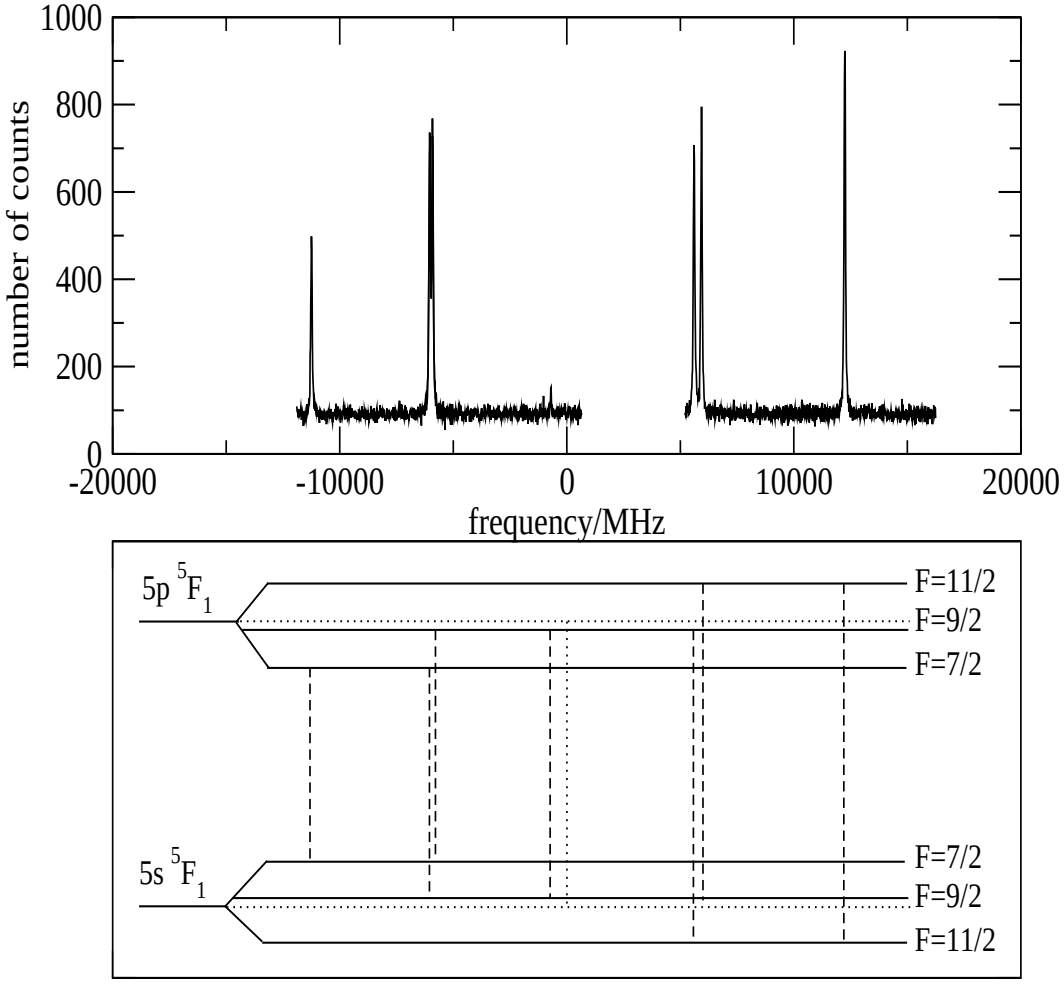

Figure 2.1: Top: Hyperfine structure of the 5s $^5F_1$ (2356.760 cm^{-1}) $\rightarrow$ 5p $^5F_1$ (36731.790 cm^{-1}) transition at 290.8237 nm in ^{93}Nb, I=9/2. Bottom: The atomic level structure leading to the observed hyperfine structure. The fine structure level is represented by the horizontal dotted line. The centroid of the transition is represented by the vertical dotted line.

hyperfine constant

$$A = \frac{\mu_I(1-\epsilon)B_e}{IJ} \tag{2.26}$$

where

$$\epsilon \simeq -(ZR_0/a_0)(a_0/2ZR_0)^{2(1-\rho)}(R^2/R_0^2)_{Av} \tag{2.27}$$

here, a_0 is the Bohr radius, R_0 is the nuclear radius, $\rho = (1-Z^2\alpha^2)^{1/2}$ and α is the fine structure constant. The effect of the hyperfine structure anomaly is usually less than 1% and is negligible in lighter atoms. Experimentally, a deviation of 0.33% has been measured in rubidium [21].

2.2 The Isotope Shift

Isotope shifts are shifts in the transition frequency of the same electronic transition along an isotopic chain. However, whereas the transition energy is in the range of eV, the energy perturbations causing the isotope shifts lie in the order of 10^{-6} eV.

If ν is the frequency of the particular transition, then the isotope shift $\delta\nu$ between two isotopes A and A' can be written as

$$\delta\nu^{A,A'} = \nu^{A'} - \nu^{A} \tag{2.28}$$

There are two different contributions to the isotope shift in a transition: the mass shift $\delta\nu_{MS}^{AA'}$ and the field shift $\delta\nu_{FS}^{AA'}$. The field shift gives information about the change in the mean square charge radius $\delta\langle r^2\rangle$, whereas the mass shift contains no information about nuclear structure but needs to be evaluated as part of the isotope shift. To a good approximation the isotope shift can be given by [22]

$$\delta\nu^{A,A'} = \delta\nu_{MS}^{A,A'} + \delta\nu_{FS}^{A,A'} \tag{2.29}$$

The Mass Shift

The mass shift can be expressed as

$$\delta\nu_{MS}^{A,A'} = (\frac{A'-A}{AA'})M \tag{2.30}$$

where M is the isotope independent mass shift and $(\frac{A'-A}{AA'})$ is the mass factor. Together they form the mass shift $\delta\nu_{MS}^{AA'}$ for an isotope pair [22].

The mass shift consists of the normal mass shift $\delta\nu_{NMS}$ and the specific mass shift $\delta\nu_{SMS}$ and can be written as

$$\delta\nu_{MS} = \delta\nu_{NMS} + \delta\nu_{SMS} \tag{2.31}$$

which can be obtained from energy considerations: The kinetic energy operator $\hat{\mathcal{T}}$ of an atom can be defined as

$$\hat{\mathcal{T}} = \frac{\hat{p}_n^2}{2m_n} + \sum_i \frac{\hat{p}_i^2}{2m_e} \tag{2.32}$$

where p_n and m_n are the momentum and mass of the nucleus and p_i and m_e are those of the electrons. For a stationary atom, momentum will be conserved and $p_n + \sum p_i = 0$. Therefore

$$\begin{aligned} \hat{\mathcal{T}} &= \frac{(-\sum \hat{p}_i)^2}{2m_n} + \sum_i \frac{\hat{p}_i^2}{2m_e} \\ &= \frac{\sum_i \hat{p}_i^2}{2m_n} + \frac{2\sum_{ij} \hat{p}_i \hat{p}_j}{2m_n} + \sum \frac{\hat{p}_i^2}{2m_e} \\ &= \frac{1}{2}\frac{m_n + m_e}{m_n m_e} \sum_i \hat{p}_i^2 + \frac{1}{m_n} \sum_{ij} \hat{p}_i \hat{p}_j \end{aligned} \tag{2.33}$$

The first term in eqn (2.33) corresponds to the normal mass shift $\delta\nu_{NMS}$. The normal mass shift occurs due to the fact that the nucleus does not have an infinite mass and therefore, the nucleus and the electrons rotate around a common centre of mass [23]. Hence, the $\delta\nu_{NMS}$ represents the change in recoil kinetic energy of the nucleus [22] with a single orbiting electron. It contributes a fixed percentage to the energy of each atomic level in the atom and can be calculated exactly.

The second term, the specific mass shift $\delta\nu_{SMS}$, arises from correlations between the electrons in the atom. These correlations are dependent on the configuration of the level concerned and hence, on the wave functions of the electrons [23]. Analytically the specific mass shift can be calculated accurately if the wave functions of the electrons are known. This is the case only for very light atoms up to beryllium [24]. In heavier atoms the specific mass shift can be determined experimentally using the King Plot technique (see section 5.4).

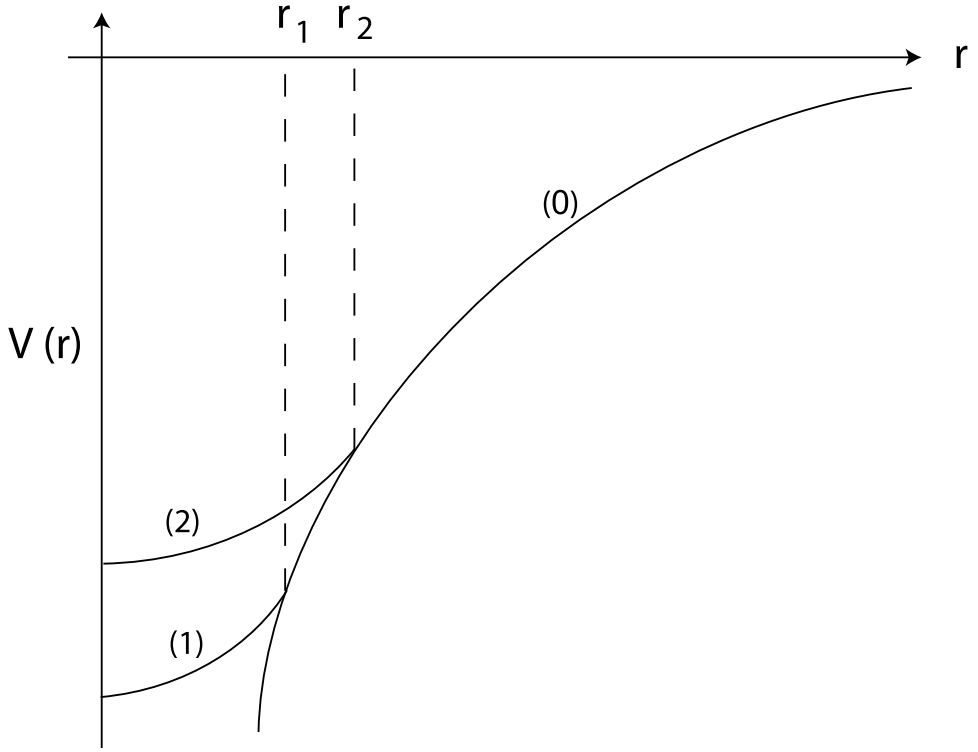

Figure 2.2: Coulomb potential of a point like nucleus (0) and two finite sized nuclei (1) and (2) with radii r_1 and r_2 respectively and $r_2 > r_1$ [56]

In a level, the specific mass shift is usually small compared to the value of the normal mass shift and can be treated as a perturbation [23]. However, in a transition it can be several times bigger than the normal mass shift. As the transition only picks up the differential change in the two level shifts, the normal mass shift which is of the same order of magnitude in both levels partially cancels.

The Field Shift

The field shift arises from the fact that a real nucleus has got a finite size and the often used infinitely deep Coulomb potential of a point like nucleus is not applicable.

In general the protons and neutrons will occupy a larger volume in a heavier isotope [23] and the Coulomb potential which interacts with the electrons has to be modified (Figure 2.2).

The spatially extended mean squared charge radius of the atomic nucleus can be obtained directly from the nuclear charge distribution $\rho(r)$ by

$$\langle r^2 \rangle = \frac{\int_0^\infty \rho(r) r^2 dV}{\int_0^\infty \rho(r) dV} \tag{2.34}$$

The extended charge distribution weakens the binding potential for electrons in the nuclear region, leading to a small energy shift δE_{FS} from one isotope to another in the respective electronic energy level [25]

$$\delta E_{FS} = \pi \frac{a_0^3 h}{Z} |\Psi(0)|^2 f(Z) \delta \langle r^2 \rangle^{AA'} \tag{2.35}$$

This shift is determined by the non-relativistic probability density of the electron at the nucleus $|\Psi(0)|^2$ and the change in the mean squared charge radius $\delta\langle r^2 \rangle$ i.e. the electrostatic interaction between the nucleus and the electron. a_0 is the Bohr radius, Z is the atomic number and $f(Z)$ is a known function that increases with Z and that contains corrections due to relativistic effects and the finite size of the nucleus.

For the field shift to be seen in a transition, the change of the electron density at the nucleus $\Delta|\Psi(0)|^2$ has to be looked at. This leads to the usual expression for the relativistic frequency shift in a transition [26, 27]

$$\delta \nu_{FS} = \underbrace{\frac{\pi a_0^3}{Z} \Delta |\Psi(0)|^2 f(Z)}_{=F} \delta \langle r^2 \rangle \tag{2.36}$$

The field shift will be biggest for a transition which involves a big change of electron density at the nucleus, namely an s-electron going to a p-state [22], as an s-electron has got a relatively large probability of being inside the nucleus whereas the electronic density at the nucleus is negligible for a $p_{3/2}$-electron. However, the change in electron density at the nucleus $\Delta|\Psi(0)|^2$ is always the total change and

has additional contributions from other electrons that are affected from a change in screening from the nucleus as the atom changes state.

The field shift also increases with increasing Z. This is accounted for by the relativistic correction function $f(Z)$ and is also implicit from $\Delta|\Psi(0)|^2$ as electrons will have an increased nuclear density in higher Z nuclei. (The attraction is stronger and the wave function is drawn in.) The total isotope shift will then be dominated by the field shift. In the intermediate region around $Z \simeq 40$ the mass shift and the field shift will be of similar size.

The field shift can now be written as a product of electronic and nuclear information

$$\delta\nu_{FS}^{AA'} = F \times \delta\langle r^2\rangle^{A,A'} \tag{2.37}$$

where F is known as the electronic factor.

This expression has to be amended for heavier elements as the increased electron energy makes the electrons more sensitive to the nuclear shape. Therefore higher order terms of the nuclear charge distribution need to be taken into account and $\delta\langle r^2\rangle$ is replaced by $\lambda^{AA'} = \delta\langle r^2\rangle^{AA'} + \frac{C_2}{C_1}\delta\langle r^4\rangle^{AA'} + \frac{C_3}{C_1}\delta\langle r^6\rangle^{AA'} + ...$ This was first done by Seltzer [28] and $\lambda^{AA'}$ is called the Seltzer moment. The ratios C_i/C_1 are tabulated factors that were re-calculated by Blundell [29].

2.3 The mean square charge radius

Absolute charge radii of stable isotopes are usually obtained through electron scattering and from electronic K X-ray or muonic X-ray data [30]. These methods are sensitive to different quantities of the nuclear charge distribution. Elastic electron scattering is able to reveal the nuclear charge distribution $\rho(r)$. Electronic K X-rays give the difference in mean square charge radius $\delta\langle r^2\rangle$ between isotopes but are lim-

ited in their energy resolution. Muonic X-rays give a quantity called the Barrett moment $\langle r^k e^{-\alpha r} \rangle$ which takes into account the change of the muonic wave function across the nuclear volume [31]. Combined, these methods give a valuable calibration for absolute nuclear charge radii. However, all these methods require the availability of bulk target material and can only be used for stable or very long lived isotopes. They are unsuitable for short-lived isotopes which is why laser spectroscopy is so very useful. By using absolute charge radii as a calibration, laser spectroscopy can extend the systematics of charge radii in isotopic chains a long way into neutron-rich and neutron deficient regions.

The change in the mean square charge radius from one isotope to another can be ascribed to two effects: Obviously the addition of neutrons will alter the volume of the nucleus. However, even at constant volume a deviation of the nucleus from a spherical shape can change the measured mean square charge radius $\langle r^2 \rangle$. A deviation from a spherical shape is usually expressed in the form of the spherical harmonics. For a simple uniform charge distribution with a sharp surface, the shape deviation would be accounted for as

$$r = r_{sph}(1 + \sum \beta_i Y_i^0) \tag{2.38}$$

where Y_i^0 are the spherical harmonics, β_i are their coefficients and r_{sph} is the radius of a spherical nucleus with the same volume. Using eqn. (2.34), the mean square charge radius can now be obtained by integration over the whole space

$$\langle r^2 \rangle \simeq \langle r^2 \rangle_{sph}(1 + \frac{5}{4\pi} \sum_i \langle \beta_i^2 \rangle) \tag{2.39}$$

The quadrupole deformation parameter β_2 is dominant in the $Z \simeq 40$ region and higher orders in i can be neglected.

As a real nuclear surface possesses a diffuse edge, this needs to be taken into

account. The Helm model proposes folding a sharp edged distribution with a Gaussian one which increases the total $\langle r^2 \rangle$ by a term of $\Delta\langle r^2 \rangle = 3\sigma^2$. Here, σ is the width of the Gaussian distribution. The mathematical advantage is that all multipole moments of $\rho(r)$ are independent of σ and eqn (2.38) and (2.39) can be used unchanged for the evaluation of $\langle r^2 \rangle$ [27].

For the differential change in the mean square charge radius eqn (2.39) translates into

$$\delta\langle r^2 \rangle = \delta\langle r^2 \rangle_{sph}(1 + \frac{5}{4\pi}\sum\langle\beta_i^2\rangle) + \frac{5}{4\pi}\langle r^2 \rangle_{sph}\sum\delta\langle\beta_i^2\rangle \tag{2.40}$$

where the first term of the sum accounts for the change in volume for two nuclei with the same deformation; and the second shows the effect on $\delta\langle r^2 \rangle$ due to a change in deformation.

2.3.1 Nuclear Deformation

The deformation of the nucleus can be dynamic as well as static in nature, allowing a deformed nucleus to vibrate around its equilibrium shape. Deformed nuclei have got a non-spherical equilibrium shape [13], but also fluctuations around the zero-point can affect the observed nuclear radius.

The quadrupole deformation parameter β_2 is defined as the coefficient of the spherical harmonic $Y_2^0 = (5/16\pi)^{1/2}(3\cos^2\theta - 1)$ in eqn (2.38). This spherical harmonic describes a quadrupole deviation of the nucleus from a spherically symmetric shape. The nucleus can be statically deformed leading to static moments, but independently from that it can also show an instantaneous dynamic deformation. Therefore the deformation parameter can be written as a sum of static and dynamic contributions: $\beta_2 = \beta_{2,st} + \beta_{2,dyn}$. Thus, $\beta_{2,st}$ will just be a constant coefficient whereas $\beta_{2,dyn}$ has a time-dependence. For a vibrating nucleus, a single point on the nuclear surface can be seen as carrying out harmonic motion about its equilibrium position. Figure (2.3) illustrates the interplay of the static and the dynamic component of the deformation parameter.

For the mean square charge radius, β_2 is squared and

$$\beta_2^2 = \beta_{2,st}^2 + \beta_{2,dyn}^2 + 2\beta_{2,st}\beta_{2,dyn} \tag{2.41}$$

Averaging over time gives

$$\langle\beta_2^2\rangle = \langle\beta_{2,st}^2\rangle + \langle\beta_{2,dyn}^2\rangle \tag{2.42}$$

revealing that the expression for the mean squared charge radius contains information about both static and dynamic deformation. As $\beta_{2,st}$ is constant, $\langle\beta_{2,st}^2\rangle \equiv \langle\beta_{2,st}\rangle^2$.

Similarly the quadrupole moment Q_0 can be connected to the deformation pa-

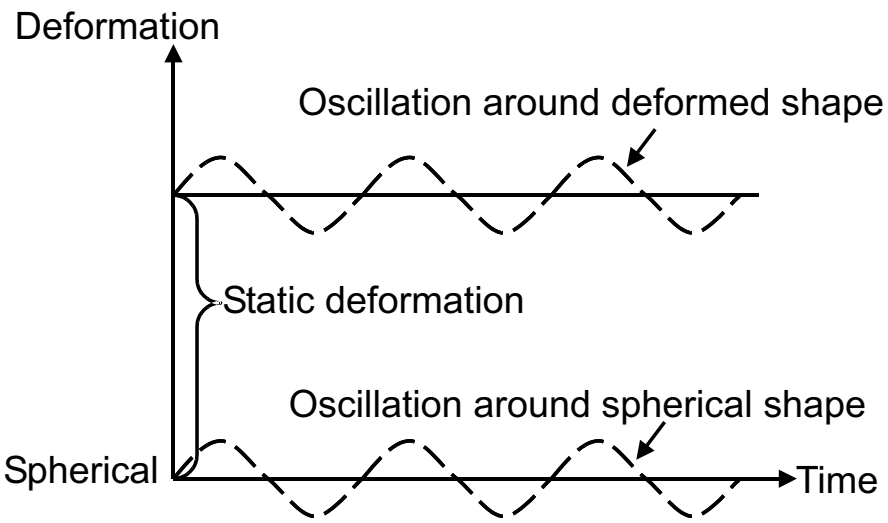

Figure 2.3: The two components of the deformation parameter β_2: static and dynamic.

rameter $\langle\beta_2\rangle$

$$Q_0 \approx \frac{5Z\langle r^2\rangle_{sph}}{\sqrt{5\pi}}\langle\beta_2\rangle(1+0.36\langle\beta_2\rangle) \tag{2.43}$$

where $\langle\beta_2\rangle$ contains only information about static deformation. $\langle r^2\rangle_{sph}$ is the mean square charge radius of a spherically symmetric nucleus. A nucleus with an average spherical shape would possess $\langle\beta_2\rangle = 0$.

Experimentally, the evaluation of the change in the mean square charge radius and the quadrupole moment can give not only information about a permanent deformation from spherical shape, but also about the rigidity of the nucleus. For very rigid nuclei $\langle\beta^2_{2,dyn}\rangle$ is expected to be small and $\langle\beta^2_2\rangle \simeq \langle\beta^2_{2,stat}\rangle$. In this case $\langle\beta^2_2\rangle$ in equation (2.39) can be replaced by $\langle\beta_2\rangle^2$.

In soft nuclei, $\langle\beta^2_{2,dyn}\rangle$ will make up a substantial amount of $\langle\beta^2_2\rangle$ and $\langle\beta^2_2\rangle > \langle\beta^2_{2,stat}\rangle$. This is known as β-softness. Microscopic calculations in rubidium ($Z = 37$) [32] demonstrate how the β-softness can be related to potential energy surfaces of

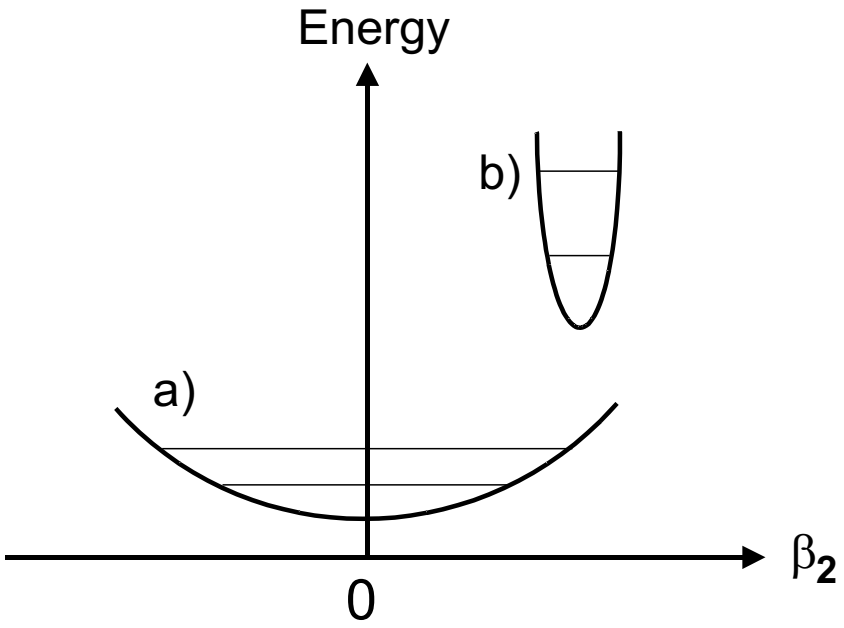

Figure 2.4: a) Potential well of a soft nucleus with mean deformation $\langle\beta_2\rangle \sim 0$. The shallow shape of the potential well allows the nucleus to freely fluctuate around its equilibrium shape. b) Potential well of a rigid nucleus with mean deformation $\langle\beta_2\rangle > 0$. The steepness of the potential well confines the nucleus to a rigid shape.

nuclei. Figure (2.4) illustrates how the softness of a nucleus can be related to its potential energy. A nucleus in a shallow potential energy well has got the freedom to vibrate about its equilibrium shape without changing its energy. A nucleus in a steep well is not able to vibrate a lot and the energy levels are much further apart, indicating that the nucleus cannot be excited as easily.

2.4 The Nilsson Model

The Nilsson model was developed as a unified model to combine the spherical shell model and the effects of nuclear deformation.

The spherical shell model assumes an extreme form of single particle behaviour

for all nuclei in the nucleus. The solutions of the Hamiltonian

$$\hat{\mathcal{H}}\Psi = \Delta\Psi + V(r)\Psi \tag{2.44}$$

lead to a structure of shells that are occupied by the nucleons. Here, Δ is the Laplace operator and $V(r) = \frac{-V_0}{1+e^{(r-R)/a}}$ is the Wood-Saxon potential. The model is refined by the introduction of the spin-orbit interaction $V_0\hat{l}\cdot\hat{s}$ leading to large shell gaps at so called magic numbers. At these magic numbers, nuclei have been found to be very stable and of spherical shape. The shell structure of nuclei has been well established experimentally and is directly evident in the charge radii systematics and in neutron and proton separation energies.

In midshell regions nuclei have been found to be well-deformed and the spherical shell model is not suited to explain their properties that are often caused by collective behaviour of the nucleons. In 1955 S G Nilsson [33] developed a unified model, the Nilsson Model, that incorporates deformation into the single particle model.

Figure (2.5) shows an axially symmetrically deformed nucleus and projection of the nuclear spin onto the symmetry axis. Where the spin component along the symmetry axis itself is still a constant of motion, any odd nucleon that is moving in this now deformed potential does not possess a conserved spin any more. This leads to a lifting of the $(2j+1)$ degeneracy of the energy levels for a spherical potential and the resulting energy levels are referred to as Nilsson states. Figure (2.6) shows the Nilsson diagram for neutrons, $50 \geq \mathrm{N} \geq 82$ [34].

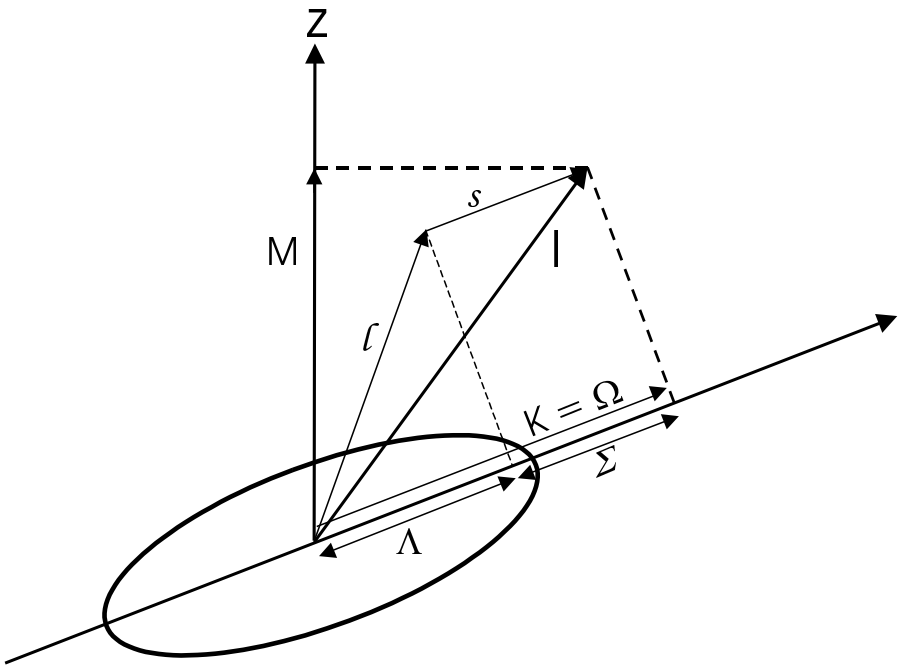

Figure 2.5: The spin projections of the total angular momentum I for an axially symmetrical deformed nucleus. M is the projection onto the lab axis, K is the projection onto the nuclear symmetry axis. Λ is the projection of the orbital angular momentum vector ℓ onto the nuclear symmetry axis and Σ is the projection for the spin vector s. For most ground state nuclei, the spin is determined by the last unpaired nucleon and $K = \Omega$.

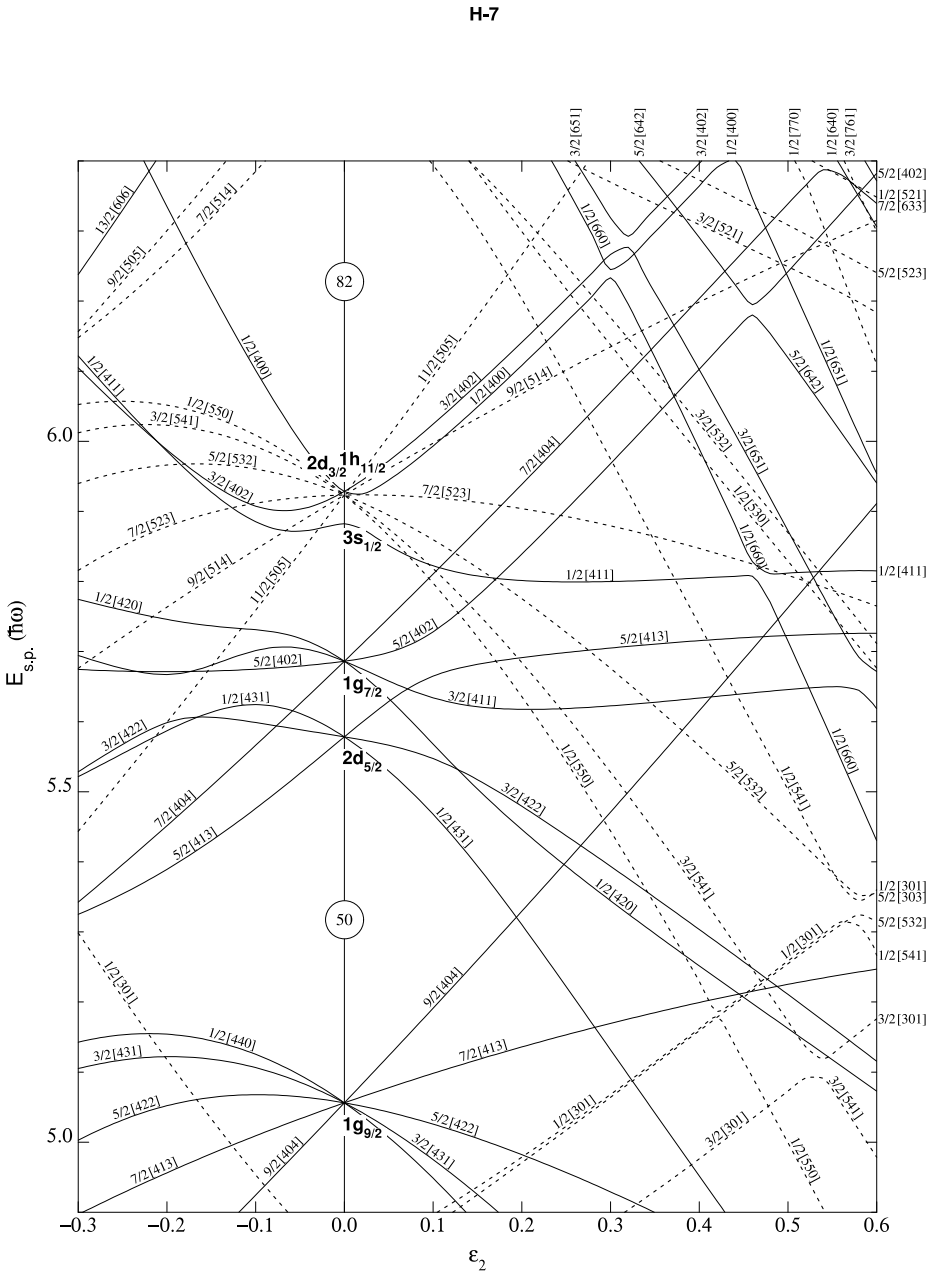

Figure 2.6: Nilsson diagrams for neutrons $50 \geq N \geq 82$ [34]

2.5 Atomic Theory

In a real atom there are usually many available energy levels for electrons to decay from or be excited to. In terms of angular momentum J and parity π, optical transitions from one energy level to another are allowed if

$$\begin{aligned} \Delta J &= 0, \pm 1 \\ \Delta \pi &= -1 \end{aligned}$$

Transitions of the kind $J = 0 \rightarrow J = 0$ are forbidden.

The change in population of atomic energy levels due to the atom-laser interaction can be described by the rate equations. In a two level system with upper level i and lower level k, the Einstein coefficient A_{ik} describes the probability for the process of spontaneous de-excitation. Whereas spontaneous de-excitation with the emission of a photon is a purely statistical process, excitation and de-excitation can also occur as an interaction process of the atom with the electric field of an incoming beam of light. This beam can be provided for example by a laser beam. The electric field interacts with the atom and induces stimulated excitation and de-excitation of electrons. This probability is described by Einstein's B-coefficients B_{ki} and B_{ik}. Both processes are illustrated in Figure (2.7).

The A-coefficient

The strength with which the excited electrons decay back by optical transitions into the ground state or other available metastable states in the absence of an external electric field is expressed by Einstein's A-coefficient for spontaneous decay. Every decay branch has got an individual A-factor A_i. The total A-factor of an energy level is obtained by summing up all A_i's of the individual decay branches, $\sum A_i = A$.

The total transition strength A is related to the lifetime τ of the transition via

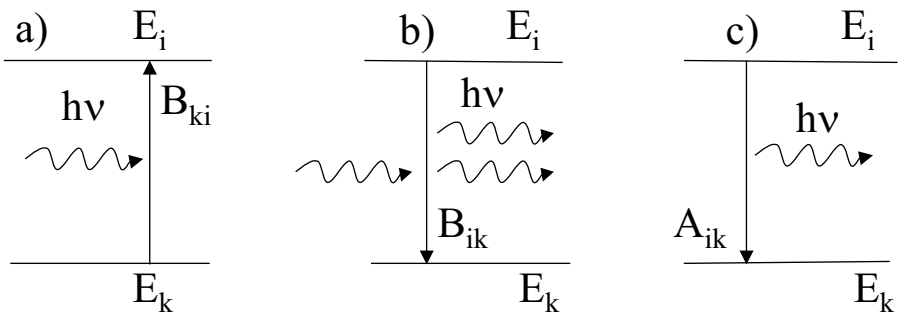

Figure 2.7: The processes of a) stimulated excitation b) stimulated de-excitation and c) spontaneous de-excitation

$A = 1/\tau$. The lifetime of the produced metastable states depends on the available decay options. When decay via electric dipole transitions is forbidden, for example by parity considerations, decay can take place via other means than electric dipole transitions (e.g. 2-photon processes, quadrupole...). The radiative lifetime for these processes is orders of magnitude longer and the energy level is then called a metastable state. The decay of levels due to collisions depends on pressure and density of the surrounding gas. The lifetime of the level is also connected to the natural linewidth of a transition. Using the Heisenberg Uncertainty Principle, $\tau \Delta E \geq \hbar$, the lower frequency limit $\delta\nu$ for the FWHM of the natural linewidth can be calculated as follows [35]

$$\begin{aligned} \Delta E &= \Delta\nu h \geq \frac{h}{2\pi\tau} \\ &\geq \frac{hA}{2\pi} \\ \Leftrightarrow \Delta\nu &\geq \frac{A}{2\pi} \end{aligned} \tag{2.45}$$

2.5.1 Interaction between atoms and light

The B-coefficient can be connected to the interaction process between the light and the atom. The electric field of incoming light can interact with the electrons of an atom and cause them to transit from one energy level to another. The interaction can be treated in a semi-classical way using perturbation theory. The wave function $\Psi(\vec{r},t)$ describes the interaction as a solution to the time-dependent Schrödinger equation

$$i\hbar\frac{\partial\Psi}{\partial t} = \hat{\mathcal{H}}\Psi \tag{2.46}$$

where $\hat{\mathcal{H}} = \hat{\mathcal{H}}_I + \hat{\mathcal{H}}_{\mathcal{P}}$. Here, $\hat{\mathcal{H}}_I$ is the Hamiltonian of the unperturbed atomic system and $\hat{\mathcal{H}}_{\mathcal{P}}$ introduces a perturbation to the quantum mechanical system due to a classically described electric field $\vec{E}(t)$ and

$$\begin{aligned}\vec{E}(t) &= \vec{E}_\omega\cos(\vec{k}.\vec{r}-\omega t)\\ &= \frac{1}{2}\vec{E}_\omega(e^{i(\vec{k}.\vec{r}-\omega t)}+e^{-i(\vec{k}.\vec{r}-\omega t)})\end{aligned} \tag{2.47}$$

As the wavelength of the incoming light is usually several orders of magnitude bigger than the diameter of the atom, the spatial variation of the electric field across the atom can be seen as small and the atom will respond to the field with an instantaneous dipole moment $\vec{p} = -e\vec{r}$. The perturbation Hamiltonian will now become

$$\hat{\mathcal{H}}_{\mathcal{P}} = -\vec{p}.\vec{E}(t) \tag{2.48}$$

The solutions to equation (2.46) will have the form

$$\Psi(\vec{r},t) = \sum_n a_n(t)\psi_n(r)e^{-iE_nt/\hbar} \tag{2.49}$$

where $\psi_n(r)$ are the time independent wave functions of the unperturbed system

and E_n are the corresponding energy eigenvalues. The $a_n(t)$ are the coefficients of the spatial wave functions. If the atom is in state i at $t = 0$ then $a_i(0) = 1$ and $a_{n\neq i}(0) = 0$. An explicit expression for $|a_k(t)|^2$ would then describe the probability that a transtition has taken place between the states i and k after some time t.

Corney [17] shows that by substituting (2.49) into (2.46) and using several other steps, the probability $|a_k(t)|^2$ of finding the atom in the excited state k is obtained as

$$|a_k(t)|^2 = \frac{e^2}{4\hbar^2}|\langle k|\vec{r}\vec{E}_\omega e^{i(\vec{k}.\vec{r})}|i\rangle|^2 \frac{\sin^2((\omega_{ki}-\omega)t/2)}{((\omega_{ki}-\omega)/2)^2} \tag{2.50}$$

Here $\omega_{ki} = (E_k - E_i)/\hbar$ is the transition frequency between the two energy states E_k and E_i and ω is the frequency of the incoming monocromatic light [17]. The exponential term in the matrix element in equation (2.50) can be expanded by a Taylor expansion: $e^{i(\vec{k}.\vec{r})} \approx 1 + i(\vec{k}.\vec{r}) - \frac{1}{2}(\vec{k}.\vec{r})^2...$ As kr is small compared to 1, $|\langle k|\vec{r}\vec{E}_\omega e^{i(\vec{k}\vec{r})}|i\rangle|^2$ in equation (2.50) reduces to the matrix element of an electric dipole operator $|\langle k|\vec{r}\vec{E}_\omega|i\rangle|^2$.

For isotropic and unpolarized radiation, the average over all possible directions of the polarization of the dipole vector $\vec{E}_\omega$ gives a matrix element $|\langle k|\vec{r}|i\rangle|^2$. It emerges that this matrix element is directly proportional to the Einstein coefficient B^ρ_{ik} for stimulated absorption (for a full derivation see [17]).

$$B^\rho_{ik} = \frac{\pi e^2}{3\epsilon_0\hbar^2}|\langle k|\vec{r}|i\rangle|^2 \tag{2.51}$$

The transition probability per unit time P_{ik} for stimulated excitation or de-excitation is proportional to the Einstein B-coefficient and to the energy density of radiation per unit bandwidth $\rho(\omega_{ki})$ at the angular frequency ω_{ki}

$$P_{ik} = B^\rho_{ik}\rho(\omega_{ik}) \tag{2.52}$$

The A- and the B-values are connected by

$$B_{ik}^{\rho} = \frac{\pi^2 c^3}{\hbar \omega_{ki}^3} \times \frac{g_k}{g_i} A_{ki} \tag{2.53}$$

[17, 36, 37]. The g_i and g_k are the multiplicities, $(2J + 1)$, of the energy levels E_i and E_k with angular momentum J_i and J_k. A large A-value indicates a large B-value and therefore a high probability for excitation.

The natural linewidth of a transition is determined by the lifetime of the upper energy level and leads to a Lorentzian line shape. Line broadening can occur through collisions and saturation effects and most importanly through Doppler broadening. A good overview about natural linewidth and line broadening processes is given in Haken and Wolf [38].

2.5.2 Optical Pumping

Optical pumping is a process in which electrons are raised (pumped) into a higher lying energy state. The process was developed by Brossel, Bitter and Kastler in the early 1950s [39]. Electrons are selectively stimulated by an incoming monochromatic beam of light that matches their transition frequency. In laser spectroscopy, the laser beam is polarised and the ions are distributed isotropically in space, hence the overall population of ions will behave as if encountering an unpolarised beam of light. In thermal equilibrium, the occupation of atomic energy levels with electrons follows a Boltzmann distribution

$$\frac{N_i}{N_k} = \frac{g_i}{g_k} e^{-\frac{E_i - E_k}{kT}} \tag{2.54}$$

When electrons are pumped into a metastable state, the thermal equilibrium of the system is disturbed. However, this is only possible if the lifetime of the metastable state is sufficiently long, i.e. the electrons do not immediately relax back into their initial energy state. In this way, the population of an upper state can be artificially enhanced, often to the extent of the complete de-population of the ground state.

Figure (2.8) shows a very simple pumping scheme. The electrons are excited from $E_k^{J\pi}$ into the upper energy level $E_i^{J\pi}$ and relax back into the lower energy levels according to the probability for spontaneous emission A_{ik} and A_{in} (section 2.5). Usually selection rules (equation 2.45) allow routes into different low lying energy states. Then, if there are no opposite parity states at lower energies, the electrons are locked, as further relaxation from the low lying metastable $E_n^{J\pi}$ state into the ground state $E_k^{J\pi}$ is forbidden by parity considerations.

The efficiency of a particular pumping scheme can be estimated by comparing A-coefficients of different transitions. The redistribution of the ground state population

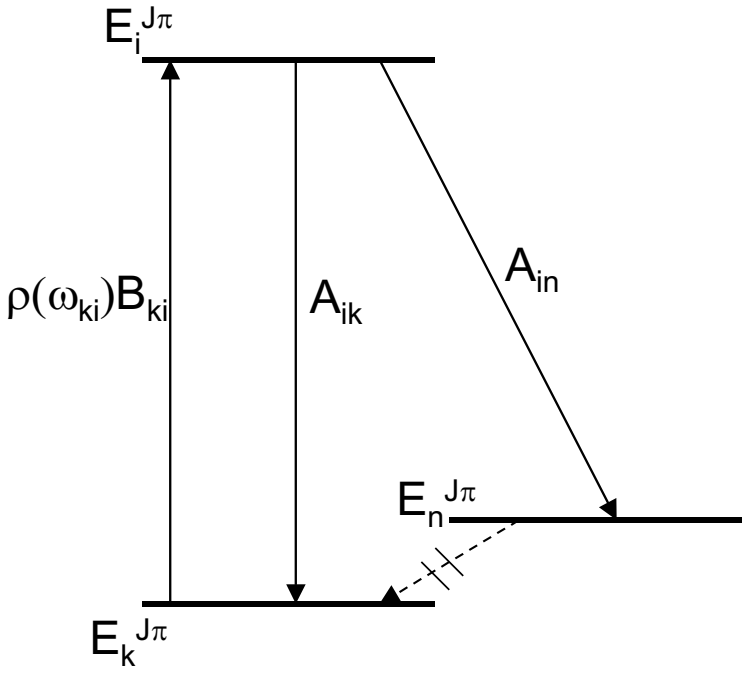

Figure 2.8: A simple pumping scheme with three levels. The electrons are pumped into level $E_i^{J\pi}$ and build up a population enhancement in $E_n^{J\pi}$ as electric dipole transitions between $E_n^{J\pi}$ and $E_k^{J\pi}$ are forbidden by parity.

can be simulated using rate equations

$$\begin{aligned}
\frac{dN_i}{dt} &= -N_i A_{ik} - N_i A_{in} + \rho(\omega_{ki}) B^{\rho}_{ki} N_k - \rho(\omega_{ki}) B^{\rho}_{ik} N_i \\
\frac{dN_k}{dt} &= -\rho(\omega_{ki}) B^{\rho}_{ki} N_k + N_i A_{ik} + \rho(\omega_{ki}) B^{\rho}_{ik} N_i \\
\frac{dN_n}{dt} &= +N_i A_{ik}
\end{aligned} \tag{2.55}$$

where $\rho(\omega_{ki})$ and B^{ρ}_{ki} are defined as in equation (2.52) and equation (2.53). An increase in population in level E_n will take place even if $A_{in} < A_{ik}$ as transitions bewteen E_n and E_k are strongly hindered and any decay into E_n will eventually build up.

2.6 Non-Linear Optics

The theory of non-linear optics describes the behaviour of light in non-linear media. Using crystals without reflection symmetry, it is possible to generate higher harmonics of a beam of light. This method is applied experimentally to laser beams in order to achieve the short wavelengths required for the experiment.

If light travels through a medium, the electric field strength of the light wave causes a polarization $\vec{P}$ of the electric field of the atoms in the medium. For normal light sources, the strength of the polarization is directly proportional to the electric field strength $\vec{E}$ of the incoming light. For high intensity light such as laser light the polarization effects are non-linear and must be expressed by taking into account higher order terms

$$\vec{P} = \epsilon_0(\bar{\chi}_1\vec{E} + \bar{\chi}_2\vec{E}^2 + \bar{\chi}_3\vec{E}^3 + ...) = \vec{P}^1 + \vec{P}^2 + \vec{P}^3 + ... \tag{2.56}$$

where $\vec{P}$ is the total polarization, $\bar{\chi}_i$ are the electric susceptibility tensors and ϵ_0 is the permittivity of free space [40].

For an incoming light wave $\vec{E} = \vec{E}_0(\sin\omega t)$ equation (2.56) becomes

$$\begin{aligned} \vec{P} &= \epsilon_0\chi_1\vec{E}_0\sin\omega t + \epsilon_0\chi_2\vec{E}_0^2\sin^2\omega t + \epsilon_0\chi_3\vec{E}_0^3\sin^3\omega t... \\ &= \epsilon_0\chi_1\vec{E}_0\sin\omega t + \frac{\epsilon_0\chi_2}{2}\vec{E}_0^2(1-\cos 2\omega t) + ... \end{aligned} \tag{2.57}$$

The second order polarization term represents a process called second-harmonic generation (SHG). It means that when a photon field of high power density passes through a medium, two photons of frequency ω can coalesce to form a photon of frequency 2ω. This is frequency doubled light.

In isotropic media $\chi_2 = 0$ and the second term in equation (2.57) vanishes. Thus, only certain crystal classes are suitable to generate frequency doubled light in the

first place. In practice, an additional challenge is the production of enough intensity of the doubled light. The difficulty is posed by the frequency dependence of the refractive index n as usually $n_\omega \neq n_{2\omega}$ even within a suitable crystal. Since the 2ω-wave is produced all the way through the crystal, the different contributions will continuously fall out of phase with each other. They will only combine constructively if a proper phase relationship is maintained between the 2ω-wave and the fundamental ω. Experimentally, this can be done using a birefringent crystal. Here, $n_\omega = n_{2\omega}$ can be arranged [40] by tilting the angle of the crystal. Another method to match the refractive indices is to use the temperature dependence of the refractive index and heat the crystal until $n_\omega = n_{2\omega}$.

Although equation (2.57) indicates the generation of tripled and quadrupled light, at JYFL these frequencies are not produced directly from the fundamental ω. The probability of three or even four photons merging together is simply too small. Instead, tripled light is achieved by coalescing the fundamental ω with already doubled light of frequency 2ω to form $\omega + 2\omega = 3\omega$. Quadrupled light originates from $2\omega + 2\omega = 4\omega$.

Chapter 3

EXPERIMENTAL FACILITY

The radioactive isotopes investigated in this work were produced at the IGISOL (Ion Guide Isotope Separator On-Line) at the University of Jyväskylä cyclotron laboratory [41]. After collision of a high energy proton beam with stable target material, several elements are used to form a beam of purified mass and low energy spread out of the generated products. Stable isotopes can be produced from an electrical discharge source inside the IGISOL. After extraction from the IGISOL, the singly charged ions are sent through a mass separating magnet. The purified beam is then cooled down to thermal energies in the ion beam cooler [42]. As a result, the beam particles are energetically decoupled from their state of production in the IGISOL. Additionally, the ions can be held inside the ion beam cooler for up to several hundred milliseconds which introduces a time structure to the otherwise continuous beam. The ion beam cooler is also the ideal place to optically pump the ions into metastable states. The ions are then extracted and an acceleration voltage of 30 kV is applied to guide the ions to the interaction region where they meet a high resolution laser beam for interrogation. The acceleration reduces the Doppler spread of the ions in the direction of travel and the recorded hyperfine structure can be resolved down to the order of the natural linewidth of the transition.

Figure (3.1) gives a schematic overview over the key elements in the experimental setup. During online experiments, the first 90° bend after the cooler can be de-

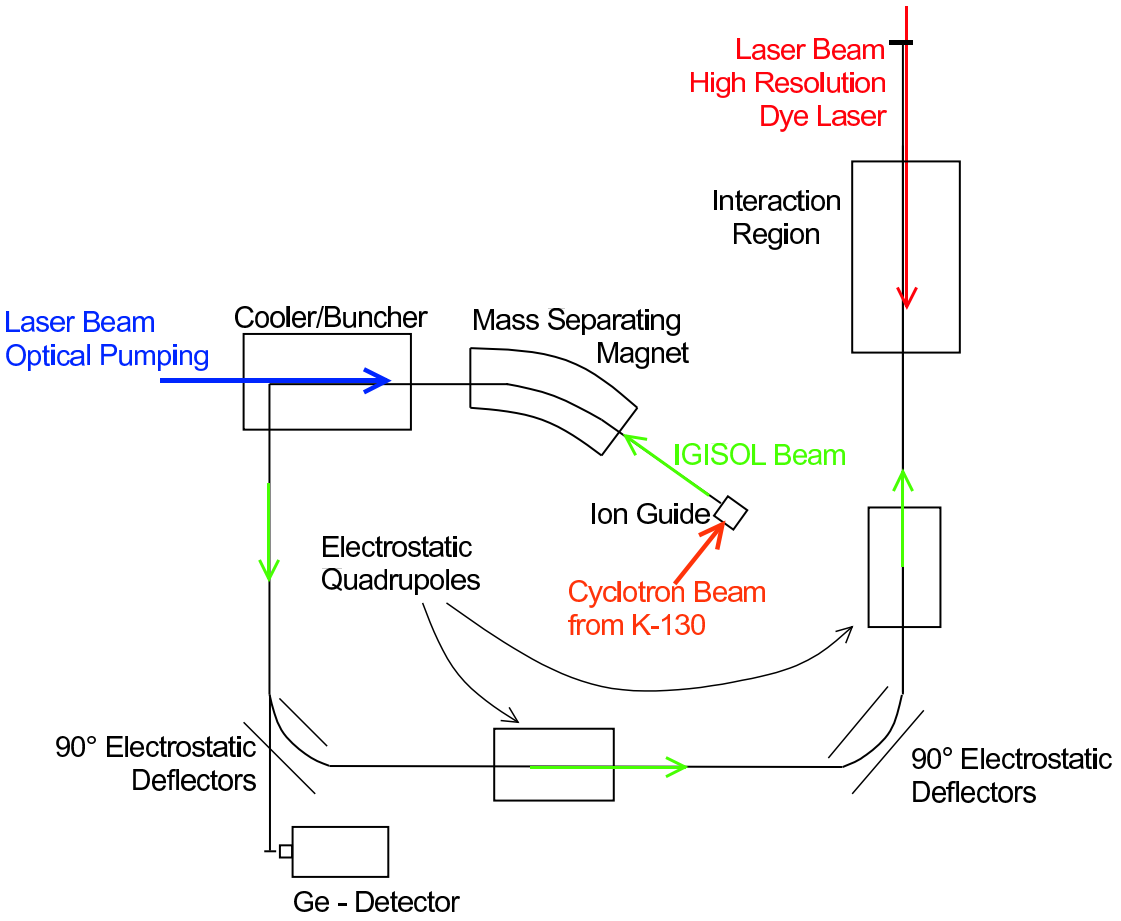

Figure 3.1: Schematic diagram of the layout of the IGISOL beam-line.

activated and the beam can be directed onto a germanium detector for an initial identification of the produced isotopes. When activated, the 90° bend leads the ions onto the second floor where the interaction region is located. The electric quadrupoles are used for guidance of the radioactive beam.

The production mechanism and the necessary steps for beam formation will be explained in more detail below.

3.1 Isotope Production at the IGISOL

At JYFL, a K-130 cyclotron is used to produce light ion beams for online-experiments. The IGISOL is designed for light-ion fusion as well as fission reactions and the reaction products are extracted using a buffer gas. The very short extraction time of the reaction products and the chemical insensitivity of the extraction mechanism is a particular advantage of the IGISOL method and isotopes with half-lives as short as 10 milliseconds have been investigated [43]. The chemical insensitivity allows the production of even refractory isotopes. On the downside of this method, the reaction products leave the IGISOL with an energy spread of about 250 eV where other conventional ISOL facilities achieve thermal energy spreads.

In this experiment a fission ion-guide was used inside the IGISOL. The incoming cyclotron beam hits a natural uranium target and a plasma of high momentum fission products (200 MeV) is created in the ion-guide (figure 3.2). The target foil is situated at an angle of 7° to the beam direction to maximise the target thickness in the beam direction. A separation foil shields the plasma from the exit of the IGISOL. Helium gas is introduced into the chamber at about 250 mbar to take out the fission products. The fission products are slowed down by passing through the chamber separation foil and recombine to singly charged ions via three-body collisions. The material of the chamber separation foil is often made of stable isotopes of the isotopic chain under investigation in order to give a calibration isotope during the spectroscopy. The desired charge state for the fission products and stable ions is 1+ as all other charge states will be lost during further travel into the beam line.

When leaving the IGISOL, all fission products are guided into the SextuPole Ion Guide (SPIG). The SPIG consists of six segmented rods that have an alternating radio frequency field superimposed on to a DC-voltage along the rods. The SPIG is divided into two segments that have DC offsets of 1-2 V [44] to guide the ions

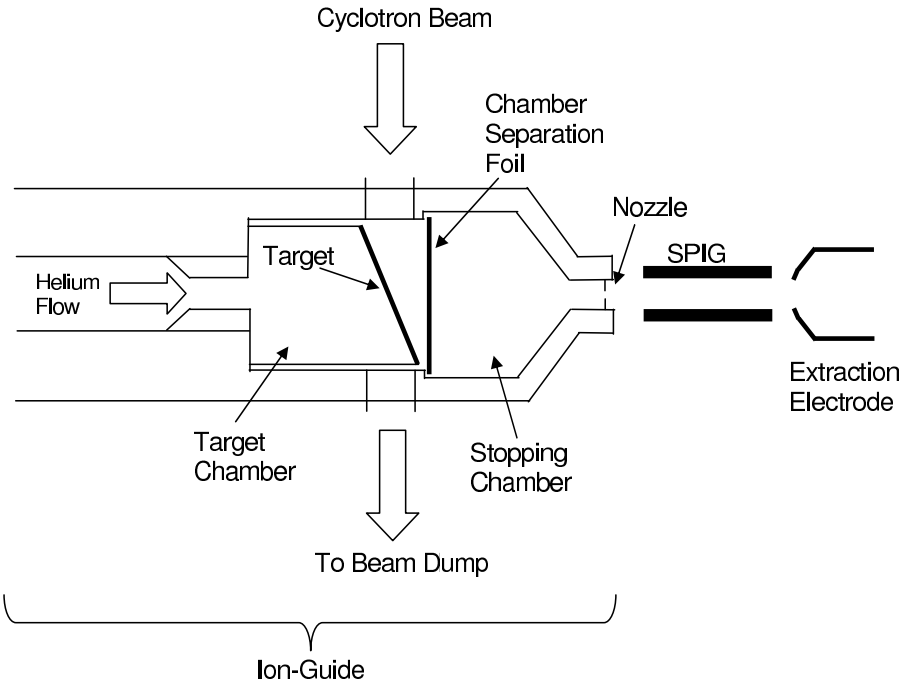

Figure 3.2: Scheme of the fission ion guide in the IGISOL as well as the SPIG and the extraction electrode.

along the sextupole forming rods. Neutral atoms of all masses will be lost into a large vacuum pump under the SPIG. Ions of the wrong charge state and light ions (e.g. He-ions) will be lost because their trajectories are not supported by the specific RF- and DC-fields of the SPIG. In this way only a range of singly ionised fission products will survive through the SPIG on stable trajectories. These are then further accelerated into the beam line by the extraction electrode.

Behind the SPIG an extractor is placed at a 10 kV lower potential than the IGISOL (30 kV). The acceleration of the beam is achieved through electric potential differences along the beam line. The beam tube behind the extractor lies at ground

potential. Beam formation along the beam line is achieved through electrostatic lenses. Isotope separation takes place through a mass separating magnet. The magnet allows masses with one selected charge to mass ratio, q/m, to pass and has a mass resolving power of $\frac{M}{\Delta M} = 200$ to 500 [45]. This mass separation is reasonably accurate although very abundant masses were observed to cause a tail into other q/m ratios. Also, isobaric contamination cannot be prevented or suppressed.

Off-line Beams

For off-line experiments an electrical discharge source can be placed inside the IGISOL chamber. Stable sample material of the element of interest is deposited at the cathode and a voltage of ~ 500 V is applied across a little gap to the anode. This voltage causes sputtering and ionisation of the sample material and hence, stable ions for spectroscopy. Beam extraction takes then place as described above.

3.2 The Beam Cooler

The ion cooler was introduced into the beam line to improve the quality of the ionic beam which then increased the sensitivity of the whole experiment. The quality of the beam is mainly improved by reducing the beam emittance and the longitudinal energy spread. The reduced spread decreases the Doppler broadening of the beam and allows better resolution of the atomic spectra. Also, the reduced beam emittance allows an improved overlap of the ionic and the laser beam, leading to better experimental efficiency.

The underlying principle is the one of a mass separating Paul trap [44]: The main part of the cooler consists of four rods that are segmented [46]. They form a quadrupole that has an alternating voltage applied (figure (3.3)). This voltage forces the ions into circular motion, creating a spiral pattern along the beam direction. The ions are already decelerated when they enter the cooler and a small voltage gradient along the beam axis causes the ions to drift towards the opposite end of the cooler (see voltage profile in figure (3.4)). The total voltage V at one segment can be expressed as:

$$V = V(z) + V(x, y) \tag{3.1}$$

where $V(x, y) = V_0 \sin(\omega t)$. In a mass separating Paul trap, certain masses form stable trajectories for a given frequency. For the beam cooler the range of masses that reach the end of the cooler through stable trajectories is increased by the addition of helium as a quenching gas. The incoming ions undergo collisions in the gas that confines them more and more onto the central beam axis, so that at the end of the cooler the ions will have nearly completely lost their radial spread.

The trajectories of the beam particles can be expressed by differential equations that are known as Mathieu equations [46]. Experimentally, the optimum conditions

are determined by looking at the transmission through the cooler as a function of frequency and pressure. Figure (3.5) shows this on the example of a stable beam of $^{89}Y^{2+}$. The number of beam particles that exit the cooler is plotted as a function of gas pressure. It appears that the beam yield is highest for a pressure of 6.4×10^{-5} mbar.

Experience has shown that the optimum cooler pressure for a particular isotope differs for a radioactive beam with respect to a stable beam. Due to the different production mechanisms (section 3.1), radioactive beams have initially a wider energy spread and a higher emittance than beams that are produced from electrical discharge sources. Therefore, they require a higher gas pressure in the cooler in order to reduce their energy spread.

A further application of the beam cooler is to control the time structure of the ion beam. A voltage trap that can be created by application of a voltage to the endplate of the cooler allows the collection of a bunch of ions which are then simultaneously released towards the interaction region (dotted line in figure (3.4)). This bunching of the ion beam has allowed for a very sensitive laser spectroscopy technique to be developed, which can reduce the background by several orders of magnitude. A more detailed description will be given in section 3.3.1.

Optical Pumping

The beam cooler is also the place where the laser beam for optical pumping is introduced into the experimental setup. This place is ideally suited to optically pump ions into metastable states as the ions have just left the ion guide. The amount of time spent in the cooler as well as their drifting at thermal energies ensure a good overlap of the ions and the pulsed laser beam. In bunching mode the ions are held in the cooler for up to 200 ms and with a repetition rate of 10 kHz a single ion can be pumped up to 2000 times.

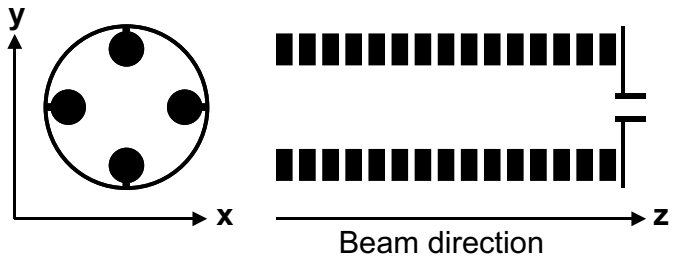

Figure 3.3: Segmented RF-region of the beam cooler/ion-drift region [42]

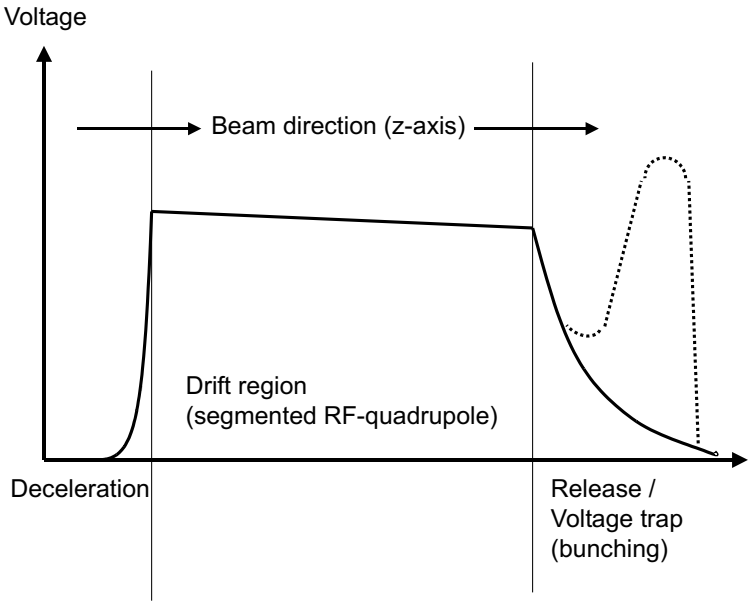

Figure 3.4: Schematic voltage profile of the beam cooler in beam direction. The dotted line represents the optionally applied trap voltage [42]

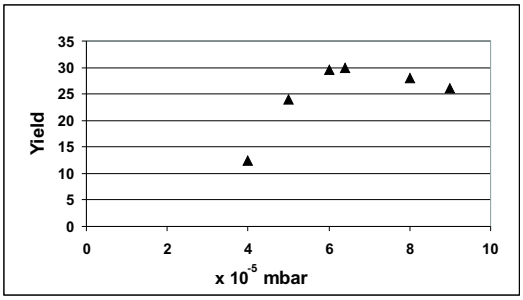

Figure 3.5: Ion yield of a stable beam of $^{89}Y^{2+}$ behind the cooler as a function of the quenching gas pressure at constant radiofrequency.

3.3 Collinear Laser Spectroscopy

After extraction from the cooler the ions are again accelerated to their final energy (about 30 keV). Over time, laser spectroscopists thought of different methods of overcoming the Doppler broadening that under normal conditions spoils the resolution of atomic lines and covers the details of the transitions which are of interest. Collinear laser spectroscopy takes advantage of the fact that the radioactive isotopes of interest are produced as ions. Since Doppler broadening appears as a result of the velocity spread δv of the ions, this velocity spread can be reduced significantly by increasing the kinetic energy E of the ions via high voltage (see figure 3.6):

$$\begin{aligned} E &= \frac{1}{2}mv^2 \\ \therefore \delta E &= mv \cdot \delta v \\ \Rightarrow \delta v &= \frac{\delta E}{mv} \end{aligned} \tag{3.2}$$

where m is the mass of the ion and v its velocity. As can be seen from equation (3.2), for a constant energy spread δE an increase of velocity v results in a reduced velocity spread δv. Therefore, acceleration of the ions allows their spectral lines to be resolved close to the natural line width. However, when the ions eventually meet the laser for interrogation they are Doppler shifted with respect to the laser beam. Therefore, instead of being tuned to the intrinsic transition frequency, the laser needs to be tuned to the Doppler shifted transition frequency of the ions.

The relationship between the intrinsic transition frequency ν_0 and the shifted frequency ν_L is

$$\nu_0 = \nu_L(1 + \alpha + \sqrt{\alpha^2 + 2\alpha}) \tag{3.3}$$

where $\alpha = \frac{eV}{mc^2}$. Here, the voltage V applied to the cooler is multiplied by the charge

e of the ion and mc^2 is the rest mass of the specific isotope.

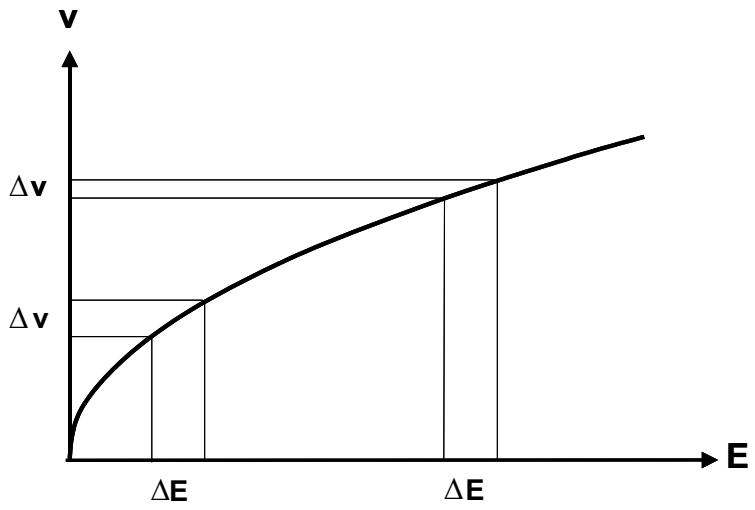

Figure 3.6: Relationship between energy spread and velocity spread

An additional constraint is that the laser frequency has to coincide with an iodine absorption peak for the purpose of frequency stabilization (section 3.4.2). The shifted transition frequency of the ions might not match this condition. It is possible to apply an additional voltage to the interaction region, so that the condition can be met and the total voltage V_{total} applied to the ions is then

$$V_{total} = V_C + V_t \tag{3.4}$$

where V_C is the voltage applied to the cooler and V_t the tuning voltage applied to the interaction region.

V_t can be used to scan across the whole transition and is found by identifying the appropriate iodine absorption peak in the iodine atlas by Gerstenkorn and Luc [51] and recalculating α using

$$\alpha = \frac{(\nu_0 - \nu_L)^2}{2\nu_0\nu_L} \tag{3.5}$$

In practise, the cooler voltage is positive since it pushes the ions away from the

cooler. The tuning voltage is usually negative and pulls the ions into the interaction region. The tuning voltage V_t is always chosen to be at several hundred volts. This is in order to allow the scan itself to start at slightly lower voltage than the expected transition. By continuously increasing V_t during the experiment, all features of the ionic transition can be brought onto resonance with the laser frequency and a spectrum can be recorded.

3.3.1 The Interaction Region

The interaction region is where the accelerated ion beam and the interrogating laser overlap and atomic transitions are scanned. The ion beam and the laser meet in a collinear arrangement which maximises the interaction time (figure (3.7)).

In order to align the ion beam into a long narrow cone, two apertures (6 mm and 1 mm) are installed along the beam line. Too broad and parallel an ion beam would require more laser power per unit area over a larger area and increase the amount of scattered light and therefore the photon background. On the other hand too tightly a focused beam allows the ions an increased deviation perpendicular to the beam direction at the cost of the velocity component along the beam line. This would mean that the ions on a steep ray path need a higher acceleration voltage in order to come to resonance than the ones that travel only in the beam direction without a perpendicular component.

The light collection optics at 90° to the beam direction collects the emitted fluorescent photons (figure (3.7)). It consists of a lens set up that preserves the spatial resolution of the photons and a spatially segmented photomultiplier tube (PMT) that converts the emitted light into an electronic output signal.

The size of the incoming ion current can be measured behind the interaction region, using microchannel plates for currents up to 100 000 ions/s or a Faraday cup for large off-line beams. The deflector plates are used to divert the ion beam onto

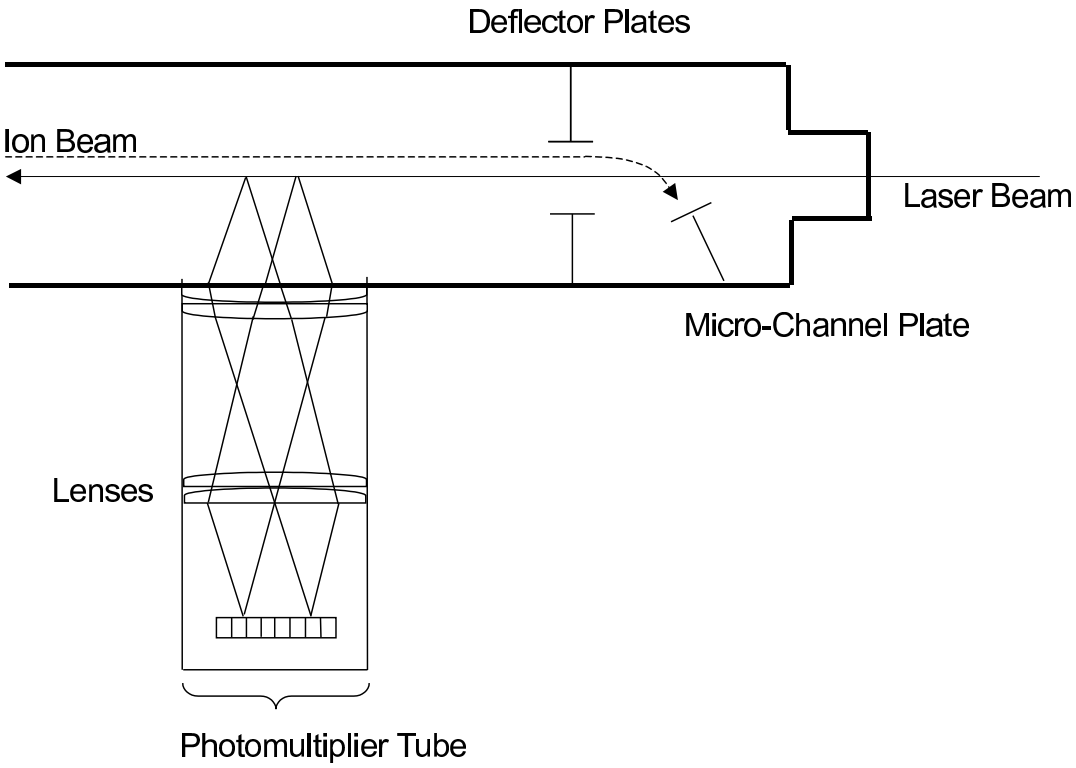

Figure 3.7: The interaction region showing the ion beam meeting collinearly with the laser beam. The resonance photons are collected via a lens system in the front of a photomultiplier tube [47].

the microchannel plates.

3.3.2 Bunching

The method of bunching the ion beam was introduced in collinear laser spectroscopy in order to reduce the photon background. Where in continuous operation every photon is counted, in the bunching method a coincidence gate is applied and times when no ions pass the photomultiplier tube are cut out. A voltage barrier is applied at the end of the beam cooler and the ions that are leaving the IGISOL are accumulated

in the ion cooler to form an ion bunch. The accumulation time (bunching time) can be varied and is usually taken to be 100 ms - 200 ms (figure 3.8). After that the ions are released and the whole bunch is accelerated along the beam line. The background suppression is the ratio of the time of the photomultiplier gate and the accumulation time in the cooler. As the photomultiplier gate is usually 20 μs the background suppression is of the order of 10^{-4}.

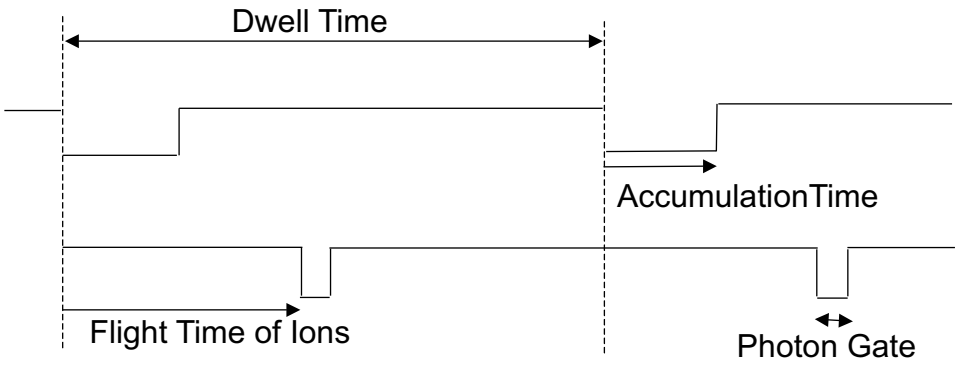

Figure 3.8: The time sequence of the bunching method. The dwell time of the recorded channel spans the accumulation time of the ions in the cooler and their flight time to the interaction region. While they are passing the photomultiplier tube a photon gate is applied to record the fluorescent photons.

3.4 The Lasers

Two different laser systems are used in this experiment. For the pumping process, a high powered solid state laser system with a broad linewidth and high output power is employed. The advantage of the high output power is that during the experiment it allows the light to be led over long distances into the pumping region and to still saturate the transition. The broad line width allows coverage of the energy width of the whole hyperfine structure of a level.

For the spectroscopy, a narrow line width tunable dye laser system is used. Its linewidth is smaller than the natural linewidth and is able to resolve the hyperfine structure features and the isotope shift. Its tunability allows a large range of frequencies to be accessed.

3.4.1 The Dye Laser

The laser used for the spectroscopy at JYFL is a Spectra Physics 380 dye laser which is pumped by a 532 nm Coherent Verdi laser. Next to its practical tunability it has got a narrow linewidth of not more than 2 MHz which allows easy resolution of the natural linewidth of atomic and ionic transitions. The active medium of a dye laser is dissolved organic dye molecules. They have a large number of excited states (Figure 3.9) which supply a large range of possible transitions. Population inversion is achieved by pumping the electrons from the ground state of the S0-band into the higher lying states of the S1-singlet band from where they decay via fast non-radiative transitions into the lowest energy level of the S1-band. From there the electrons drop back down into the various levels of the S0-band by photon emission. As some of the electrons are lost into the T0-band, the dye has to be circulated under high pressure to avoid building up to a point where the dye is exhausted. Using different dyes, for example Rhodamine 6G or SR640 [48], it is possible to cover a wavelength range of 570 nm to about 750 nm in the fundamental. Figure

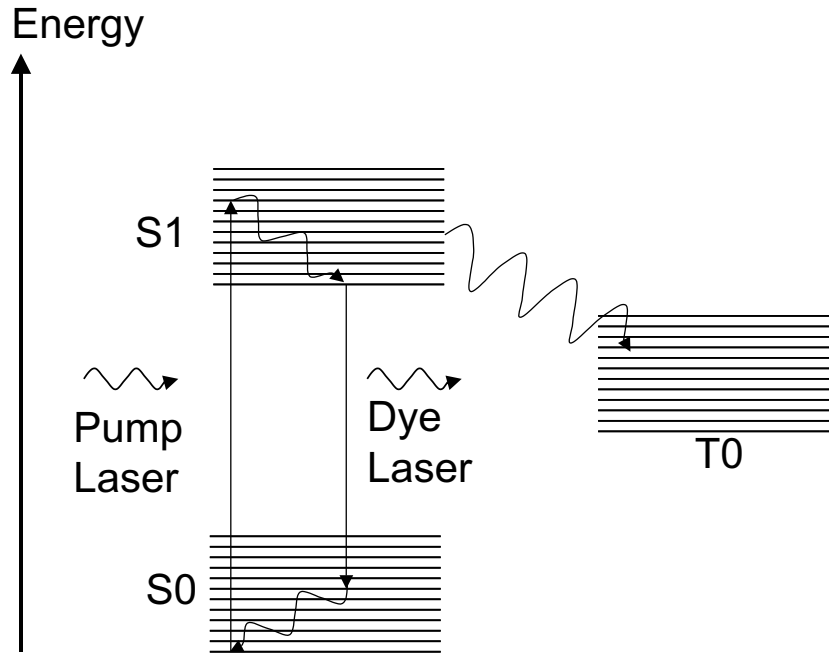

Figure 3.9: Scheme of the energy levels of the dye. Population inversion is achieved by exciting electrons into the S1-band where they pile up in the lowest available energy level

(3.10) shows the typical dye profile for Rhodamine 6G. The absorption spectrum of the dye lies at a shorter wave length than the emission spectrum.

A general scheme of the dye laser cavity is shown in figure 3.11. It consists of a pump mirror that focuses the beam of the Verdi laser onto the dye. It also contains the mirrors $M1$ to $M4$ which allow the laser photons to travel continuously around the cavity. The length L of the cavity supports only wavelengths λ that fulfill the condition

$$\lambda = \frac{L}{n} \quad \Leftrightarrow \quad \nu = n\frac{c}{L} \tag{3.6}$$

where n is an integer number and c is the speed of light. This causes a frequency separation of the output modes of ~ 200 MHz [49].

Initially the laser photons travel in both directions around the laser cavity, as the cavity does not impose a preferred direction onto the light. The introduction of a Uni-Directional Device (UDD) ensures that lasing occurs only in one direction in

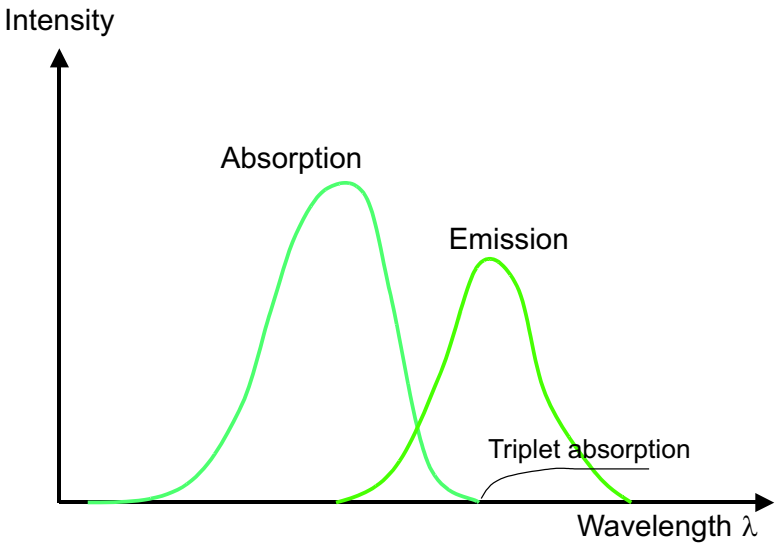

Figure 3.10: The typical wavelength spectrum of a dye laser. The absorption profile of the dye lies in a lower wavelength region than the emission profile, so that re-absorption of the laser photons into the dye is not significant. [49].

the cavity and no gain is lost by propagation in two directions. The UDD consists of a Faraday rotator and an optically active quartz compensator plate. Both rotate the polarization of the beam by $2° - 3°$. Whilst the rotation in polarization by the Faraday plate is dependent on the direction of propagation of the beam, the rotation caused by the quartz plate is not. The two rotations are opposite to each other for light travelling in the correct direction and no net change of the polarization is caused. However, a net change in polarization is caused for light that travels in the wrong direction. The change is increased with each time the light passes through the UDD. This light is then lost over repeated circulations through the cavity, because several of the components in the laser cavity are positioned at Brewster's angle. This position minimizes reflection losses for horizontally polarised light and suppresses vertically polarised light [49].

A single output frequency is then selected using different tuning devices. The

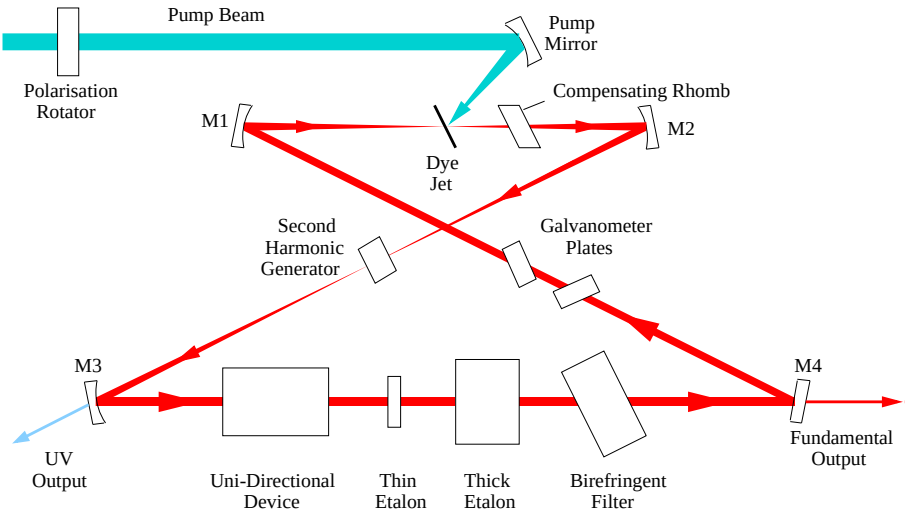

Figure 3.11: The Dye Laser Cavity [49]

Birefringent Filter (Figure 3.11) is a coarse tuning element for the selection of a single output mode. It has a transmission bandwidth of 0.5 nm [50] and consists of an arrangement of three birefringent plates. A birefringent material possesses the property to alter the polarisation of transmitted light depending on its wavelength. Again, the altered polarisation leads to losses at the Brewster surfaces inside the cavity and causes a sinusoidal transmission profile of the Birefringent filter. By tilting the angle of the Birefringent plate, the point of minimum transmission loss can be shifted to different wavelengths.

A single cavity mode is then chosen with the help of a thick and a thin etalon as explained in Figure (3.12). The thick etalon consists of two mirrors with a 30% reflective coating. The distance between the mirrors can be changed using a hollow cylindrical piezoelectric element. By applying voltage to the piezoelectric element, the length of the etalon can be altered, allowing cavity modes of various wavelengths to be chosen. The free spectral range of this etalon is 75 GHz. The thin etalon consists of a piece of glass that is approximately 0.11 mm thick [49].

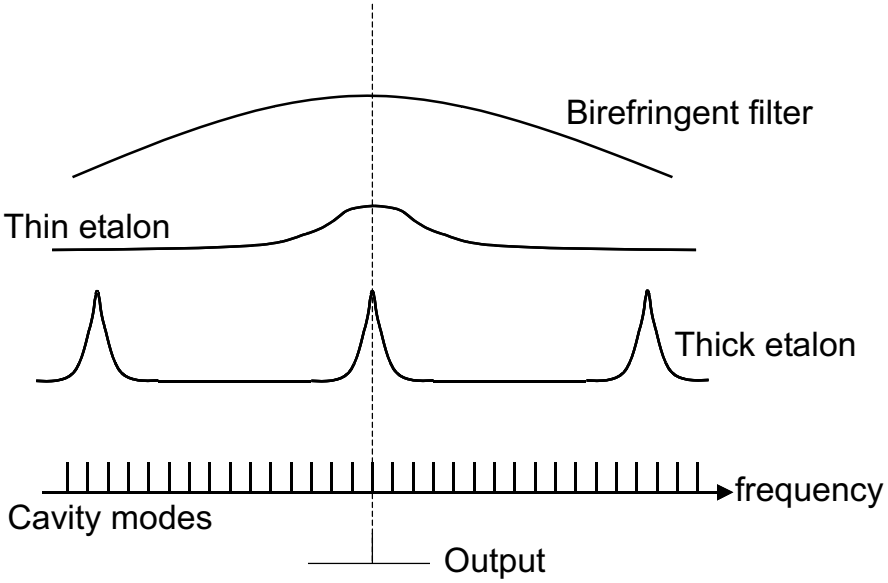

Figure 3.12: The interplay of the birefringent filter, the thick and the thin etalon in the selection of a single cavity mode

Its transmission profile is much broader than the profile of the thick etalon. It suppresses neighbouring maxima of the thick etalon and therefore helps prevent mode hops, i.e. a change from one supported cavity mode to another. The thin etalon is rarely used.

The electronically driven galvanometer plates in the cavity account for changes in optical path length and together with the thick etalon the laser frequency can be changed continously.

Inside the cavity all angles are kept small to avoid the effects of astigmatism. Astigmatism occurs if light is incident onto a curved mirror at an angle. The plane along the major axis of the resulting ellipsoidal light section will then have a different focal point to the plane along the minor axis. To account for any residual astigmatic effects, a rhomb is introduced into the cavity [50].

The crystal for second harmonic generation is situated inside the laser cavity (figure (3.11)). It is placed between the mirrors M2 and M3 at the secondary waist of the beam in order to maximise the power density of the laser beam into the

crystal. The crystal used in the experiment is β-Barium-Borate (β-BBO). β-BBO works well for the short wavelengths needed for the spectroscopy of niobium and proved convenient to work with in practice.

3.4.2 Frequency Stabilization

During the experiment the laser frequency needs to be stabilised in order to achieve the minimum linewidth. Vibrations that run through the building, mechanical noise and thermal expansion of the cavity result in vibration of the cavity and a laser line width that is not yet narrow enough for spectroscopic application. Passive devices like a concrete table for the cavity and the use of alloys with a small thermal expansion coefficient help stabilise the cavity and therefore the optical path length inside the cavity. In order to achieve the narrow linewidth of 1-2 MHz needed for spectroscopy, a frequency locking system is employed. The idea is to monitor fluctuations in the laser frequency by locking to the transmission profile of an etalon peak.

If light is sent through an etalon, the measured light intensity behind the etalon gives an indication on whether the laser frequency coincides with a transmission peak or not. This can be used to create a correction signal. When the laser frequency is adjusted to half maximum of the peak, a deviation in either direction will result in an increase or decrease in light intensity. When converted into voltage, a correction signal can be applied to drive the frequency back to its initial position.

In the experiment, a commercial Spectra Physics Stabilok is used for frequency stabilisation. The Stabilok contains two etalons: The laser is locked to the side of a high finesse reference etalon with a free spectral range that is bigger than the separation of the laser modes. Additionally a low finesse slave etalon is employed that takes care of bigger frequency jumps, like mode hops, that occur occasionally. In the event of a mode hop, the supported laser mode will be far off the high finesse

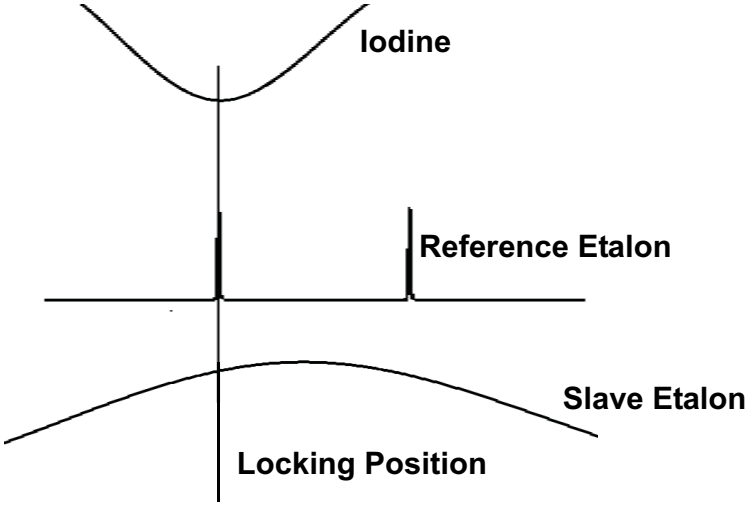

Figure 3.13: Frequency Stabilization of the Dye Laser: The laser is electronically locked to the bottom of an iodine peak and to the sides of the peaks of a reference and a slave etalon.

transmission peak, however it will still sit on the same low finesse peak as before. A servo loop can be used to bring the laser back to the required frequency.

Figure (3.13) visualises how the laser is locked about half way on the side of the reference etalon peak and about two thirds from the maximum of the low finesse slave etalon. The absorption spectrum of molecular iodine [51] is employed to provide an absolute reference frequency as the etalon peaks can drift over a long time period.

In this base-locking technique, the laser is locked to the bottom of the iodine absorption peak. A small dither signal is applied to the laser frequency, (figure (3.14)) the transmitted light intensity ideally varies with twice the frequency of the input voltage. The resulting signal is divided by a reference signal to account for fluctuations in the laser output power. A phase-sensitive detector (PSD) is used to compare the input and output voltage. If the laser frequency drifts, the phase-sensitive detector will record an output signal with the same frequency as the input signal and a correction signal is sent to the optical components in the laser cavity and the optical path length is adjusted.

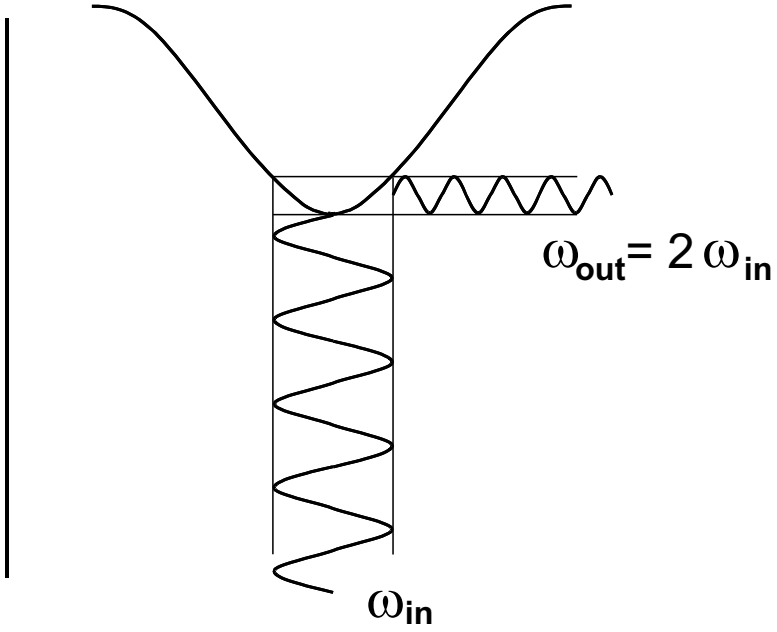

Figure 3.14: An oscillating voltage is applied to the laser. The frequency is adjusted to sit base of an iodine peak for the purpose of frequency stabilisation. The frequency and phase of the output signal allows to determine when the laser is off lock.

3.4.3 The Titanium-Sapphire laser

At the stage of optical pumping in the cooler the ionic transitions are subjected to considerable Doppler broadening due to thermal motion. A laser system with a broad linewidth is required to cover this broadening. Also, a high powered laser is necessary since the experimental setup requires transporting the beam a long way to its experimental application site and the transition should still be saturated. The solid state laser system, whose lasing medium is a titanium doped aluminium oxide Al_2O_3 crystal, (TiSa) provides both these features.

The solid state Titanium-Sapphire laser system used was developed by a collaboration of the Universities of Mainz, Germany, and Jyväskylä. It is pumped by a

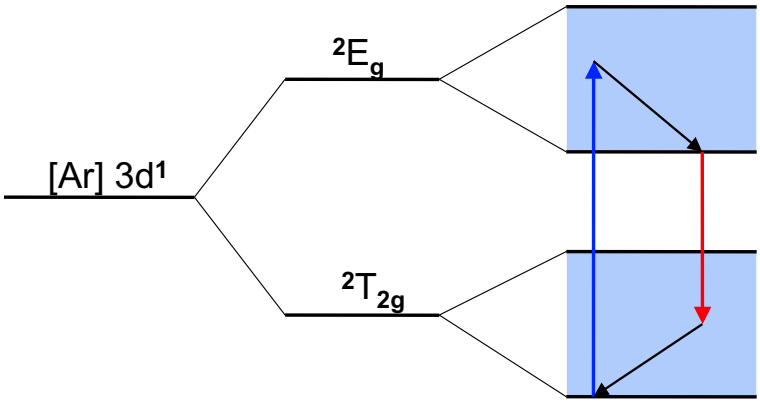

Figure 3.15: The band structure in a $Ti : Al_2O_3$ - crystal [53]. In the crystal lattice, the degeneracy of the $3d$ levels of the free Ti^{3+}-ion is lifted and the electron levels split into so-called ^2E_g and $^2T_{2g}$- levels. These levels are broadened by electron-phonon interactions.

pulsed Nd:YAG laser (Lee Laser) at a repetition rate of 10kHz and at a wavelength of 532 nm [52]. The Nd:YAG is a Q-switched laser which is operated at 10 - 20 W and an average energy of 1mJ in a pulse of $30 - 50$ ns length.

The pumping wavelength lies close to the absorption maximum of the TiSa crystal. Figure (3.15) shows the band structure of the $Ti : Al_2O_3$ crystal.

The free Ti^{3+}-ion possesses a $3d$ valence electron outside an argon-like configuration. When implanted into a Al_3O_3 crystal, the 10-fold energy degeneracy of the $3d$ level is lifted and so-called ^2E_g and $^2T_{2g}$ - levels are formed. The split energy levels are widened through electron-phonon interactions in the crystal lattice, leading to a quasi-continuous band of energy levels [53].

Population inversion is achieved by raising the electrons into the higher states of the upper energy band where it relaxes to the bottom of the band via non-radiative processes within picoseconds. Laser photons are emitted when the electrons drop

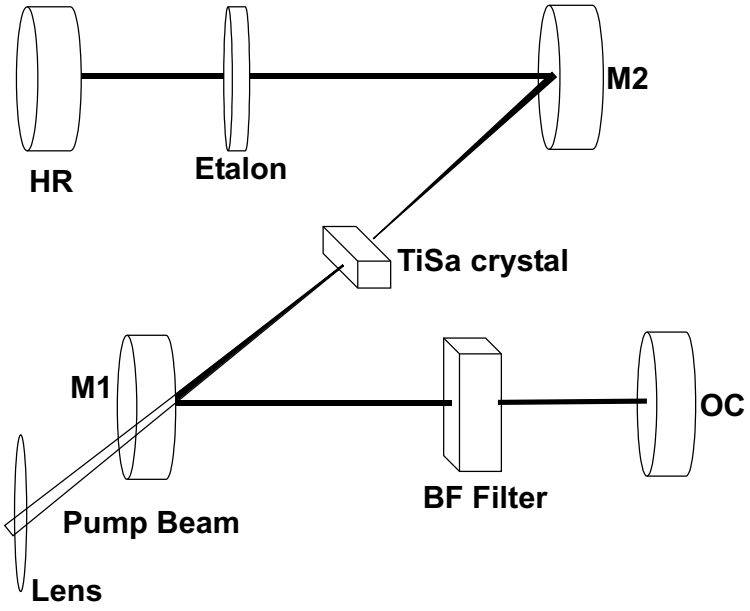

Figure 3.16: The Cavity of the Titanium Sapphire Laser

back into the various states of the ${}^2T_{2g}$-band. The continous output spectrum produced lies in the range of $690 - 1000$ nm [54].

The Z-shaped cavity is shown in figure (3.16). It consists of two resonator mirrors $M1$ and $M2$, a highly reflecting end mirror HR as well as an output coupler OC which provides the outgoing laser beam. The pump beam is introduced into the cavity through the back of mirror $M1$ and focused onto the crystal. Since the frequency output of the crystal is continuous a birefringent crystal (BF filter) is introduced into the cavity for broad frequency selection. Further, an antireflection coated thin etalon is used to constrain the competing modes as in the case of the dye laser cavity. The mirrors $M1$ and $M2$ are coated with dichroic material which transmits the pumping wavelengths and reflects the longer TiSa wavelength and thus decouples the pump beam from the infrared laser beam.

Three different TiSa lasers can be operated at the same time. The bandwidth of

the produced laser light is about 5 GHz which easily covers the Doppler broadened hyperfine structure. The typical output power of the fundamental is in the order of 2 Watts. Using different sets of mirrors, a wavelength range of about 720-930 nm has been covered.

Second Harmonic Generation

For experimental purposes the output light is frequency doubled, tripled or even quadrupled. Where the frequency doubling process has to take place inside the cavity in case of the dye laser to make use of maximised power density, the TiSa laser possesses an external frequency doubling and frequency tripling unit. Figure (3.17) shows the setup of the frequency tripling unit. The fundamental wavelength is focused onto a first frequency doubling crystal (β-Barium-Borate) and a ray of blue light is produced. The red fundamental and the blue ray are split using a dichroic mirror that only reflects the blue ray. As the polarisation of the doubled light is rotated by 90° with respect to the fundamental, a $\lambda/2$-plate is used to bring both polarisations into the same plane. The light rays are then re-united and focused onto a second β-Barium-Borate crystal where the photons of each ray coalesce into photons with three times the frequency of the fundamental. Frequency quadrupled light is produced by sending frequency doubled light through a second doubling crystal. The shortest wavelength that was experimentally achieved by quadrupling the fundamental was 205 nm [55].

Optical Pumping

For the purpose of optical pumping the beam of the TiSa laser is introduced into the ion beam cooler. The required light power to saturate the transition in the cooler is a few mW which is easily achieved. The linewidth of the TiSa light increases in the frequency multiplication process. The uncertainty in the laser linewidth is in

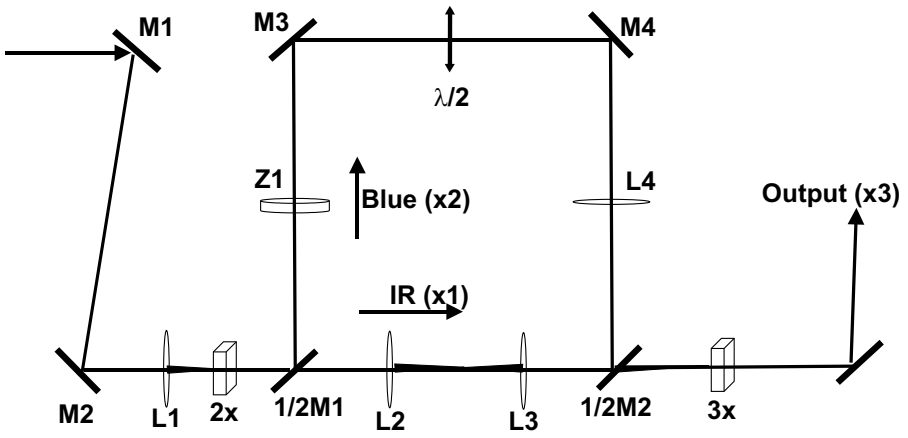

Figure 3.17: Scheme of the frequency tripling device. M_i are mirrors, L_i are lenses, Z1 is a cylindrical lens, $\lambda/2$ is a $\lambda/2$ - plate and 2x and 3x refer to the β-Barium-Borate crystals that are responsible for the doubling and tripling processes of the incoming light.

the order of 5 - 10 GHz and broad enough to cover the Doppler broadened ionic transition in the cooler.

Chapter 4

NIOBIUM EXPERIMENT

Offline tests are necessary as preliminary work to experiments. Stable samples of the element in question are introduced into the IGISOL and atomic transitions are tested for efficiency.

4.1 Selection criteria for a transition

In order to successfully probe transitions with the high resolution dye laser it is necessary to find a transition that provides the best efficiency. Here, the efficiency is defined as

$$\text{efficiency} = \frac{\text{number of ions/second}}{\text{number of photons/second}} \tag{4.1}$$

Criteria for suitable transitions are usually:

- the transition strength: a high A-value is desirable;
- a high population of the lower energy level. As the atomic level population in thermal equilibrium follows a Boltzmann distribution, atomic ground states usually provide the highest population. If spectroscopy should be done from energy levels other than the ground state, these may have to be artificially populated;

- the wavelength of the transition has to be accessible with enough power from the dye laser system. The dye laser can conveniently access wavelengths between 570 nm and 728 nm (285 nm to 364 nm doubled);

- the angular momentum of the lower and upper atomic levels involved should be relatively low as the total intensity of the transition is spread out over all hyperfine components. Therefore, too many hyperfine components may make the transitions unsuitable. On the other hand, any $J = 0 \rightarrow J = 1$-transition will give a hyperfine structure of at most three peaks. In an experiment in neutron-rich yttrium this proved an insufficient number of peaks in order to fit all parameters and it was not possible to unambiguously assign the spins in ^{100}Y and ^{102}Y [56]. For this reason the experiment had to be repeated at a later date using another transition [11].

4.2 Offline tests

A number of transitions in niobium were tested offline before the actual experiment. Only one ground state transition was accessible with the dye laser, all other transitions start from metastable states and can be expected to benefit from optical pumping (table (4.1)). The ground state transition proved weak when investigated further (table (4.2)).

In all these lines, the biggest hyperfine structure component was scanned without optical pumping. If the efficiency looked promising, further investigation of the whole transition was done using optical pumping in the cooler. The efficiency on the biggest hyperfine structure peak is generally more meaningful than the total transition efficiency as the total efficiency distributes over all hyperfine structure peaks. Hence, even a strong transition can appear weak and unsuitable if many hyperfine components are present.

Table 4.1: Possible spectroscopy lines in niobium [57]

Wavelength (nm/air)	A-value (1/s)	E_{lower} (cm^{-1})	Configuration	E_{upper} (cm^{-1})	Configuration
286.1091	2.046e+08	2356.760	5s $^5F_1$	37298.200	5p $^5D^o_0$
286.5611	1.630e+07	0.000	4d^4 $^5D_0$	34886.330	5p $^3D^o_1$
286.8519	1.417e+08	2629.070	5s $^5F_2$	37480.030	5p $^5D^o_1$
287.8731	1.092e+07	158.990	4d^4 $^5D_1$	34886.330	5p $^3D^o_1$
287.9385	6.551e+06	801.380	4d^4 $^5D_3$	35520.830	5p $^3D^o_2$
290.8237	1.201e+08	2356.760	5s $^5F_1$	36731.790	5p $^5F^o_1$
319.4972	1.148e+08	2629.070	5s $^5F_2$	33919.200	5p $^5G^o_3$
320.6342	6.867e+07	7505.780	5s $^3F_2$	38684.960	5p $^3G^o_3$
322.5475	1.196e+08	2356.760	5s $^5F_1$	33351.000	5p $^5G^o_2$

The pumping wavelength of the Titanium:Sapphire laser was set to excite the transition 4d^4 $^5D_0$ (0.00 cm^{-1}) $\rightarrow$ 5p $^3D^o_1$ (34886.330 cm^{-1}) at 286.5611 nm. This transition is particularly suitable for pumping as it directly populates many of the lower lying states with spins $I = 0, 1$ and 2. One of the populated states is the 2356.760 cm^{-1} 5s $^5F_1$ -level which can then act as a starting point for spectroscopy. Figure (4.1) shows the pumping scheme used to populate the 5s $^5F_1$ (2356.760 cm^{-1}) - state which is then used to probe the 5s $^5F_1$ (2356.760 cm^{-1}) $\rightarrow$ 5p $^5F^o_1$ (36731.790 cm^{-1}) transition at 290.8237 nm. Electric dipole transitions between low lying metastable states are forbidden by parity considerations, but de-excitation can take place via collisions.

Collisions mainly take place in the beam cooler where the ions are cooled to thermal energies. The number of collisions is drastically increased when the bunching potential is applied and the ions are held in the cooler for up to 200 ms. At this point any significant metastable population that may be present is expected to relax back into the ground state. It is at this stage where the introduction of the pumping beam is crucial in order to hold the population of that particular metastable state that should be used for spectroscopy.

The results of the offline investigations are displayed in table (4.2). As the table

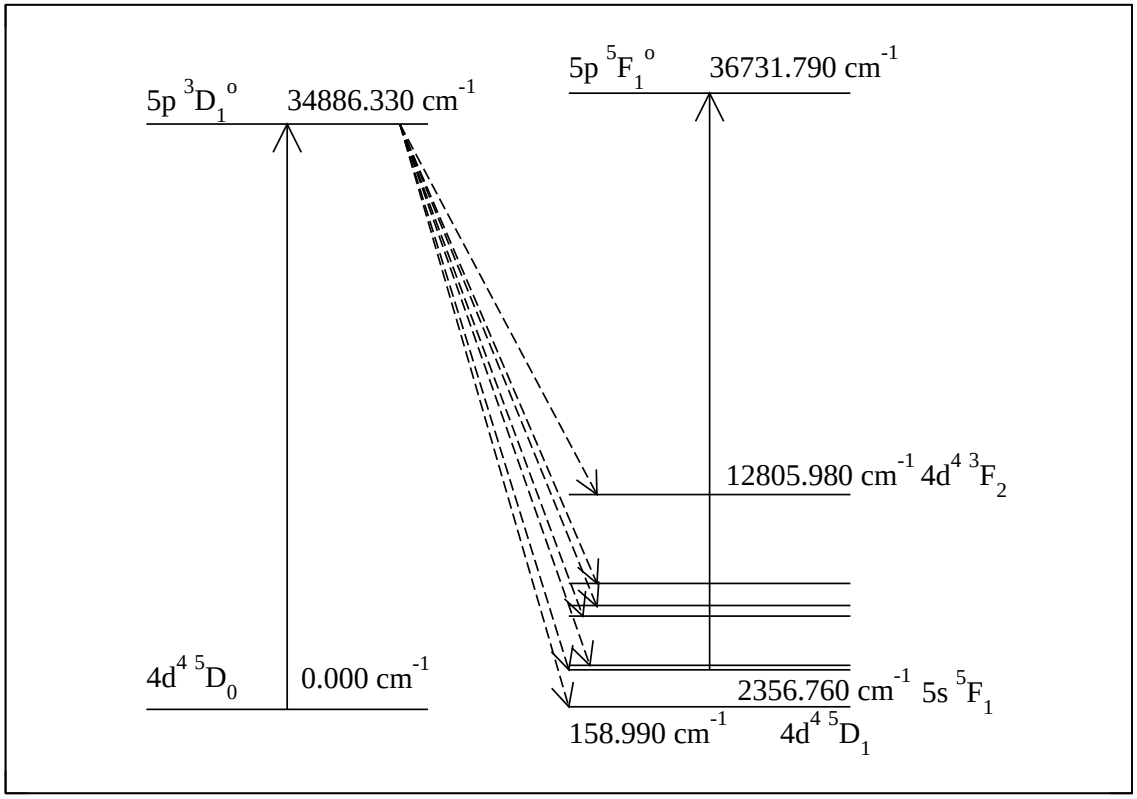

Figure 4.1: The pumping scheme and the transition used for laser spectroscopy in niobium.

shows, the lines 2356.760 cm^{-1} 5s $^5F_1 \rightarrow$ 36731.790 cm^{-1} 5p $^5F_1^o$ at 290.8237 nm and 2356.760 cm^{-1} 5s $^5F_1 \rightarrow$ 33351.000 cm^{-1} 5p $^5G_2^o$ at 322.5475 nm seem both equally suitable. The decision was made in favour of the 290.8237 nm transition on grounds of the hyperfine structure: As figure (4.2) shows, its hyperfine structure has fewer components due to the lower spin of the upper state and is therefore narrower. It also possesses two very pronounced doublets. This means that less scan time is needed to cover the transition. The intensity of the transition versus pump power was investigated to ensure that the pump beam is able to saturate the atomic transition. The power was measured directly behind the tripling unit. The graph is shown in figure (4.3). As the beam of the TiSa laser is led over a long distance, power losses occur along the way when the beam is reflected on several mirrors. The power that arrived inside the beam cooler may not be more than a

Table 4.2: Efficiency of the tested spectroscopy lines

Wavelength (nm/air)	A-value (1/s)	efficiency without pumping	efficiency with pumping	efficiency with bunching
286.1091	2.046e+08	1 in 70500		
286.5611	1.630e+07	1 in 182000		
286.8519	1.417e+08	1 in 98000		
287.8731	1.092e+07	1 in 570000		
287.9385	6.551e+06	not detectable		
290.8237	1.201e+08	1 in 37500	1 in 11000	1 in 6700
319.4972	1.148e+08	1 in 35000	1 in 23000	
320.6342	6.867e+07	not detectable		
322.5475	1.196e+08	1 in 14600	1 in 9400	1 in 6750

few mW.

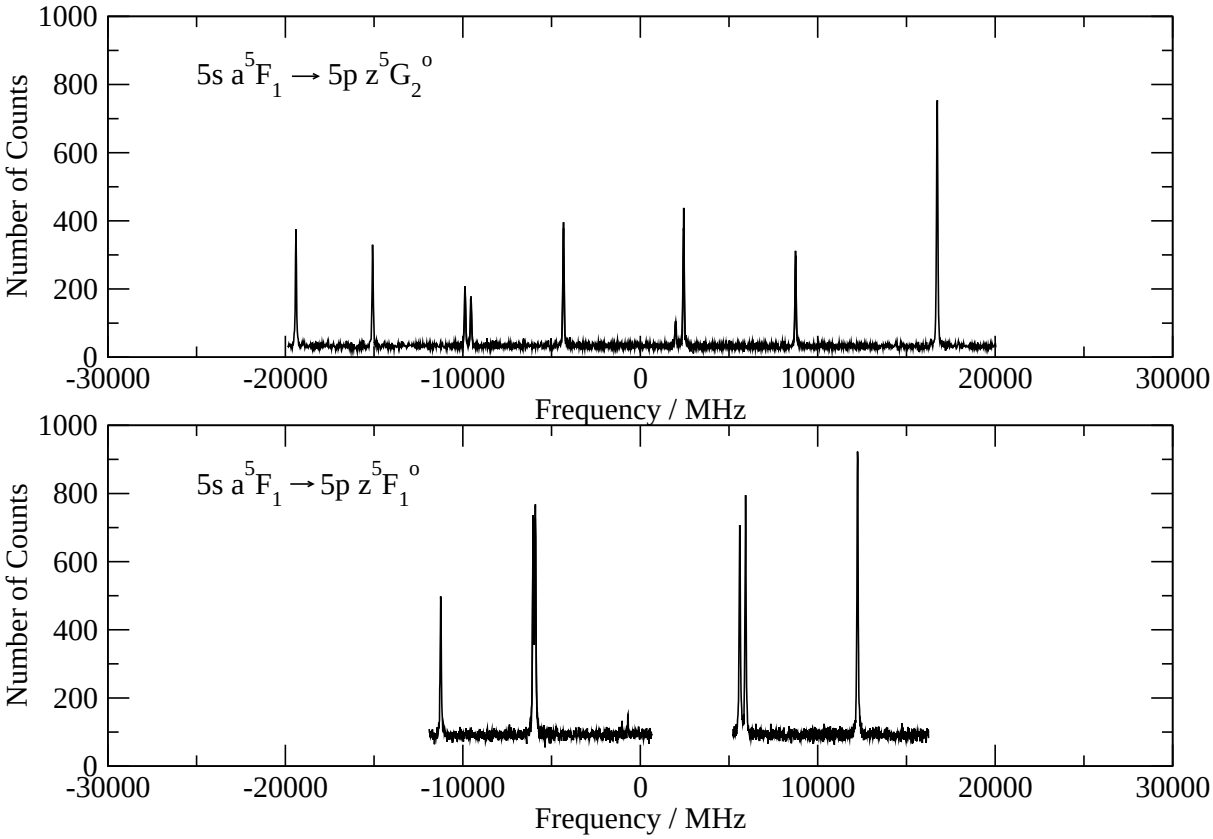

Figure 4.2: The spectra for the 5s $^5F_1$ (2356.760 cm^{-1}) $\rightarrow$ 5p $^5F_1^o$ (36731.790 cm^{-1} and the 5s $^5F_1$ (2356.760 cm^{-1}) $\rightarrow$ 5p $^5G_2^o$ (33351.000 cm^{-1}) transitions (290.8237 nm and 322.5475 nm respectively)

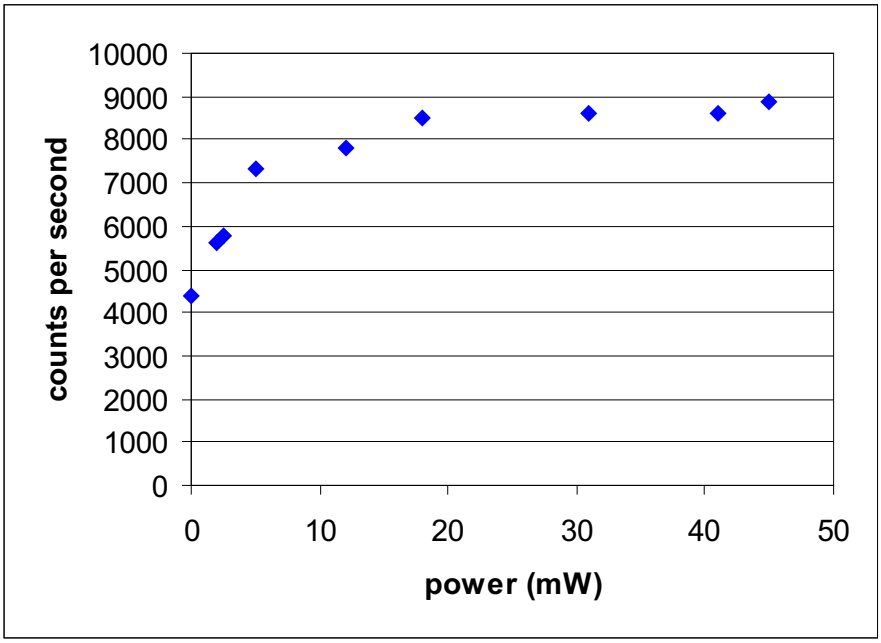

Figure 4.3: Intensity curve of the atomic transition $4d^4\ {}^5D_0$ (0.00 cm^{-1} $\rightarrow$ $5p\ {}^3D_1^o$ (34886.330 cm^{-1}) at 286.5611 nm as a function of TiSa output power.

4.3 Online Experiment

A proton beam of 30 MeV energy and 6.2 μA intensity was directed onto a natural uranium target in the IGISOL to give a $U(p, f)$-reaction. Natural uranium contains 99.3 % of ^{238}U which has got a fission cross section of 1.536(31) barns at 30 MeV [58]. It has been found that the valley of the assymetric yield-curve of uranium fission products increasingly flattens for higher fission energies [14]. At 30 MeV the two maxima are still present with one of them peaking at $A \simeq 100$. Rinta-Antila [59] demonstrates that zirconium is the most dominant isotope in the $A = 100$ isobars under the given conditions. The separation foil in the fission ion guide contained a strip of stable ^{93}Nb. In the course of the reaction they are knocked out by the reaction products and provide a reference beam of $^{93}Nb^{+}$. Before actual laser measurements could be taken, the settings along the beam line had to be optimised and calibrations had to be carried out.

The main aim was to optimise both the beam transport of the ions along the beam line and the spectroscopic efficiency. These are mainly governed by the gas pressure inside the ion-guide and the cooler. As a first step the helium pressure in the IGISOL and the settings of the SPIG needed to be adjusted to give the optimum extraction of the radioactive ions into the beam line. The produced fission fragments carry a high momentum and need to be slowed down, re-combine with the electrons and be carried out off the IGISOL. For this reason a higher helium pressure is required than for offline work where the ions are produced in a lower charge state and the momentum carried by the products is significantly lower. Due to this different production mechanism, the population of metastable states is also expected to differ. A helium pressure of about 250 mbar was found to give the best result for the extraction. The ion current leaving the IGISOL was measured on a Faraday cup behind the mass separating magnet. The mass separating magnet itself was calibrated using the inert gas xenon.

The next step was to find out which isotopes were being produced in the $U(p, f)$-reaction. For this reason the ion beam with the fission products was steered through the cooler at an initial pressure of 3.6 mbar and onto a beam stop in front of a high resolution germanium detector. The fission products pile up in front of the gamma detector and most of them quickly decay via β-decay. During the decay process a cascade of gamma rays is produced by the de-exciting daughter nuclei. The total probability for the emission of a γ ray is expressed by the Iγ%, which is the product of the branching ratio and the relative intensity, i.e. the probability for a nuclear level to be populated times the probability of the level to decay while emitting a γ ray. Since we are talking about many γ rays, the observed peak intensity on the γ detector is directly correlated to the probability for that decay path. Usually the strongest γ rays of a particular nucleus are used to identify the mother and daughter nuclei. In this experiment, γ rays of zirconium, niobium and molybdenum isotopes could be identified.

The optimisation of the ion beam was then carried out on mass A = 99 using the 121.7 keV γ ray that is visible in zirconium from yttrium β^--decay. Using the 121.7 keV γ ray, the intensity of the proton beam was varied from 2 μA - 8 μA while γ measurements were taken repeatedly for 30 s. The magnet mass reading was varied in steps of a tenth of a mass unit until the maximum ion yield was found. Then the cooler inlet pressure was optimised to give optimum transmission. The final settings used in the experiment were a proton beam intensity of 6.2 μA and a cooler pressure of 2.7 mbar.

The total ^{99}Y ion rate passing the cooler can roughly be estimated from the observed γ rate. The final rate of the 121.7 keV γ-ray in steady state was about 200 γ/s. The γ -detector efficiency for a 100 keV γ-ray may not be better than 20%. In our setup it was used at a 90 $^\circ$ angle to the incoming beam and due to the solid angle the overall efficiency may not be better than 10%. This suggests a total of

2000 γ's emitted per second. The absolute intensity of the 121.7 keV γ-ray is 46.9%. This suggests a total of about 4200 ions/s of ^{99}Y being present in the beam. A later reading on the microchannel plates at the end of the beam line gives a total number of 20000 ions/s for $A = 99$.

A similar calculation for ^{101}Nb using the 276.2 keV γ ray suggests a number of about 750 niobium ions/s being present in the beam. This is based on the observation of 466 γ's in 30 s and a branching ratio of 21%. The microchannel plates on the end of the laser beamline around that time gave readings of 4400 - 8000 ions/s. Fluctuations are due to drifts of the settings along the beam line. A = 100 isobars were recorded as 4000 - 7000 ions/s. These numbers agree with measurements of Rinta-Antila [59] that were taken in an IGISOL fission experiment with 30 MeV protons. The beam was purified in the Penning trap and the ^{100}Nb content in the A = 100 isobar amounted to a fifth of the total beam of $\sim$ 4300 ions. The true fraction will slightly change due to the short lifetime of ^{100}Y ($t_{1/2}$ = 735 ms) compared to the time it took to record a data point on the spectrum (50 cycles at 220 ms per cycle) [59].

The γ rate for different isotopes was checked on several occasions throughout the experiment. Other observed γ-rays were E_γ = 97.785 keV and 137.723 keV from ^{99}Nb decay. Also E_γ = 600.5 keV and 535.60 keV from ^{100}Nb-decay and E_γ = 296.611 keV from ^{102}Nb-decay.

Spectroscopy was done on the 5s $^5F_1$ (2356.760 cm^{-1}) $\rightarrow$ 5p $^5F_1^o$ (36731.790 cm^{-1}) -line at 290.82 nm. The dye laser was locked to the bottom of the iodine peak at 17428.6352 cm^{-1}. It was pumped at 4 Watts and gave an output of $\sim$ 1 mW UV-light. The photon background from scattered laser light was typically 250 photons/second with fluctuations between 200 photons/seconds and 350 photons/seconds in some of the scans. The TiSa produced a fundamental wavelength of λ = 859.9353 nm which was tripled to give a wavelength of λ = 286.5611 nm

Table 4.3: Nuclear Data of the investigated neutron-rich niobium isotopes according to the Table of Nuclides [60]

Mass A	Half-life $t_{1/2}$	State (MeV)	Spin, Parity I^{pi}
93	stable	0.000	$9/2^+$
99	15 min	0.000	$9/2^+$
99^m	2.6 min	0.365	$1/2^-$
101	7.1 s	0.000	$(5/2^+)$
102	1.3 s	0.000	1^+
102^m	4.3 s	0.000	
103	1.5 s	0.000	$(5/2^+)$
105	2.95 s	0.000	$(5/2^+)$

($4d^4\ {}^5D_0$ (0.000 cm^{-1}) $\rightarrow$ $5p\ {}^3D_1^o$ (34886.330 cm^{-1})). The power of the frequency tripled light behind the tripler was 15 mW. The time taken to scan isotopes ^{99}Nb, ^{101}Nb, ^{102}Nb and ^{103}Nb was more than 36 hours with 18 hours for ^{99}Nb alone.

Chapter 5

ANALYSIS AND RESULTS

During the experiment, spectra of the isotopes ^{99}Nb, ^{100}Nb, ^{101}Nb, ^{102}Nb, ^{102m}Nb and ^{103}Nb were taken. The most intense, highest frequency component (right-hand side of the scan) in the hyperfine structure of ^{93}Nb was used for calibration and regularly re-scanned in between scans of the radioactive isotopes. The fit of the hyperfine structure is necessary not only for the extraction of the magnetic moment and the quadrupole moment but also for the extraction of the centroid of the transition. The frequency difference between the centroid of the transition and that of a reference isotope is the isotope shift.

For the measurements, the ions are accelerated to the light collection region. For each ion bunch, the acceleration voltage is ramped by a step and the number of detected flourescent photons is stored in a data channel. In this way, the laser frequency repeatedly scans across a region and repeated scans make a run. In the analysis, the runs are converted from channel number to voltage and from voltage to frequency. Scans are typically 25, 50 or 100 channels long and the voltage applied is 1 - 2 Volts/channel, where 1 V $\sim$ 14 MHz (for this mass region and acceleration voltage).

5.1 Analysis of ^{99}Nb-spectra

Having the same spin, $I^{\pi} = 9/2^{+}$, as ^{93}Nb, the ^{99}Nb-isotope will also have seven hyperfine components. Under the assumption that hyperfine anomalies are negligible, the ratios of A_u/A_l and B_u/B_l from ^{93}Nb will be constant across the isotopic chain. This reduces the number of free parameters and a scan of 3 components in the ^{99}Nb hyperfine structure (hfs) should be sufficient to determine the respective A and B coefficients and the centroid position of the structure. During the experiment, the most intense component on the right-hand side and a doublet on the right-hand side of the expected centroid of the transition were scanned. The recorded spectrum is displayed in figure (5.1). Between runs, calibration scans of a peak in ^{93}Nb were taken. The conversion of all the calibration peaks of ^{93}Nb revealed that a big jump of nearly 83 MHz (about 3 channels) had occurred between two calibration peaks as shown in figure (5.2).

Smaller drifts of up to about 10 MHz (about 0.5 channels) are not unusual due to drifts of the laser frequency along the base of the locking iodine peak or a shape change of the locking iodine absorption peak due to temperature variations. A full investigation on temperature effects on iodine absorption spectra can be found in the thesis of B Cheal [61]. The big frequency jump affects all scans taken before or after the jump and all data for the ^{99}Nb isotope now fall into two groups, one before and one after the shift. As in between measurements of molybdenum had taken place and interrupted the niobium measurements, it could be that slight changes in steering and adjustment of the equipment can be held accountable for the occurrence of the jump. A second jump of this magnitude cannot be observed anywhere else in the data set. The size of the jump was determined by evaluating all of the ^{93}Nb-calibration peaks and taking the weighted means of seven peaks before and six after the jump that are directly enclosing relevant spectra.

Usually, different scans of the same region can be summed up in order to use

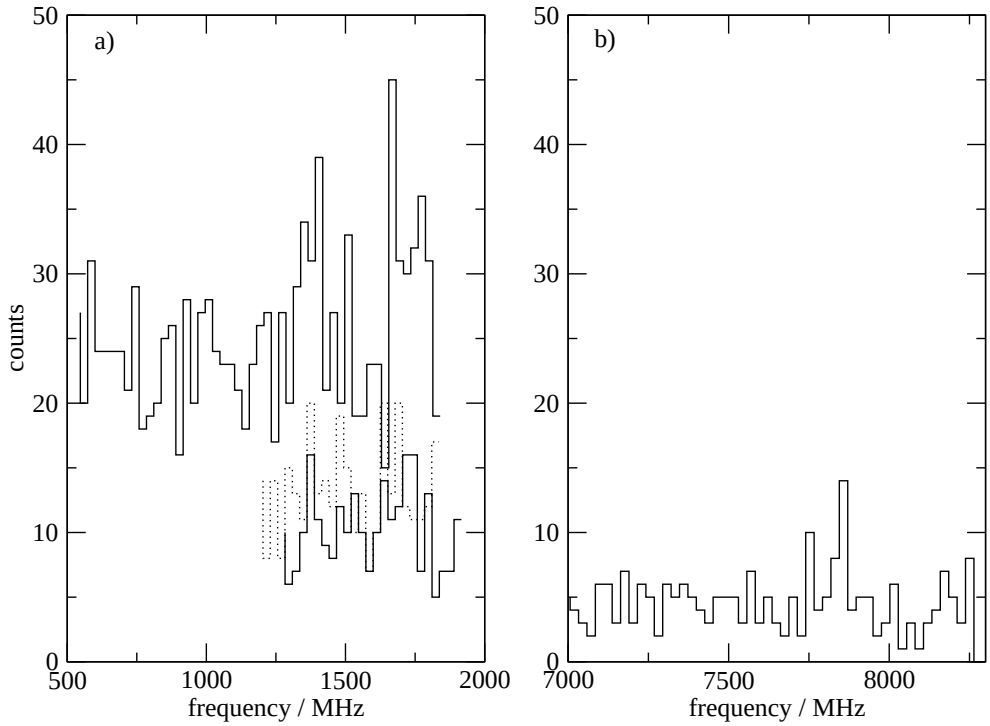

Figure 5.1: ^{99}Nb hyperfine structure: a) RHS doublet b) RHS component. The RHS doublet was scanned several times and for the hfs fit the scans were grouped into three sets: The long 50 ch spectrum incorporates 3078 scans before the big frequency jump, the 25 ch spectrum (dotted) contains another 1449 scans; the third 25 ch scan (solid line) represents the 903 frequency corrected scans that were taken after a frequency jump of 82.87 MHz had occurred. This jump was then accounted for by shifting the spectrum.

all available information. For a summation, scans need to have the same number of channels. Unfortunately the data of the spectra taken of the doublet structure are of relatively poor quality. In order to double-check that the spectra taken indeed contain real information, a statistical analysis was performed before the actual analysis of the hyperfine structure spectrum. This was done using a sum of full 50 channel scans before the frequency jump and incorporated 3078 scans (see figure 5.3).

The total number of scans performed for the doublet region was 5430. However, this also includes 25 channel scans that cannot be included in the same statistical analysis as the 50 channel scans. It was assumed that all background in the spectrum

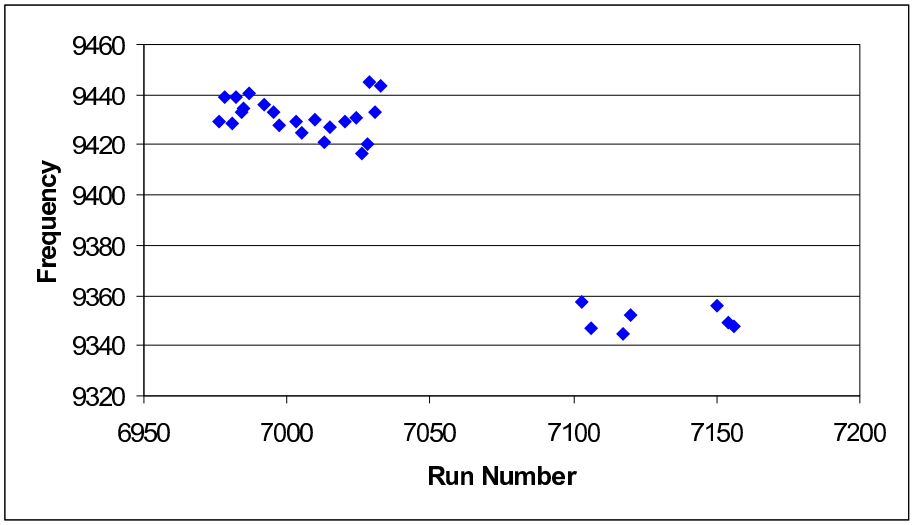

Figure 5.2: The frequency position of the ^{93}Nb calibration peaks that were taken before and after every scan of a ^{99}Nb component. The big gap in run numbers is due to measurements of molybdenum that took place in the intervening time. A big and sudden shift of about 83 MHz occurred after those measurements. The error in the frequency positions is of the order of 3 MHz and has been omitted for clarity.

should be Poisson distributed with the same mean value. The average number of counts for a channel was calculated to be $\bar{x}_{exp} = 25.14$. For this test we expect the existence of an ideal Poisson distribution with the same mean value as the experimentally obtained mean value, i.e. we require $\bar{x}_{exp} = \bar{x}_{predicted} = \bar{x}$. For a Poisson distribution, $\bar{x}$ can be identified with σ^2, the predicted variance of the distribution. The real spread of the data taken is calculated as

$$s^2 = \frac{1}{N-1}\sum_{i=1}^{N}(x_i - \bar{x})^2 \tag{5.1}$$

where N is the number of channels. This gave $s^2 = 37.47$.

The ideal and the real distribution of the data points can be compared using the χ^2-method [62]. χ^2 is defined as

$$\chi^2 = \frac{(N-1)s^2}{\sigma^2} = \frac{(N-1)s^2}{\bar{x}}, \tag{5.2}$$

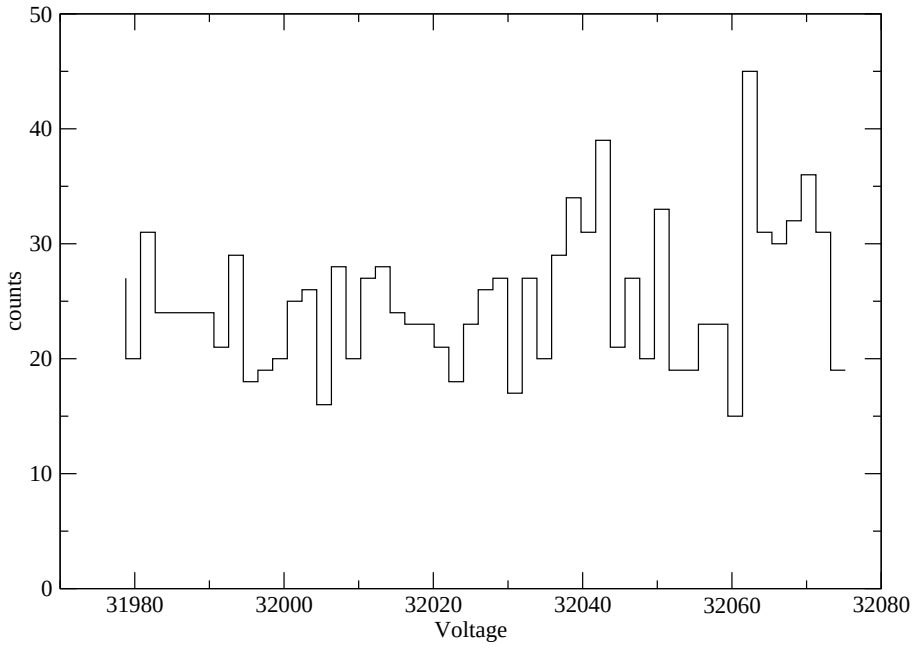

Figure 5.3: ^{99}Nb hyperfine structure component: RHS doublet, sum of full 50 channel scans.

where $(N-1)$ is the reduced number of degrees of freedom (d.o.f). The χ^2 - method compares the two variances in order to decide how likely the recorded data are indeed Poisson distributed. For data that can be perfectly described by a Poisson distribution (and hence contains mere background) we would expect

$$\frac{\chi^2}{(d.o.f)} = \frac{s^2}{\bar{x}} \simeq 1 \tag{5.3}$$

For the 50 channel scans, $\chi^2/(d.o.f.) = 1.49$. Using a chi-squared distribution table (p-table) [63], one can find the probability, p, that a random sample from a true Poisson distribution would have a larger value of χ^2 than the specific value shown in the table [62]. For the 50 channel scan, p = 0.015, indicating that the fluctuation of the data points in the spectrum was abnormally large. The spectrum was then divided into two 25 channel parts. The left half showed $\bar{x} = 23.32$, $\chi^2 = 0.62$ and p = 0.9. The p-probability indicates that the data in this part of the

spectrum are showing very small fluctuations, even for a Poisson distribution. For a perfect fit of the ideal Poisson distribution, p = 0.5 would be expected. Hence, the left half of the spectrum is quite doubtless mere background. For the right half of the spectrum, $\bar{x} = 26.96$, $\chi^2 = 2.04$ and p = 0.001. This is an extremely small probability, indicating very large fluctuations in the measured spectrum. It is fundamentally different from the distribution of the left half of the data points. The conclusion is that the unusually large fluctuations in the background can be connected to the presence of non-background components, i.e. we are seeing real peaks in this spectrum. This would be the doublet structure that we are looking for.

For the hyperfine structure analysis, the spectra taken of ^{99}Nb were combined as follows: all high intensity right-hand side components were evaluated and the most likely distance to the ^{93}Nb-calibration peak was determined by taking the weighted mean of all spectra available. For the right-hand side doublet, the 50 channel spectra of the doublet before the jump were added up and converted to frequency. Additionally, a 25 channel run from before the jump was taken into account, as it consisted of 1449 single scans (dotted line, figure (5.1 b)). As a third spectrum, the sum of 903 25-channel scans was taken into account that had been measured after a frequency jump of 82.87 MHz had occurred (25 channel spectrum, solid line in figure (5.1 a)). This spectrum was shifted to account for the jump. In the fitting program *xmgrace* (as modified by Dr D H Forest, University of Birmingham) it is possible to incorporate all these spectra into the same hyperfine fitting routine and take them into account at the same time. The program can then find the most likely position for the doublet and the single peak on the basis of all spectra incorporated into the routine.

^{99}Nb possesses a $I = 1/2^-$ isomer at 0.365 MeV. Experiments have shown that fission reactions preferentially populate states with high angular momentum. Given

the poor quality of the recorded spectrum it was assumed that the present peaks belong solely to the $I = 9/2^+$ state and that the $I = 1/2^-$ structure was not sufficiently populated to be detectable.

5.2 Analysis of ^{101}Nb

^{101}Nb is an odd-even nucleus with the spin arising from a single unpaired proton. It has been assigned a spin of $I = (5/2)$ which is yet to be confirmed [60]. With the same upper and lower J of the atomic levels as before we expect seven hyperfine components and we expect the overall structure to look similar to the ones in ^{93}Nb and ^{99}Nb. The components that were recorded were the left-hand side doublet, the right-hand side doublet and the far right component. There was no significant drift in the ^{93}Nb - calibration peaks and all relevant spectra were directly summed and converted into frequency. On first sight it seemed that the LHS doublet structure shows two very different intensities. Relative intensities of hfs components can be predicted as Racah intensities [64] and according to those, the intensities of the LHS doublet components should be about the same. In agreement to the expectation, a statistical check of the area under the recorded peaks (above background) came to: left = (30.5 $\pm$ 5.5) counts and right = (30.7 $\pm$ 5.5) counts. The intensities of both peaks are therefore very similar and the hyperfine structure was fitted on that basis. As the spin is yet to be ascertained, alternative spin assignments had to be tested and if possible rejected. The Nilsson diagram for protons suggests possible Nilsson orbits with spins $I = 1/2,\ 3/2,\ 7/2$ in the vicinity of the $I = 5/2$ state [65]. A spin of $I = 1/2$ can be ruled out straight away as this spin would only yield four hyperfine components. However, due to the absence of an isomer all five recorded peaks must be ascribed to the same nuclear state. The recorded spectrum was then fitted successively with spin assignments $I = 3/2,\ 5/2,\ 7/2$. As we do not expect a large hyperfine anomaly, the restriction that the ratios A_u/A_l and B_u/B_l

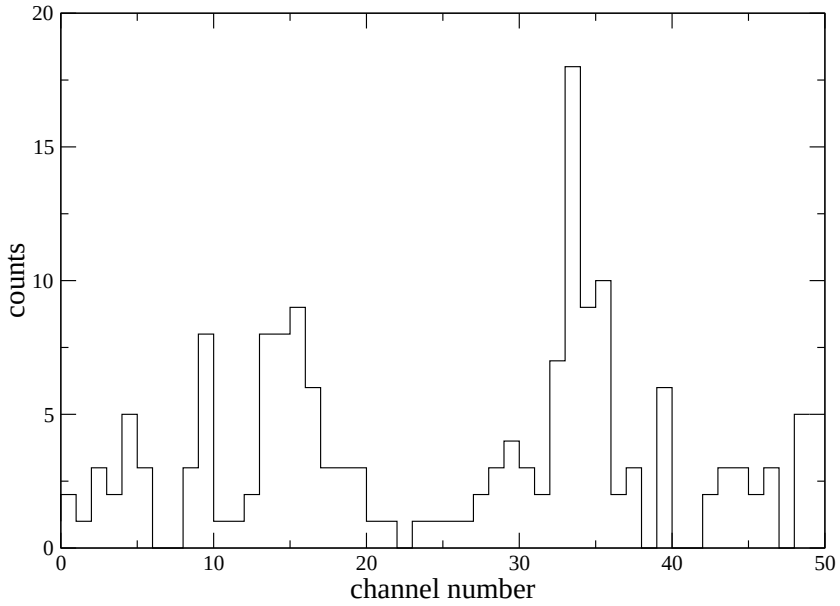

Figure 5.4: ^{101}Nb hyperfine structure components: LHS doublet.

are constant is imposed; and the only free parameters in any fit were the centroid of the transition and one of the A and one of the B coefficients. With these restrictions it was not possible to satisfactorily fit all five peaks with spin assignemts of $I = 3/2$ or $I = 7/2$. Figure (5.5) shows that in both cases either the fit of the right doublet or of the right most component could not match up with the recorded spectrum. On the other hand the doublet as well as all other peaks are perfectly well matched for $I = 5/2$. This can be counted as a qualitative proof of this being the correct spin assignment. Another indication comes from the reduced χ^2s of the fits. These are $\chi^2_r = 1.83$ and $\chi^2_r = 1.77$ for $I = 3/2$ and $I = 7/2$ respectively, whereas the one for $I = 5/2$ is $\chi^2_r = 0.635$, which is significantly better. We do expect the best fit to have the lowest χ^2_r. So this is a quantitive indication that the $I = 5/2$ spin assignment is correct.

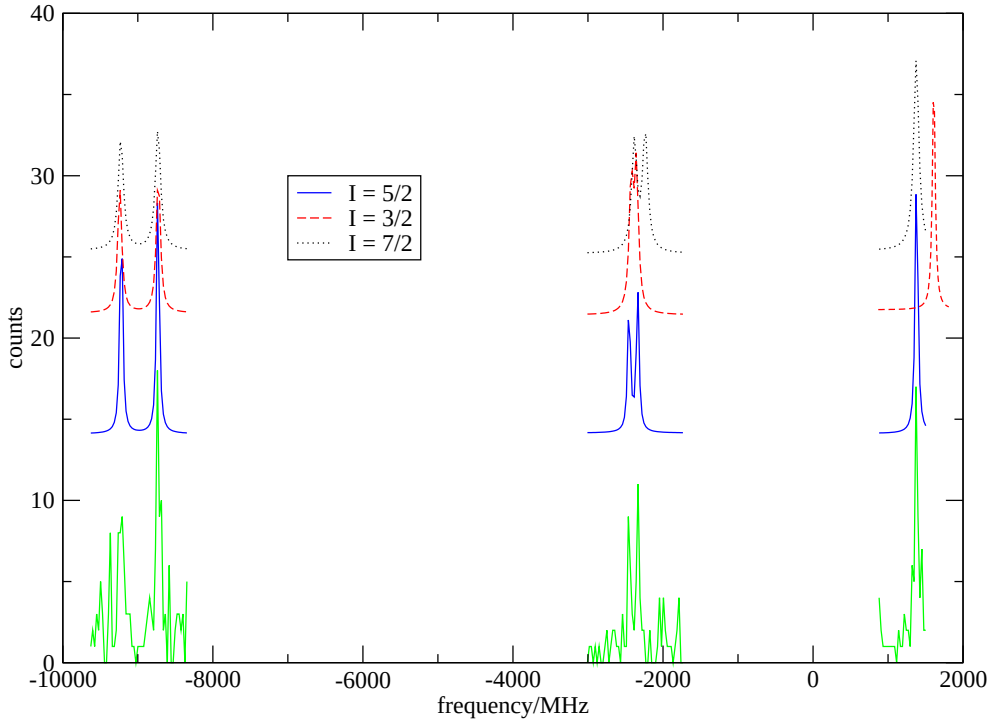

Figure 5.5: ^{101}Nb hyperfine structure fitted with different spin assignments.

5.3 Analysis of ^{103}Nb

For the ^{103}Nb isotope, the situation is very similar to the ^{101}Nb isotope. Again the spin is assigned as $I^{\pi} = (5/2)^{+}$ but is yet to be confirmed. Again we expect seven hyperfine structure components in a similar arrangement as before. Scans of the top right component, the right-hand side doublet and the left-hand side doublet were taken. The spectra for ^{103}Nb were all converted from channel number into frequency. It appears that the left peak of the left-hand side double is split into two ripples. These are two large spikes in one channel each (1 ch $\simeq$ 2 V $\simeq$ 28 MHz). It can be seen from the other peaks in the spectrum that the FWHM is about 60 MHz. Therefore, the two spikes belong to one and the same peak and do not represent two separate resonance peaks. Again $I = 1/2$ was rejected on the grounds of not yielding enough peaks to explain the recorded spectrum in the absence of an isomer.

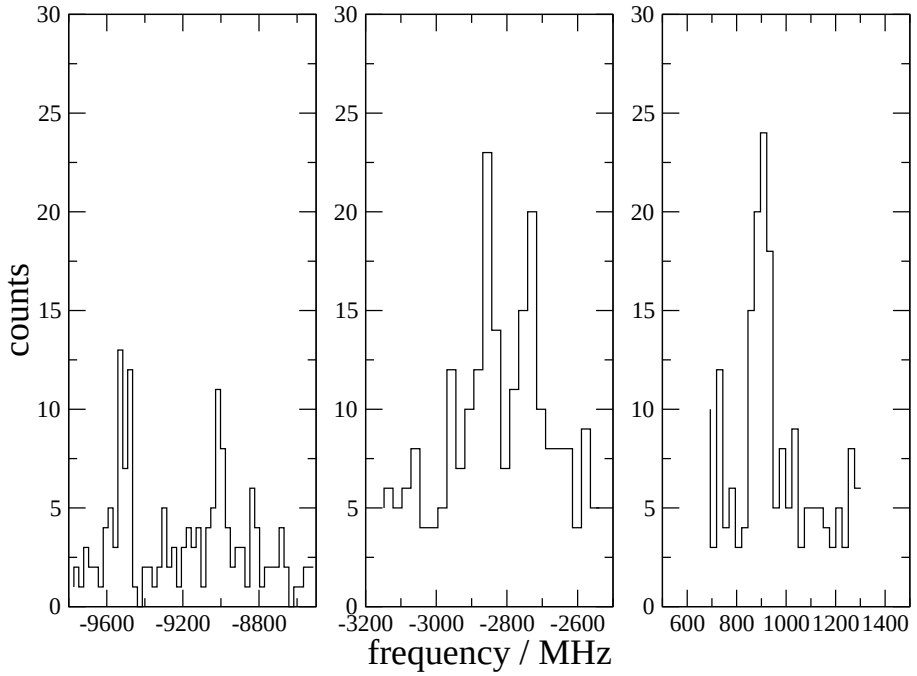

Figure 5.6: ^{103}Nb hyperfine structre components: LHS doublet, RHS double, RHS single peak.

Figure (5.7) shows that again it was not possible to satisfactorily fit all peaks at the same time using spin assignments of $I = 3/2$ and $I = 7/2$. However the fit perfectly matches for $I = 5/2$. The respective reduced χ^2s were $\chi^2_r = 1.63$, $\chi^2_r = 0.67$ and $\chi^2_r = 1.41$ for $I = 3/2$, $I = 5/2$ and $I = 7/2$ respectively. $I = 5/2$ is therefore taken as the correct spin assignment for ^{103}Nb on the grounds that is provides both the best visual fit and lowest χ^2_r.

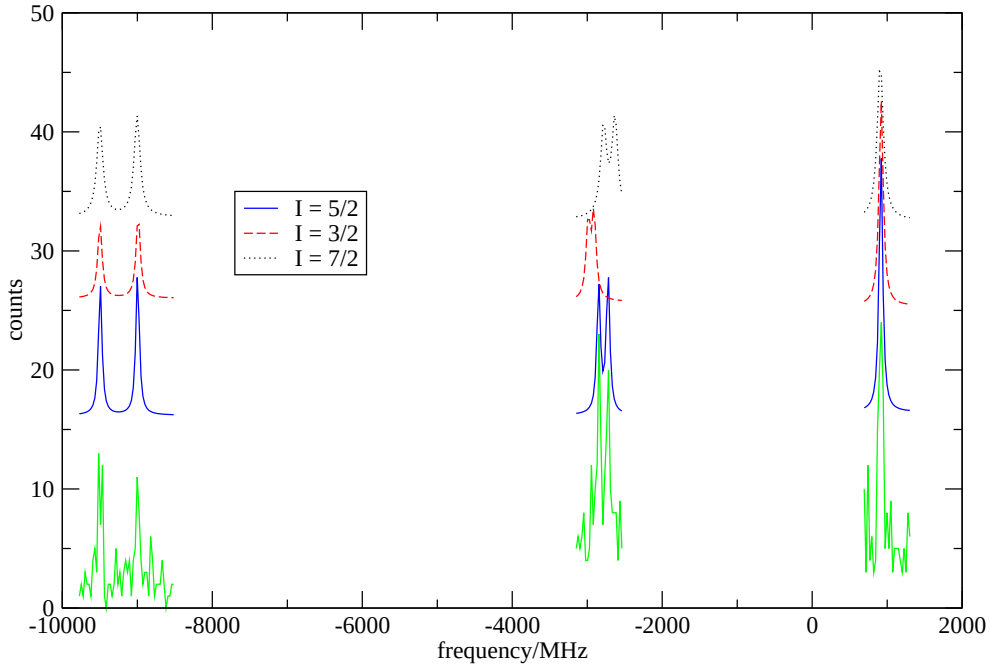

Figure 5.7: ^{103}Nb hyperfine structure fitted with different spin assignments.

5.4 Calibration and extraction of the mean square nuclear charge radius

From the fitted spectra, the isotope shifts of the radioactive isotopes were determined with respect to $A = 91$ ($N = 50$). At this point usually the mass shift and the field shift of the atomic transition are already known from a King Plot [23] calibration of the stable isotopes. The nuclear parameters of the radioactive isotopes can then be readily extracted. In the King Plot technique, all extracted isotope shifts $\delta\nu_i^{AA'}$ are modified by a factor

$$\begin{aligned} \mu &= \frac{AA'}{A'-A} \cdot \frac{A'_{ref} - A_{ref}}{A_{ref} \cdot A'_{ref}} \\ &= \frac{AA'}{A'-A}\mu_{ref} \end{aligned} \tag{5.4}$$

where A'_{ref} and A_{ref} are a reference isotope pair and A and A' are the isotopes between which the isotope shift $\delta\nu_i^{AA'}$ has been measured. The usual equation

$$\delta\nu_i^{AA'} = (\frac{A'-A}{AA'})M_i + F_i\delta\langle r^2\rangle_Z^{AA'} \tag{5.5}$$

changes to

$$\mu \cdot \delta\nu_i^{AA'} = \mu_{ref}M_i + \mu F_i \cdot \delta\langle r^2\rangle_Z^{AA'} \tag{5.6}$$

A plot of $\mu\delta\langle r^2\rangle_Z^{AA'}$ versus $\mu\delta\nu_i^{AA'}$ then displays a straight line with slope F_i and intercept $\mu_{ref}M_i$. In the case of niobium, the only stable isotope is ^{93}Nb. This is not sufficient for a pre-experimental calibration. Therefore a calibration with neighbouring elements is carried out. This method was first described by Heilig and Steudel in 1974 [26] and first employed by Fischer *et al* in 1974 [66]. It was also used by B Cheal on neutron-deficient yttrium [61]. In this method, the niobium isotope

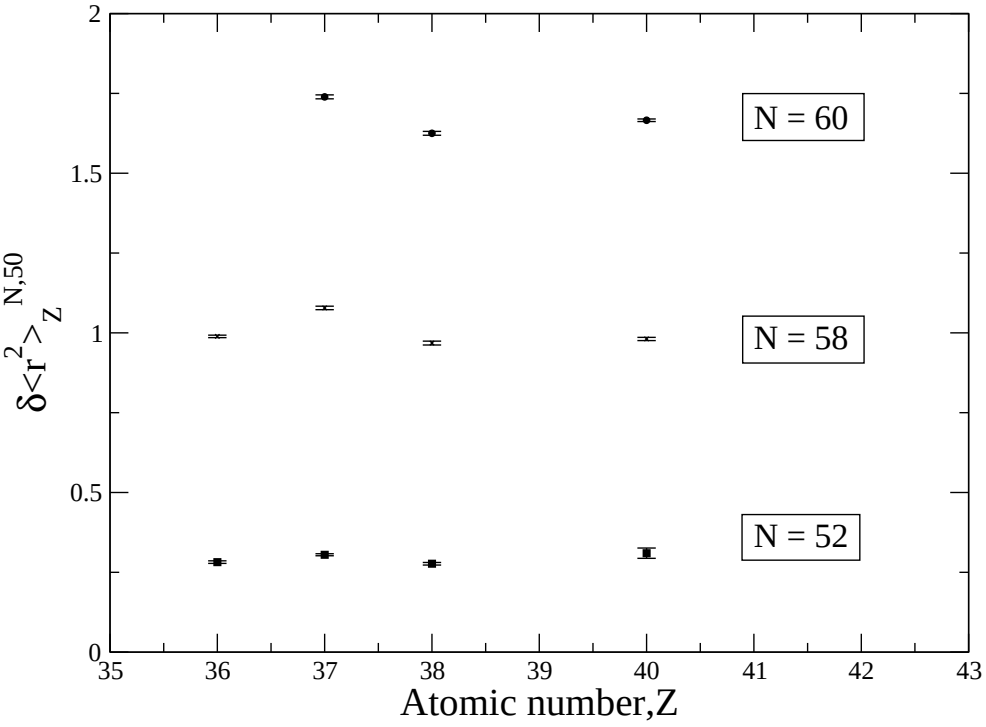

Figure 5.8: The $\delta\langle r^2\rangle_Z^{52,50}$, $\delta\langle r^2\rangle_Z^{58,50}$ and $\delta\langle r^2\rangle_Z^{60,50}$ are plotted against their respective atomic numbers in order to illustrate the scaling behaviour of the charge radii of neighbouring isotones in a small region of the nuclear chart.

shifts are plotted against the $\delta\langle r^2\rangle$-values of neighbouring isotones using the King Plot technique. Billowes and Campbell in 1995 [22] explain that this will only give a straight line if the changes in the charge radii of the neighbouring chain show a proportional behaviour to the one in question so that:

$$\delta\langle r^2\rangle_Z^{N,N+1} = K(Z')\delta\langle r^2\rangle_{Z'}^{N,N+1} \tag{5.7}$$

where $K(Z')$ is a scaling factor and $K(Z' = Z) \equiv 1$. This is the case for the elements $Z = 36$ (Kr) to $Z = 40$ (Zr) around the shell closure of $N \sim 50$. The proportional dependence with Z is illustrated in figure (5.8) where the $\delta\langle r^2\rangle_Z^{52,50}$,

$\delta\langle r^2\rangle_Z^{58,50}$, $\delta\langle r^2\rangle_Z^{60,50}$ of krypton [67], rubidium [3], strontium [4] and zirconium [7] are plotted against their respective atomic number.

Equation (5.6) now becomes

$$\mu \cdot \delta\nu_i^{AA'} = \mu_{ref} M_i + \mu F_i \cdot K(Z')\delta\langle r^2\rangle_{Z'}^{AA'} \tag{5.8}$$

Figure (5.9) shows the different calibration graphs for the elements krypton, rubidium, strontium and zirconium where the modified niobium isotope shifts $\mu\delta\nu^{A,A'}$ are plotted versus the modified charge radii $\mu\delta\langle r^2\rangle^{A,A'}$ of the respective element. The best fit corresponds to a minimum in the χ^2-surface where

$$\chi^2 = \sum_{AA'} \frac{[\mu\delta\nu_i^{AA'} - (\mu_{ref} M_i + \mu F_i \cdot K(Z')\delta\langle r^2\rangle_{Z'}^{AA'})]^2}{\sigma^2_{\mu\delta\nu_i^{AA'}} + (F_i K(Z'))^2 \sigma^2_{\mu\delta\langle r^2\rangle_{Z'}^{AA'}}} \tag{5.9}$$

and σ_i are the errors of the experimental isotope shifts and radii. The χ^2-surface for niobium isotope shifts versus krypton charge radii is shown in figure (5.10). The diagonal form of the elliptical minimum demonstrates the correlation between the gradient $F_i K(Z')$ and the intercept M_i of the fitted straight line. The χ^2-surfaces for rubidium, strontium and zirconium show similar anti-correlated behaviour and the magnitude of the correlation, the covariance, was obtained for each fit. The field and mass factors were obtained according to equation (5.8) and are displayed in table (5.1).

The $F_i \cdot K(Z')$ for different neighbouring chains can be plotted versus Z'. An interpolation to $Z' = Z = 41$ reveals the field factor of niobium. As the extraction of $\delta\langle r^2\rangle^{A,A'}$ is very sensitive to the calibration, it was advisable to be very careful in the evaluation of the field and the mass factor and the underlying assumptions. The interpolations for the field factor F_i and for the mass factor M_i were performed as two least-square fits under the assumption that both factors are constant with Z. Both fits are displayed in figure (5.11).

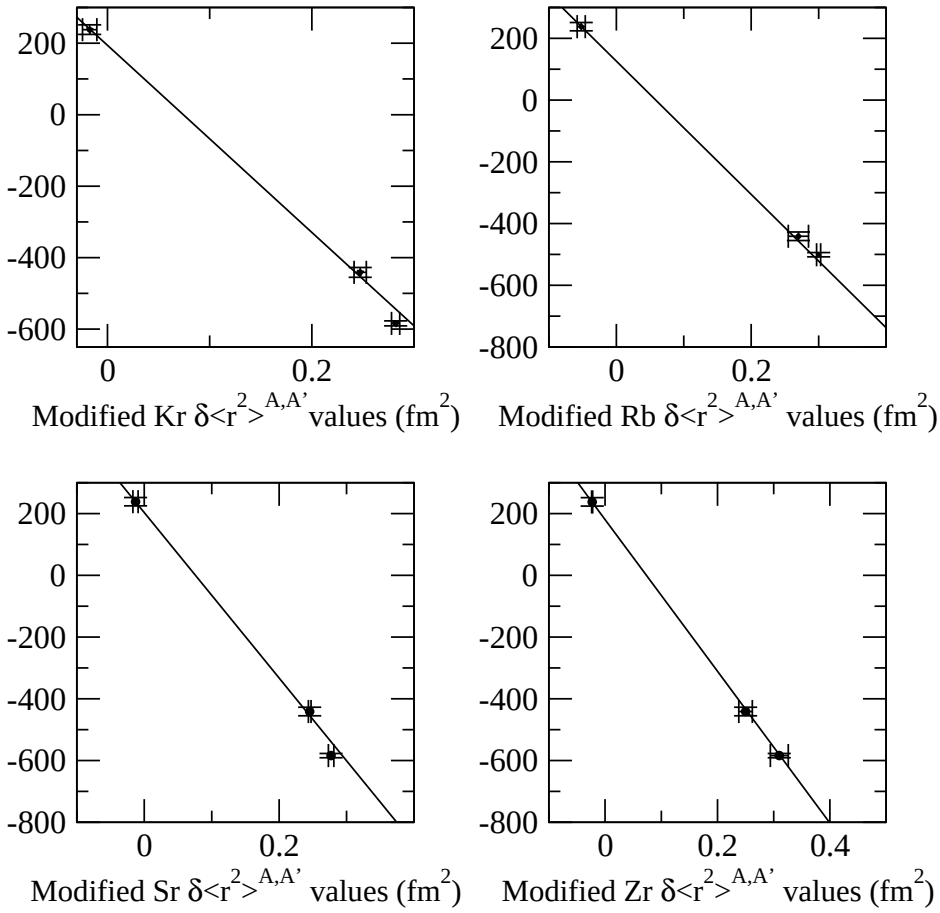

Figure 5.9: The modified isotope shifts of niobium, $\mu\delta\nu^{A,A'}$, are plotted against modified charge radii, $\mu\delta\langle r^2\rangle^{A,A'}$, of neighbouring elements.

Table 5.1: The extracted field factor and mass factor for neighbouring elements Kr, Rb, Sr and Zr using niobium isotope shifts

Element	Z'	$F_iK(Z')$ (MHz/fm^2)	M_i (GHz)
Krypton	36	-2617(107)	822(96)
Rubidium	37	-2160(103)	534(70)
Strontium	38	-2680(77)	860(68)
Zirconium	40	-2458(69)	765(53)

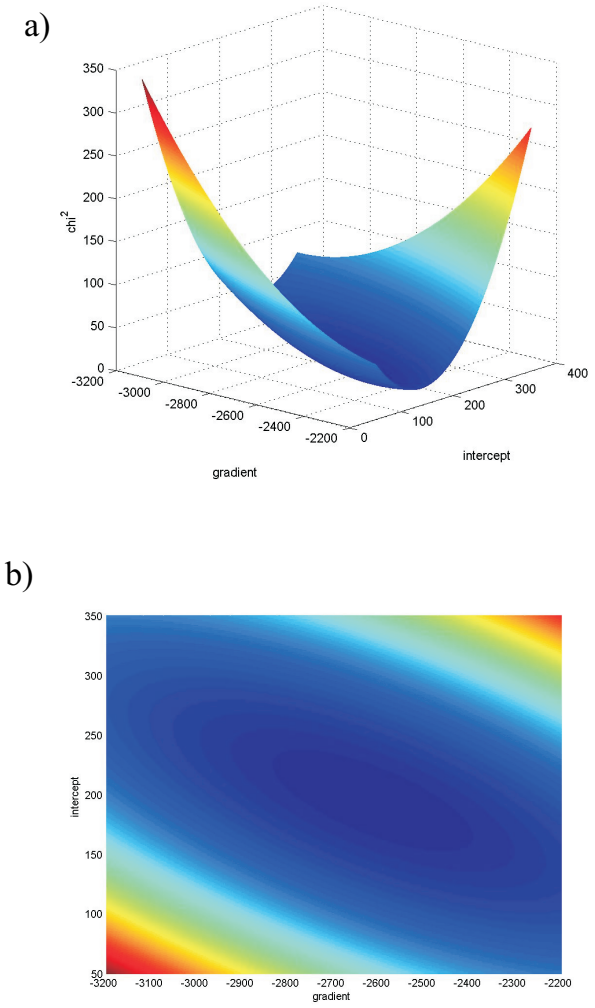

Figure 5.10: The χ^2 surface of the krypton versus niobium least squares fit. a) in three dimensions b) in the gradient-intercept-plane only. The gradient and the intercept are anticorrelated. The χ^2 -surfaces for rubidium, strontium and zirconium look similar.

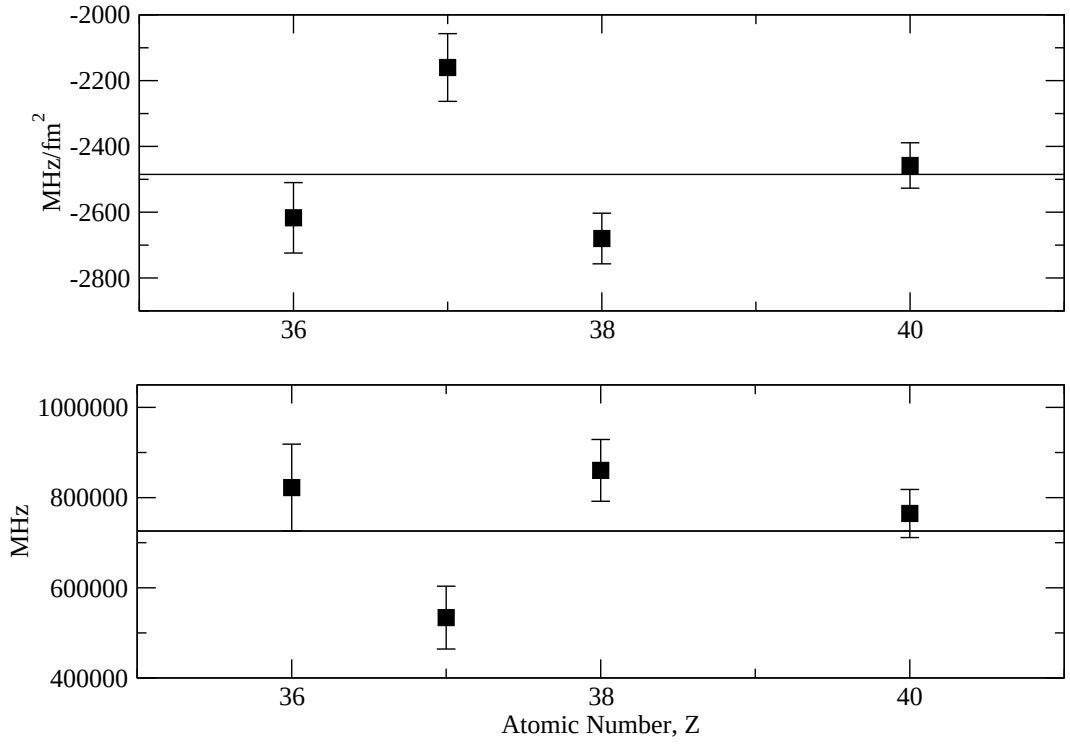

Figure 5.11: Top: The field factors of krypton, rubidium, strontium and zirconium are plotted against their respective Z. The field factor for niobium is obtained through interpolation. Bottom: Interpolation for the mass factor.

This assumption of a zero gradient was justified by the statistical analysis of zirconium and strontium data. In both cases accepted values of the field factor and mass factor are available from calibration against stable isotopes [4, 50]. For each of the two elements a calibration versus neighbouring elements has been carried out. As the interpolation of field factors from neighbouring chains could have either a zero or non-zero gradient, hypothesis testing was applied to decide which fit was statistically more significant.

Hypothesis testing: The F - test

An $F-test$ allows one to decide which of two models is best employed to fit a set of data. The $F-test$ is originally used to compare two sample variances s_1 and s_2 of the same population. As these sample variances should lie close to each other, we expect the ratio

$$F = \frac{s_1}{s_2} \tag{5.10}$$

to be close to 1. A very large or a very small value of F would indicate a significant difference between the variances.

The $F-test$ can also be used to compare the χ^2s of two different regression lines that fit the same data. It is always possible to fit a set of data with a model (model 2) that has more parameters than a simpler approach (model 1). However, although model 2 with more parameters $p2$ usually presents a lower error to the fit, this does not mean that it is significantly better than the simpler model 1 with $p1$ parameters, $p1 < p2$. The null hypothesis in this case is: Model 2 "y = mx + b" does not provide a significantly better fit to the data than model 1 "y = C". The ratio F is modified to [68]

$$F = \frac{\frac{\chi_2^2 - \chi_1^2}{p2-p1}}{\frac{\chi_2^2}{n-p2}} \tag{5.11}$$

where χ_i^2 are the χ^2s of the least square fits 1 and 2, p_i are the number of parameters

of the models 1 and 2; and n is the number of data points.

The significance level is chosen to be $\alpha = 5\%$ which rejects F values that are larger than a critical $F = F_c$. A particular $F = F(k, l)$ is dependent on the degrees of freedom of the numerator k and of the denominator l. For example $F_c(1, 1) = 161$ at 5% [69] for $p_2 - p_1 = 1$ and $n - p_2 = 1$.

The investigation for both strontium and zirconium yields that a significant linear dependency of the field factor on Z cannot be demonstrated. For the strontium isotope shifts around the shell closure $F(1, 1) = 0.9479$ which corresponds to a significance of 50.90%. Hence, the null hypothesis is not rejected and a non-zero gradient does not provide a significantly better fit to the data than a zero gradient interpolation. The same conclusion is drawn for the zirconium isotope shifts around the shell closure as $F(1, 1) = 0.028917$ which corresponds to a significance of 89.3%.

Further, the field factors from calibration against neighbouring elements were compared to the accepted values given by Buchinger [4] and Thayer [50]. The fits with non-zero gradient differed by 9% - 28% from the accepted field factor value, the fits with zero gradients differed by 1% - 18% from the accepted F_i-value. This is seen as a further indication that an interpolation with a zero gradient is the better choice.

The deviation of the field factors obtained through calibration against neighbouring elements from the accepted value is of the same order of magnitude as results by Fricke [30]. Fricke used a combined analysis of muonic, electron scattering and x-ray data in order to calibrate field factors independently of the electronic configuration of the transition involved. He states errors of up to 20% on his field factors. Another way of estimating an unknown field factor is by estimating the probability density of the electron in the nucleus. This method was used by Keim [67] and he assigned a systematic error of 10% in order to account for the uncertainty of the underlying assumptions.

Table 5.2: The extracted field and mass factor for the niobum isotopes based on the calibration versus neighbouring elements

A	$\delta\nu^{A,91}$ MHz	$\delta\langle r^2\rangle^{A,91}$ (fm^2)	$\sqrt{\langle\beta_2^2\rangle}$
90	-123(7) [a]	0.0138(33)	0.0193(3)
90m	-191(9) [a]	0.0412(42)	0.203(3)
91	0	0	0.150(3)
91m	-92(7) [a]	0.037(3)	0.168(4)
92	-223(7) [a]	0.1247(32)	0.171(4)
93	-584(7) [a]	0.3041(46)	0.211(3)
99	-1883(9)	1.013(14)	0.281(5)
101	-3410(8)	1.691(21)	0.393(5)
103	-3779(8)	1.895(23)	0.401(5)

[a] Baczynska [11]

As a result of this investigation, the field factor F_{290nm} and the mass factor M_{290nm} for the 290.82 nm transition in niobium, $Z = 41$, are obtained by forming the weighted mean of the field factors obtained from neighbouring isotopes, hence assuming a zero gradient. A full treatment of the correlation of the statistical errors has been carried out and the reader is referred to the Appendix for details. A systematic error of 10% was assigned to the calibration to account for the uncertainty in the evaluation.

The field factor is $F_{290nm} = -2485(41)$ MHz/fm^2, the mass factor yields $M_{290nm} = 726(33)$ GHz. These values replace the field factor of $F = -2646(8)$ MHz/fm^2 and mass factor $M = 762(7)$ GHz obtained by K Baczynska [11] for the same transition. The big difference compared to the old set of values arises from a mistake in a computer code used by Baczynska which led to too small an error in the data set. This mistake has since been corrected.

Using the new F_{290nm} and M_{290nm}-values, differential nuclear charge radii for the niobium chain were extracted and the correlation between the field and the mass factor was taken into account in the evaluation of the statistical error on $\delta\langle r^2\rangle^{A,91}$. Values of the absolute charge radii $\langle r^2\rangle^A$ were determined using the ex-

tracted $\delta\langle r^2\rangle^{A,91}$ and the absolute value of $\langle r^2\rangle^{93}$ from Angeli [70]. The $\langle r^2\rangle^A$ were then used in a *maple*-routine by M L Bissell to extract the deformation parameter $\sqrt{\langle\beta_2^2\rangle}$ according to equation (2.39). The obtained values for $\delta\langle r^2\rangle^{A,91}$ and $\sqrt{\langle\beta_2^2\rangle}$ are displayed in table (5.2).

5.5 Nuclear Moments - Results

The hyperfine structure constants of the fitted hyperfine spectra are displayed in table (5.3). It was possible to confirm the preliminary spin assignments of $I^{\pi} = 5/2^{+}$

Table 5.3: The hyperfine structure constants for the transition 5s $^5F_1$ (2356.760 cm^{-1}) $\rightarrow$ 5p $^5F_1^o$ 36731.790 cm^{-1} at 290.8237 nm for the isotopes ^{93}Nb, ^{99}Nb, ^{101}Nb and ^{103}Nb. Due to the constant ratios A_u/A_l and B_u/B_l, no errors are assigned to either A_l or B_l.

A	A_u (MHz)	B_u (MHz)	A_l (MHz)	B_l (MHz)
93	1198.0(1)	53.0(9)	-1151.4	23.4
99	1166(2)	53 (11)	-1121.8	23.3
101	1115.0(5)	-175.8(2.3)	-1071.6	-77.7
103	1094(5.5)	-181.8(3)	1051.6	-80.3

for the ^{101}Nb and ^{103}Nb isotopes. The magnetic dipole moments μ and the spectroscopic electric quadrupole moments Q_s are extracted from the hyperfine structure constants A_l, B_l, A_u and B_u using equations (2.13) and (2.21). The magnetic moment was extracted under the assumption that the hyperfine anomaly is negligible and the ratios $A_u/A_l = -1.0405(2)$ and $B_u/B_l = 2.26(12)$ were fixed from ^{93}Nb. This reduced the number of free parameters to the centroid, one of the A and one of the B coefficients. The assigned error on the magnetic moment is increased to 1% to account for possible unknown hyperfine anomaly effects. In fact, as the nuclei in neighbouring isotones have been found to undergo a significant shape change at $N = 60$, it is not unreasonable to expect that the shape change is connected to a re-distribution of nuclear magnetisation. However, the determination of a hyperfine anomaly requires an independent measurement of the magnetic moment which is not possible using laser spectroscopy.

The deformation parameter β_2 is extracted from the intrinsic quadrupole moment Q_0 using the finite range droplet model. Detailed information can be found in the

Table 5.4: The nuclear dipole and quadrupole moments, μ and Q_S, as well as the deformation parameters β_2 of the isotopes ^{93}Nb, ^{99}Nb, ^{101}Nb and ^{103}Nb.

Mass Number A	Spin I	μ μ_N	Q_S (barn)	$\langle\beta_2\rangle$
93	9/2	6.1705(3) [a]	-0.32(2)[a]	-0.07(1)
99	9/2	6.01(6)	-0.32(7)	-0.072(16)
101	5/2	3.19(3)	1.06(8)	0.317(25)
103	5/2	3.13(3)	1.10(7)	0.324(22)

[a]Table of Nuclides [60]

papers by W D Myer and K H Schmidt [71], W H Myers and W J Swiatecki [72] and D Berdichevsky and F Tondeur [73]. A *maple*-routine written by M L Bissell of the University of Birmingham, was used to perform droplet model calculations.

The extracted deformation parameter β_2, together with the magnetic dipole moments μ and the spectroscopic quadrupole moments Q_s are displayed in table (5.4).

5.6 Analysis and Results of ^{102}Nb and ^{102m}Nb

The ^{102}Nb nucleus proved to be a particularly difficult case. It is directly produced as a fission fragment of ^{nat}U and also occurs through β-decay from ^{102}Zr. Ahrens (1976) [74] states two half-lifes of 1.3 s and 4.3 s from ^{102}Zr decay studies. One of them is a low lying isomeric state close to the ground state. The 1.3 s half-life has been assigned $I = 1^+$ [60]. The excitation energy between the two states has been stated as $E_{exc} = 130(50)$ keV by the NUBASE evaluation of nuclear decay properties (2003) [75]. Latest information from precision mass measurements by Rinta-Antila *et al* (2007) [59] report a tentative energy difference of $E_{exc} = 93(23)$ keV for the low lying isomeric state. The measurements also indicate the 4.3 s state to be the ground state. No transitions are reported between these two states. The information available is summarised in table (5.5).

Table 5.5: Spin and half-lives of ^{102}Nb long lived states [60]

Level MeV	Half-life $t_{1/2}$	Spin I^π
0.000 [59]	4.3s	unassigned [74], (4)[60]
0.130(50) [75] 0.093(23) [59]	1.3s	1^+

Due to the relatively long half-life of the isomer both the ground state and the metastable state were produced in the experiment and it was feasible to do spectroscopy on both of them. However, at the time of the experiment, it was not possible to determine in which ratio the two states were produced. During the experiment a total of four hyperfine structure peaks could be observed. The spin $I^\pi = 1^+$ of the isomer together with the atomic angular momentum lead to the expectation of 6 hyperfine peaks in the spectrum. For an estimate of the magnetic moment, the measured magnetic moments of ^{103}Nb ($I = 5/2^+$) and ^{101}Zr ($I = 3/2^+$) (single proton and single neutron states respectively) were coupled according to

equation (2.10). For the deformation, a similar deformation to that of ^{101}Y (Q_s = 1.53(17) b [56]) was assumed. The spin of the ground state has not been officially assigned yet. The β-decay to ^{102}Mo populates levels with spin $I = (3^+), (4^+), 6^+$ with a branching ratio of 71% to the (3^+) state at 2.4803 MeV [60] (figure (5.12)). Assuming allowed or first-forbidden decay, the spin of the parent nucleus could be $I = 3, 4$ or 5. Decay to $I = 2$ is not observed which excludes a spin of $I = 2$ in the parent nucleus. Other levels in molybdenum have not been assigned. A summation of the assigned transition percentages suggests that the whole decay strength has been accounted for in the scheme. A spin of $I = 4$ is suggested in the level diagram [60] which is displayed in figure (5.12). Assuming spin $I = 3, 4$ or 5, the number

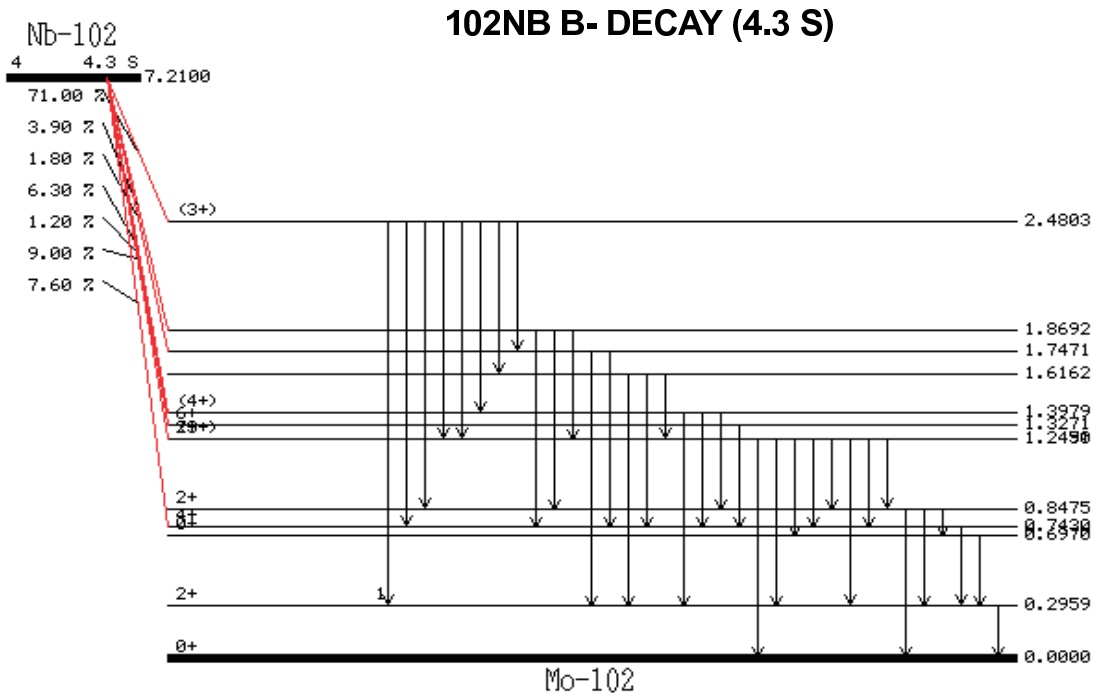

Parent state: G.S. Half life: 4.3 S(4) Q(gs): 7210(70) keV Branch ratio: 1.0

Figure 5.12: β-decay of the ^{102}Nb ($t_{1/2}$ = 4.3s) isomer [60].

Table 5.6: Prediction of the magnetic moments of 102Nb and 102mNb, based on experimental values of ^{101}Nb, ^{101}Zr and ^{105}Mo

Isotope A	Spin I^π	μ μ_N	Configuration
^{101}Nb	$5/2^+$	3.19(3)	$\pi[422]5/2$
^{101}Zr	$3/2^+$	-0.272(1) [a]	$\nu[411]3/2$
^{105}Mo	$(5/2)^-$	-0.55(2) [b]	$\nu[532]5/2$
^{102m}Nb	1^+	2.370	$\pi[422]5/2 \otimes \nu[411]3/2$
^{102}Nb	3^+	2.554	$\pi[422]5/2 \otimes \nu[411]3/2$
^{102}Nb	4^+	2.918	$\pi[422]5/2 \otimes \nu[411]3/2$
^{102}Nb	5^-	2.641	$\pi[422]5/2 \otimes \nu[532]5/2$

[a] ref. [7] [b] ref [10]

of hyperfine components of the ground state is 7. For spin $I = 3$ or 4 a magnetic moment can be predicted from coupling the same single particle values as for the isomeric state. This assumes an isomer with the same Nilsson states as the ground state (table (5.6)) and therefore the same degree of deformation is assumed as before (^{101}Y, $Q_s = 1.53(17)$ b [56]). The single particle states $\Omega_\pi = [422](5/2)$ and $\Omega_\nu = [411](3/2)$ cannot couple to $I^\pi = 5$. Here it is assumed that the neutron scatters into the $\Omega_\nu = [532](5/2)$ state, which is suggested to lie close to the $\Omega_\nu = [411](3/2)$ state in the Nilsson model for the same degree of nuclear deformation (see [65]). The value for the magnetic moment of that state is taken from ^{105}Mo ($I^\pi = (5/2)^-$) [10] . A summary of the predicted moments is given in table (5.6).

To disentangle the ground state structure from the isomer structure a clear spectrum with well defined peaks needs to be recorded. Unfortunately the available spectrum lacks clarity. Figure (5.13) shows the recorded spectrum (top) together with the predictions (bottom). The frequency scale of the recorded spectrum stems from the experimental measurements and has been maintained for the display of the predictions. For a first tentative disentanglement, the centroid of the ground state spectrum was obtained from a direct interpolation of the ^{101}Nb and ^{103}Nb charge radii (see table (5.2)). Figure (5.13) shows that the outer peaks can be suggested

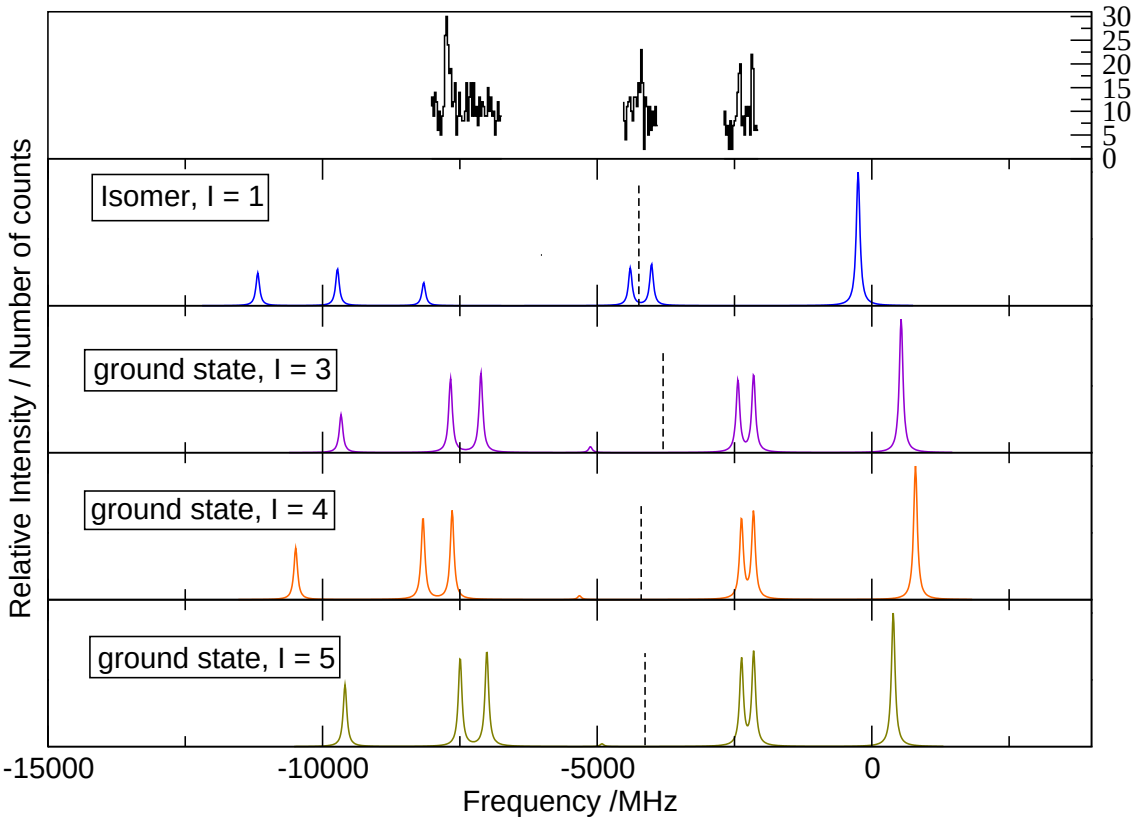

Figure 5.13: Top: Recorded ^{102}Nb hyperfine structure components: The spectrum shows a mixture of ground state and isomer components. Due to time constrains these were the only regions covered. Bottom4: The predicted hyperfine structure for ground and isomer states. The dotted lines mark the centroid of each spectrum.

to represent the ground state structure. For display purposes, the ground state predictions were shifted to overlap with the two right peaks. It can be seen that the prediction for $I = 4$ also matches up the left peak as part of the left doublet structure while the predictions for $I = 3$ and 5, though very close, do not match up. It was then assumed that the peak in the middle spectrum belongs to the isomer. It is suggested that the peak represents the doublet structure, as any other assignment of the peak would shift the centroid of the transition (dotted line) over frequency distances that correspond to unphysically large isomer shifts.

Figure (5.14) shows again the recorded spectrum, where the recorded peak heights have been normalised to the number of scans in each spectrum, showing

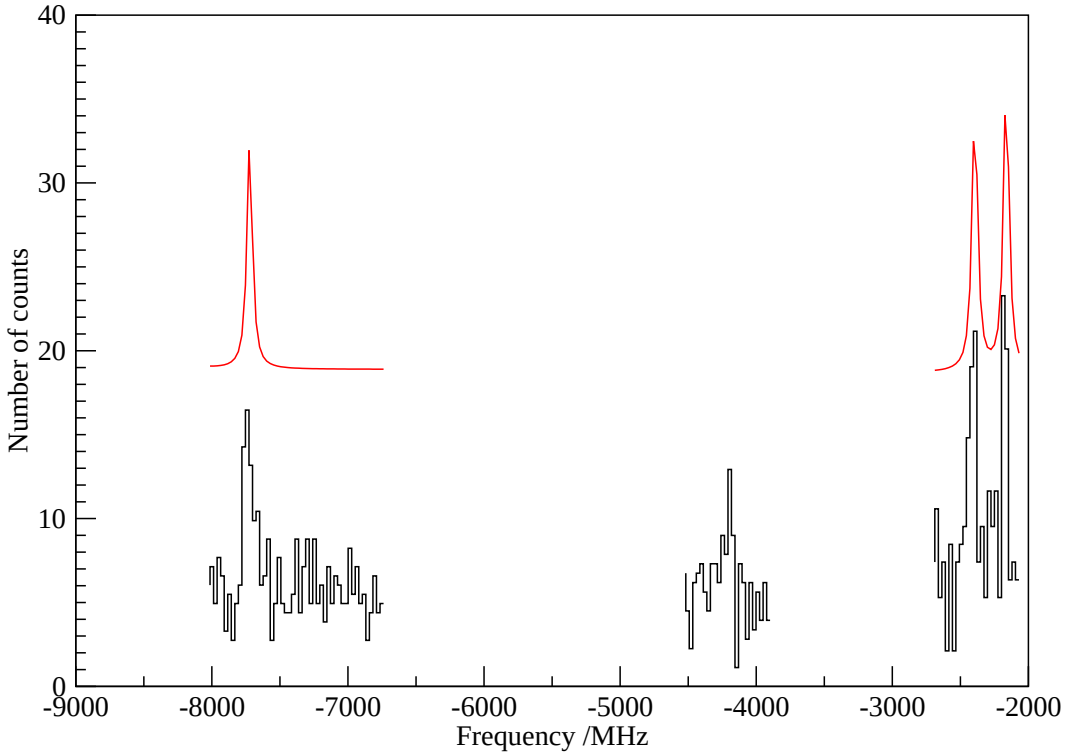

Figure 5.14: Recorded ^{102}Nb spectrum, peak height is normalised to the number of scans taken in each region. Above that is a fit for the I = 4 ground state structure.

that the structure on the right has the most intense peaks.

Table 5.7: The hyperfine constants for the hyperfine structure fits for the different spin assignemts of ^{102}Nb including the reduced χ^2 for each fit.

Isotope	Spin I	A_u (MHz)	B_u (MHz)	A_l (MHz)	B_l (MHz)	χ^2/dof
102	3	832.2(1.8)	-250.4(7.1)	-799.8	-110.7	1.177
102	4	645.9(1.4)	-263.7(5.2)	-620.8	-116.6	0.693
102	5	520.0(1.1)	-273.3(7.9)	-507.5	-120.8	1.177

The spectra were fitted for each suggested spin using the χ^2 minimisation routine of *xmgrace*. The ratios $A_u/A_l = -1.0405(2)$ and $B_u/B_l = 2.26(12)$ were fixed from ^{93}Nb reducing the free fitting parameters to the centroid and one of the A and one

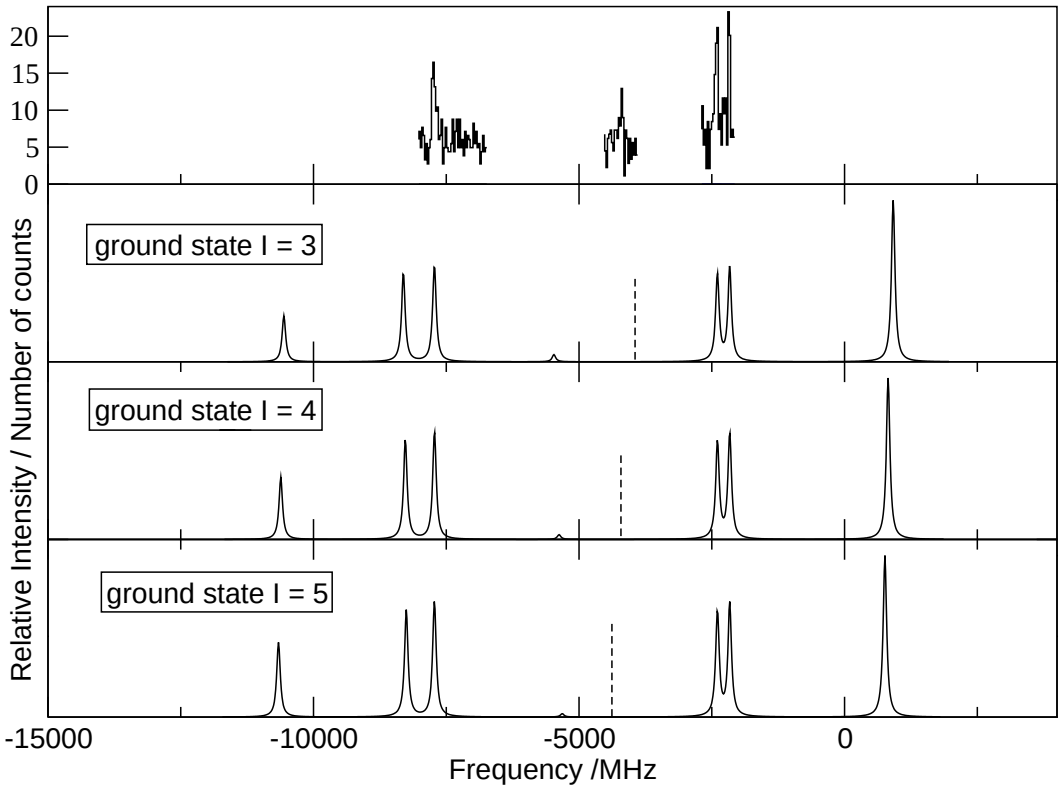

Figure 5.15: Top: recorded ^{102}Nb spectrum. Bottom spectra: fitted ground state structure with spin assignments I = 3, 4 and 5.

of the B coefficients. The fit for $I = 4$ is shown in figure (5.14). The retrieved A and B - hyperfine structure constants were used as a basis to display the full spectrum for each of the spin assignments. As figure (5.15) shows, all of the spin assignments give possible fits. The hyperfine parameters with statistical errors and the reduced χ^2 for each of the fits can be found in table (5.7) showing that the reduced χ^2 is smallest for $I = 4$ which indicates the best fit. However, all three χ^2s are close to 1 which indicates that all the possibilities give agreeable fits. Table (5.8) shows the values for the magnetic moment, the quadrupole moment and the deformation parameter β_2 that were extracted from the hyperfine structure parameters. The centroid of each fit was used to calculate the isotope shift between ^{102}Nb and ^{91}Nb. The isotope shifts were used to extract the change in mean square charge radius

Table 5.8: The nuclear dipole and quadrupole moments μ, Q_S and Q_0, the deformation parameter $\langle\beta_2\rangle$, $\delta\langle r^2\rangle^{102m,91}$ and $\sqrt{\langle\beta_2^2\rangle}$ for the different spin assignments for ^{102m}Nb.

Spin I	μ μ_N	Q_S (barn)	Q_0 (barn)	$\langle\beta_2\rangle$	$\delta\langle r^2\rangle^{102,91}$ (fm^2)	$\sqrt{\langle\beta_2^2\rangle}$
3	2.858(7)	1.51(11)	3.63(26)	0.38(2)	1.67(2)	0.374(4)
4	2.957(7)	1.59(11)	3.13(21)	0.33(2)	1.78(2)	0.394(4)
5	3.022(7)	1.65(12)	2.86(20)	0.30(2)	1.85(2)	0.407(4)

using the F_{290nm} and M_{290nm} values that were deduced in section 5.4. The values of $\delta\langle r^2\rangle^{102,91}$ can be found in table (5.8) and were further used to deduce the values for the deformation parameter $\sqrt{\langle\beta_2^2\rangle}$.

Using the found assignments, a rough estimate of the production ratio of the nuclear states can be made. The total intensity of any transition is spread out over the hyperfine structure. The intensity of each hyperfine component depends on the angular momentum of both the electronic wavefunction and the nucleus. The calculation was first done by Racah and were tabulated by White and Eliason [64]. Using these intensities and the observed intensities in the recorded spectrum, a ratio of ^{102m}Nb : ^{102}Nb = 1 : 2.6 or 1 : 5.2 can be calculated. The estimate depends on the isomer structure: if it is assumed that the peak in the recorded spectrum stems from a collapsed doublet, the ratio is a factor two less favourable than under the assumption that the doublet is not collapsed but that one of the peaks is not visible.

5.7 Interpretation

5.7.1 The charge radii

The extracted changes in the mean square charge radii are displayed in table (5.9) together with the deformation parameters $\sqrt{\langle\beta_2^2\rangle}$ and $\langle\beta_2\rangle$ that were extracted from $\delta\langle r^2\rangle^{A,91}$ and from the quadrupole moment Q_0 respectively. The deformation parameter $\langle\beta_2\rangle$ from the quadrupole moment does not contain information about dynamic contributions to the deformation whereas $\sqrt{\langle\beta_2^2\rangle}$ contains both static and dynamic contributions. Figure (5.16) shows the charge radii systematics between neutron number $N = 49$ and $N = 62$. For these neutron numbers, the radii were re-calculated using equation (2.38) with only the static and not the dynamic deformation contribution at constant volume; they are displayed by the unfilled circles in figure (5.16). Figure (5.16) also shows droplet model isodeformation lines for the deformation parameter.

Table 5.9: The extracted $\delta\langle r^2\rangle^{A,91}$ for the niobium chain with $\sqrt{\langle\beta_2^2\rangle}$ and the quadrupole moment Qs with $\langle\beta_2\rangle$.

A	Spin I^π	$\delta\langle r^2\rangle^{A,91}$ (fm^2)	$\sqrt{\langle\beta_2^2\rangle}$	Q$_S$ (barn)	$\langle\beta_2\rangle$
90	8^+	+0.0138(33)	0.193(3)	-0.01(4)[a]	-0.001(6)
90m	4^-	+0.0412(42)	0.203(3)	-0.2(1)[a]	-0.05(2)
91	$9/2^+$	0	0.150(3)	-0.25(3)[a]	-0.058(8)
91m	$1/2^-$	+0.037(3)	0.168(4)	-	-
92	7^+	+0.1247(32)	0.171(4)	-0.31(5)[a]	-0.058(10)
93	$9/2^+$	+0.3041(46)	0.211(3)	-0.32(2) [b]	-0.07(1)
99	$9/2^+$	+1.013(14)	0.281(5)	-0.32(7)	-0.072(16)
101	$5/2^+$	+1.691(21)	0.393(5)	+1.06(8)	0.317(25)
102	(3)	+1.67(2)	0.374(4)	+1.51(11)	0.38(2)
102	(4)	+1.78(2)	0.394(4)	+1.59(11)	0.33(2)
102	(5)	+1.85(3)	0.407(4)	+1.65(12)	0.30(2)
103	$5/2^+$	+1.895(23)	0.401(5)	+1.10(7)	0.324(22)

[a] ref. [11] [b] ref. [60]

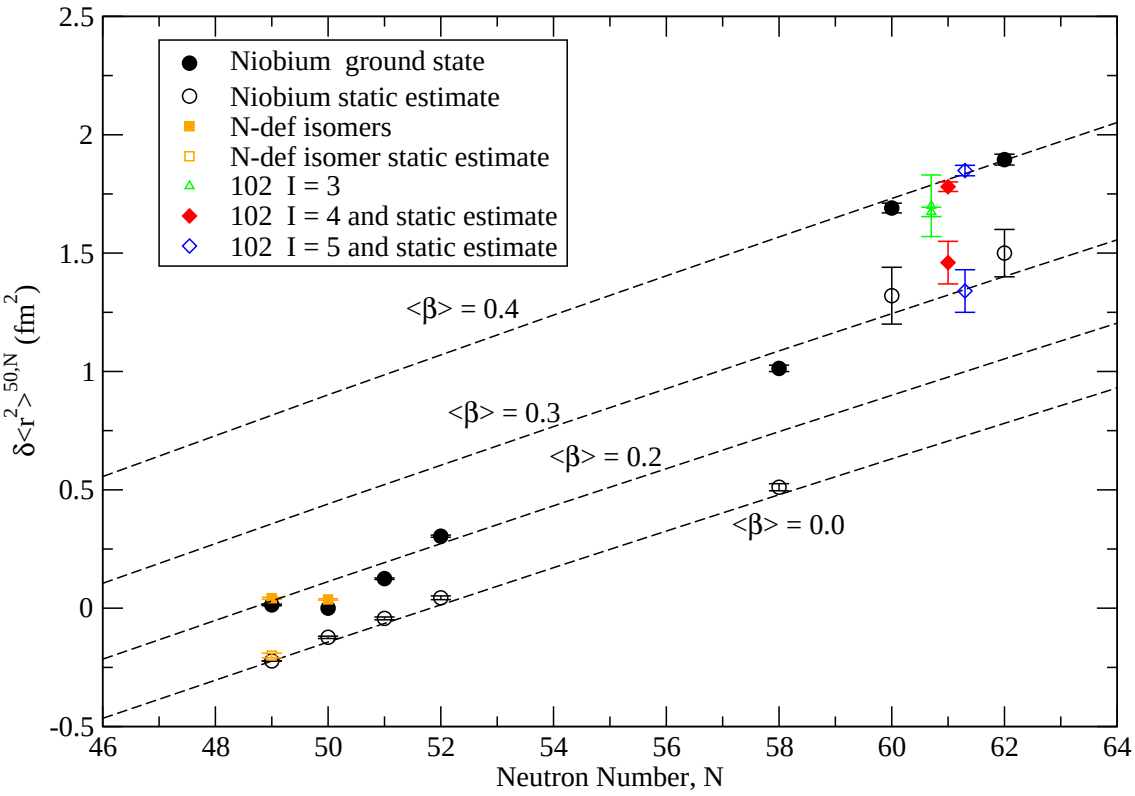

Figure 5.16: The extracted differential niobium charge radii are plotted against their neutron number. The dotted lines are isodeformation lines, the unfilled circles show the charge radii without the dynamic deformation contribution. The charge radii of ^{102}Nb are spread around $N = 61$ for clarity of the diagram.

The addition of neutrons to a nucleus causes an increase in nuclear volume, so that the charge radius increases even if the deformation of the nucleus does not change. Therefore, isodeformations lines have got a positive slope. The nuclear radii of niobium indicate very little deformation around the shell closure at $N = 50$. The radii based on the static deformation alone cannot account for the measured $\delta\langle r^2\rangle$ measured, (figure (5.16), which indicates that the changes measured are due to the dynamic deformation. For neutron numbers $N = 52 - 57$ a smooth onset in deformation seems likely, up to a measured deformation of $\sqrt{\langle\beta_2^2\rangle} = 0.272(5)$ in $N = 58$. This smooth behaviour has been observed in neighbouring isotope chains $Z = 40$ [7] and $Z = 39$ [56]. The static deformation in ^{99}Nb ($N = 58$) reveals

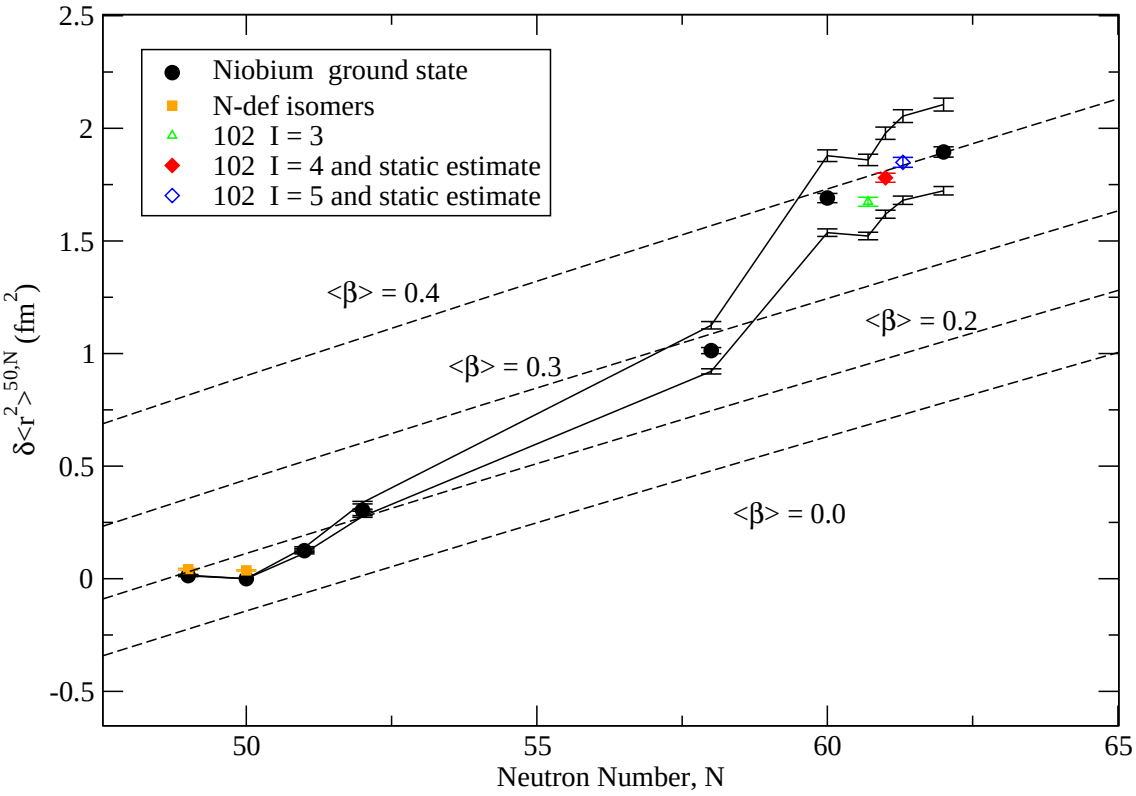

Figure 5.17: The extracted differential niobium charge radii are plotted against their neutron number. The enclosing lines show the effect of the 10% systematic error on the calibration that is fed through to the charge radii. The charge radii of ^{102}Nb are spread around $N = 61$ for clarity of the diagram.

that the nucleus maintains its spherical equilibrium shape, but appears very soft to dynamic deformation.

At $N = 60$ an increase in $\langle r^2 \rangle$ takes place that has been established in the neighbouring isotope chains. The sudden increase in the ground state $\langle r^2 \rangle$-value is due to an increased deformation in ^{101}Nb. The sign of $\langle \beta_2 \rangle$ in table 5.9 shows that the nuclear shape changes from a slightly oblate shape in ^{99}Nb to a strongly prolate deformed nucleus in ^{101}Nb and ^{103}Nb. Again, this is in agreement with observations in the yttrium chain (figure (5.18)). The large difference between $\sqrt{\langle \beta_2^2 \rangle}$ and $\langle \beta_2 \rangle$ in ^{101}Nb indicate a soft nucleus, softer than observed in ^{99}Y and ^{101}Y. However, ^{101}Nb and ^{103}Nb are less soft than ^{99}Nb. Here, it would be advantageous to have ^{100}Nb

values to establish how the softness changes across the onset in deformation.

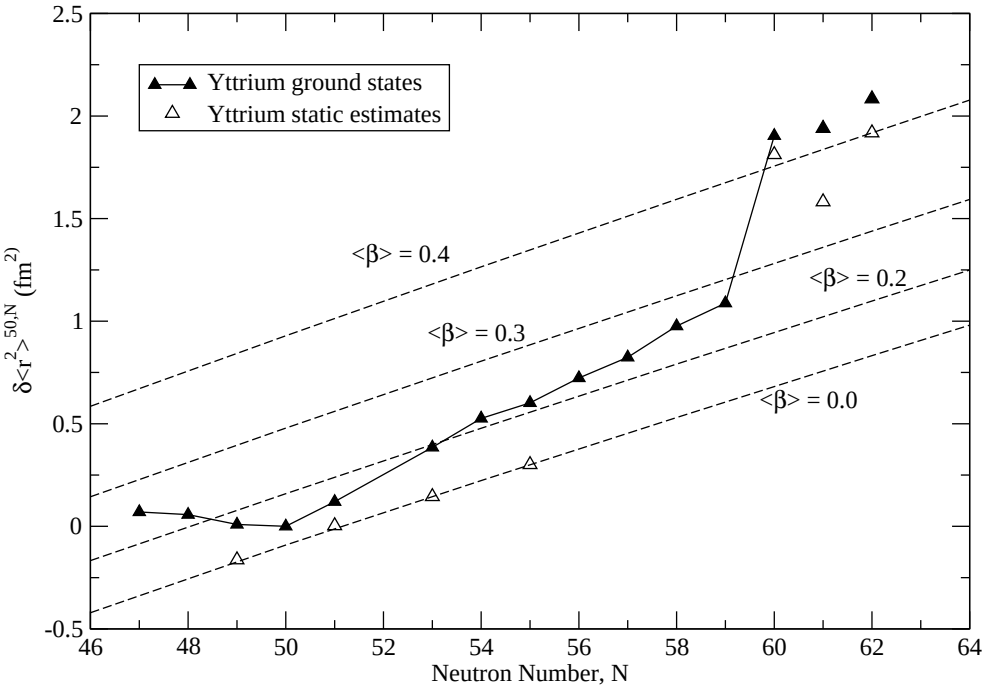

Figure 5.18: The differential yttrium charge radii are plotted against their neutron number. The data are taken from Gardner [56]. The charge radii were not assigned statistical errors and the uncertainty in the calibration of the atomic factors is taken into account by assignment of a 10% error onto the charge radii. The unfilled circles show the charge radii without the dynamic deformation contribution. The dotted lines are isodeformation lines. $N = 61$ is not connected by a line as it was not clear whether the ground state or an isomer has been observed.

Figure (5.17) shows how the application of the systematic error onto the F_{290nm}-value changes the extracted values for the charge radii. For a 10% increase in the calibration, the charge radii are well above the $\beta = 0.4$ iso-deformation line. The extracted values for ^{102}Nb are spread out by spin in figure (5.16). From calculations for $I = 3$ the nucleus appears to be completely rigid and turns out to be increasingly soft in calculations for the cases $I = 4$ and $I = 5$. This is very different from the more soft nature of ^{101}Nb and ^{103}Nb. The corresponding $N = 61$ nucleus in yttrium shows a very soft nature whereas the $N = 60$ and $N = 62$ nuclei are more rigid (figure (5.18)). However it is not established whether the measurement of ^{100}Y belongs

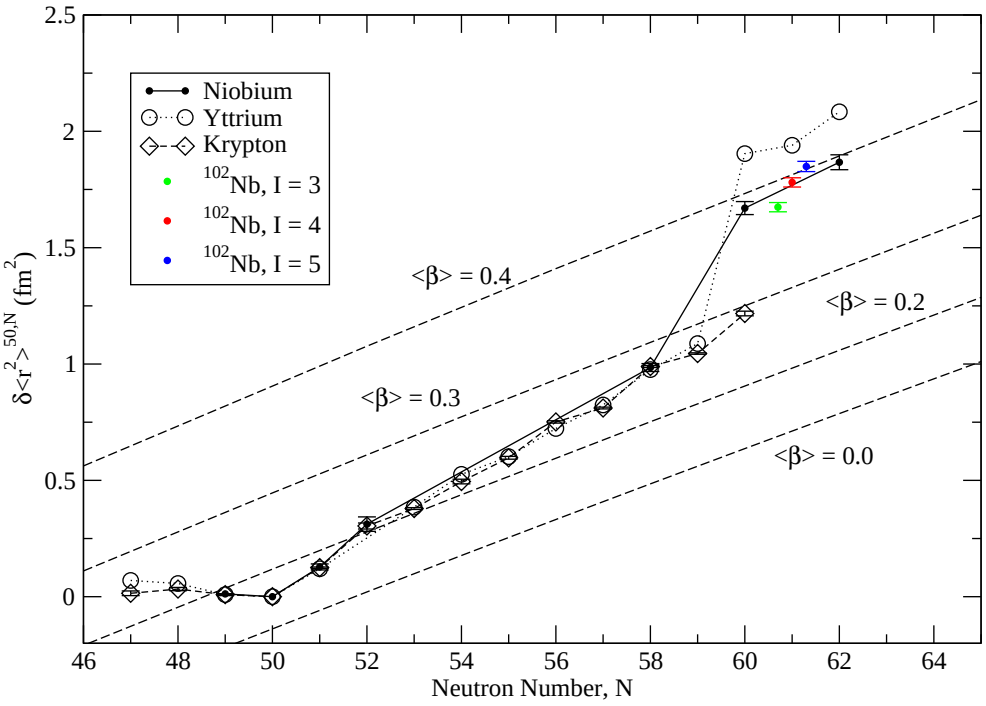

Figure 5.19: The charge radii systematic for krypton [67], yttrium [56] and niobium. Three data points are show for ^{102}Nb, originating from the different possible spin assigments $I = 3, 4$ or 5. The neutron deficient niobium data were taken from [11]. The dotted lines are isodeformation lines.

to the yttrium isomer or the ground state, i.e. whether a trend of similar soft or rigidness can be expected after the shape change or not. Again, where available, the yttrium charge radii in figure (5.18) were re-calculated on the basis of the static deformation parameter alone.

In zirconium, a rigid behaviour has been observed for $N = 61$ (^{101}Zr) ($\langle\beta_2\rangle = +0.435(35)$) [7]. However due to the even number of protons in the zirconium chain, no static information is available on ^{100}Zr nor ^{102}Zr and it was concluded that the rigid nature of ^{101}Zr represents the trend for the nuclei after $N = 60$. The soft nature of the ^{102}Nb $I = 4$ and $I = 5$ nuclei would fit well with the observed softness in ^{101}Nb and ^{103}Nb and a trend from more rigid nuclei in yttrium at $N > 60$ to softer nuclei in niobium would fit in with the observed gradual smoothing of the onset of

deformation in molybdenum [10]. The rigid nature of ^{99}Y, ^{101}Y and ^{101}Zr ($N \geq 60$) would suggest a fairly deep energetic potential which stabilises the deformation. This potential seems to flatten in niobium, indicated by the increasing softness of the isotopes past $N = 60$. This idea of a trend seems to be contradicted by the findings in ^{100}Y and ^{102}Nb as ^{100}Y appears to be a very soft nucleus and not as rigid as its neighbours ^{99}Y and ^{101}Y. Similarly in niobium: A spin of $I = 3$ in ^{102}Nb would lead to a very rigid nucleus in a steep potential well which is a quite different behaviour to its relatively soft neighbours ^{101}Nb and ^{103}Nb.

Figure (5.19) shows the charge radii systematics for krypton, yttrium and niobium. It demonstrates that the onset in deformation is not observed in krypton, reaches a maximum in yttrium and is less pronounced in niobium.

Figure (5.20) shows an overview over the whole region at $A \sim 100$. The niobium charge radii systematic agree with the general trend that has been observed in the region and fills the gap between the chains of zirconium and molybdenum. Niobium is the last element that displays the sudden onset of deformation before it smooths out in molybdenum. Unfortunately no molybdenum quadrupole moments are available yet. Figure (5.20) also shows that it is difficult to infer from the odd-even staggering which of the ^{102}Nb spin assignments is the most likely: $N = 61$ was measured for rubidium, however $N = 62$ is missing for comparison. $N = 61$ is missing on strontium and it is present in yttrium, however without clarity whether an isomer was observed. Under the assumption that the ground state was measured, the odd-odd isotope is smaller than its neighbours. Quite contrarily, the $N = 61$ isotope in molybdenum is bigger than its neighbours. In niobium, only the $I = 3$ assignment gives an odd-even staggering that follows yttrium, $I = 4$ and 5 would follow the trend of molybdenum.

In his paper on shape trends, Luo [76] points out that niobium is situated in a transitional region from axially symmetric shapes in yttrium to nearly maximally

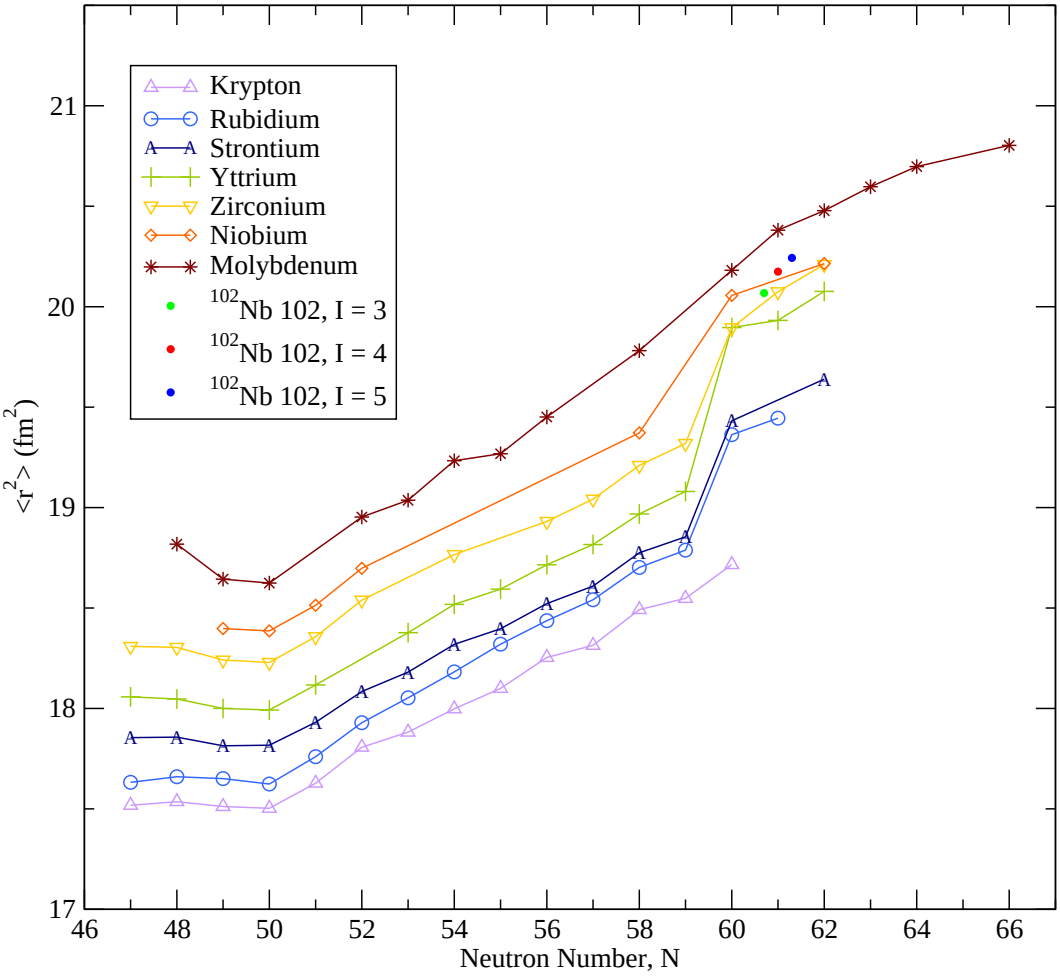

Figure 5.20: The absolute charge radii of krypton [67], rubidium [3], strontium [4], yttrium [56], zirconium [7], niobium and molybdenum [10] are plotted against their neutron number. The neutron deficient charge radii are taken from [11].

triaxial shapes in rhodium. Laser spectroscopy as a technique is not sensitive to the signatures of triaxiality. However, it might be that the difference in the static and the full deformation parameter, which is usually ascribed to nuclear softness, may have contributions from triaxiality that are not possible to trace with the employed method.

5.7.2 Nuclear Magnetic Moments

Single particle estimates of magnetic moments were calculated for the isotopes ^{93}Nb, ^{99}Nb, ^{101}Nb, ^{102}Nb and ^{103}Nb using equation (2.9). For all odd-A nuclei in table (5.10) the even number of neutrons does not contribute to the estimated magnetic moment and the Schmidt estimate is based on the spherical shell model for a single proton in the $1g^{+}_{9/2}$ configuration.

Table 5.10: The experimentally measured magnetic dipole moments and the Schmidt estimates with spherical shell model configuration

Mass A	Neutrons N	Spin I^{π}	μ_{exp} (μ_N)	$\mu_{SingPart}$ (μ_N)	configuration
90	49	8^+	$+4.964(5)^a$	$+4.338^a$	$\pi g9/2^+ \otimes \nu g9/2^+$
90m	49	4^-	$-0.019(4)^a$	-1.659^a	$\pi p1/2^- \otimes \nu g9/2^+$
91	50	$9/2^+$	$+6.526(5)^a$	$+6.793^a$	$\pi g9/2^+$
91m	50	$1/2^-$	$-0.102(1)^a$	-0.264^a	$\pi p1/2^-$
92	51	7^+	$+5.135(4)^a$	$+4.880^a$	$\pi g9/2^+ \otimes \nu g5/2^+$
93	52	$9/2^+$	$+6.1705(3)^b$	$+6.973^a$	$\pi g9/2^+$
99	58	$9/2^+$	+6.01(6)	+6.973	$\pi g9/2^+$
101	60	$5/2^+$	+3.19(3)	+6.973	$\pi g9/2^+$
102	61	(3)	+2.858(7)	+2.554	$\pi[422]5/2 \otimes \nu[411]3/2$
102	61	(4)	+2.957(7)	+2.918	$\pi[422]5/2 \otimes \nu[411]3/2$
102	61	(5)	+3.022(7)	+2.641	$\pi[422]5/2 \otimes \nu[532]5/2$
103	62	$5/2^+$	+3.13(3)	+6.973	$\pi g9/2^+$

[a] Baczynska [11] [b] Table of Nuclides [60]

For ^{102}Nb, $I = 3$ and $I = 4$, the estimated moments are based on the experimentally obtained magnetic moment for ^{103}Nb ($g_p = 1.2764(8)$) [422]5/2 and for ^{101}Zr ($g_n = -0.1813(7)$) [411]3/2 [7]. For ^{102}Nb($I = 5$) the estimate is based on ^{103}Nb and

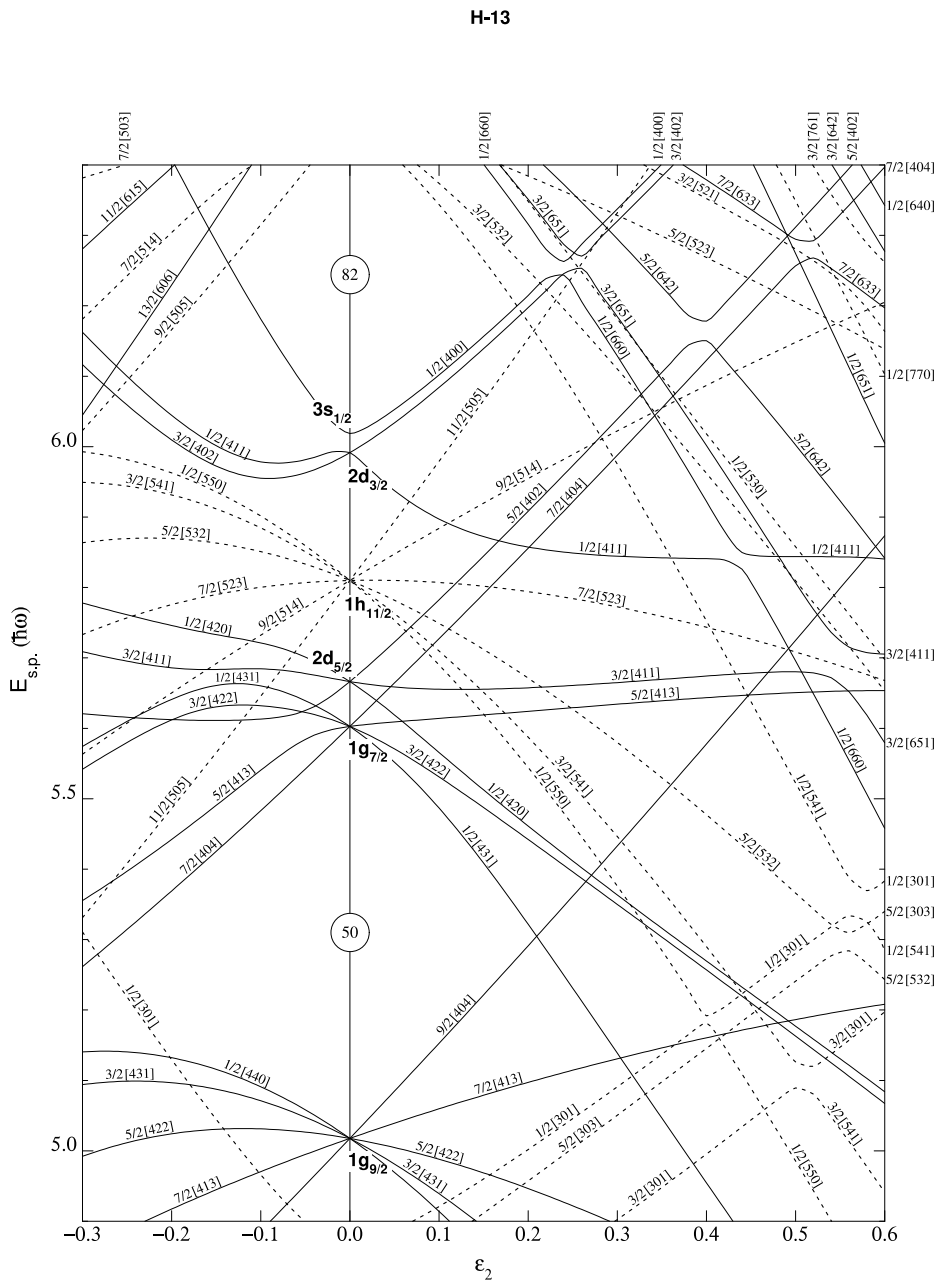

Figure 5.21: Nilsson diagram for protons, $50 \leq Z \leq 82$ [34]. The shells below $1g_{9/2}$ are with descending energy $2p_{1/2}$, $2p_{3/2}$ and $1f_{5/2}$ [32] or $2p_{1/2}$, $1f_{5/2}$ and $2p_{3/2}$ [65].

^{105}Mo [10] ($g_n = -0.220(8)$) which corresponds to a configuration [532]5/2 for the single neutron. Values for $N \leq 52$ were taken from Baczynska [11]. The single particle estimates are compared to the experimentally measured values. For ^{93}Nb, the magnetic moment can be modelled well by the spherical shell model. The same is true for ^{99}Nb. This behaviour agrees with the observed behaviour of the charge radii (see section 5.7.1). The result is also in agreement with the observed deformation parameters that suggest that the nuclear deformation can be ascribed to a very soft spherical nucleus that is vibrating about its equilibrium shape. For ^{101}Nb and ^{103}Nb there is a large discrepancy between the estimated magnetic moment for a single particle and the experimentally obtained value. This, together with the spin change, indicates that the nucleus is no longer spherical but deformed and that the nucleons move together to give a collective moment. This is in agreement with the extracted deformation parameters of $\langle\beta_2\rangle = 0.317(25)$ and $\langle\beta_2\rangle = 0.324(22)$ for ^{101}Nb and ^{103}Nb respectively. These indicate that the nuclei are strongly prolate deformed. The Nilsson diagram for protons (figure (5.21)) suggests the occupation of the 5/2[422] - level for $Z = 41$ in the vicinity of $\epsilon_2 = 0.3$ where $\epsilon_2 \sim 0.944\beta_2 - 0.122\beta_2^2$ [77]. This is in agreement with the $I = 5/2$ spin assignment for both ^{101}Nb and ^{103}Nb, obtained from the hyperfine structure fitting. The result is also in agreement with the results for ^{99}Y and ^{101}Y ($Z = 39$) [56]. Both yttrium isotopes have assigned spin $I = 5/2$ with deformation parameters $\langle\beta_2\rangle = 0.41(4)$ and $\langle\beta_2\rangle = 0.40(4)$ respectively. This is larger than the niobium deformation, allowing for a crossing of the 3/2[301] - level in the Nilsson diagram. Due to equation (2.6) we expect the magnetic moment to be orbital dependent. The very similar magnetic moment of all four isotopes $\mu(^{99}\text{Y}) = +3.18(2)\mu_N$, $\mu(^{101}\text{Y}) = +3.22(2)\mu_N$, $\mu(^{101}\text{Nb}) = +3.19(3)\mu_N$, $\mu(^{103}\text{Nb}) = +3.13(3)\mu_N$, is a further indication that the single proton occupies the same Nilsson level.

The experimentally obtained values for the ^{102}Nb magnetic moments are slightly

bigger than the Schmidt estimates that are obtained from neighbouring isotopes. However, they are in good agreement with these Schmidt values and seem consistent with the assumed configurations. The $I = 4$ magnetic moment of $\mu = +2.957(7)\mu_N$ is in remarkable agreement with the estimated value of $\mu = +2.918\ \mu_N$.

5.7.3 2n-separation energies

The obtained results can be compared to the two neutron separation energies that were measured by Hager *et al* for the A $\sim$ 100 region [2]. Neutron separation energies are very sensitive to the shell structure of nuclei, including pairing effects and spin-orbit coupling. The two neutron separation energy S_{2n} is defined as

$$S_{2n}(Z,N) = [m(Z,N-2) + 2m_n - m(Z,N)]c^2 \tag{5.12}$$

The two neutron separation energy is used to trace changes in the nuclear structure as it removes the pairing effect of nuclei. A stable nuclear structure leads to a smooth behaviour of S_{2n} when plotted against neutron number. The S_{2n}-energy decreases as more neutrons are added, indicating that neutrons are more loosely bound as the nuclei are more distant from the valley of stability.

In her paper, Hager [2] had already compared her results with the charge radii systematics of strontium, yttrium and zirconium. She found that the sudden increase in the charge radii of zirconium and yttrium corresponds to an increase in the respective S_{2n}-energies at $N = 60$ (see also [78]) (figure (5.22). This sudden change in the S_{2n}-energies confirms that the nuclei experience a local increase in stability as the neutrons are more tightly bound and the nuclei minimise their energy by settling into the deformed state . The S_{2n}-energy systematics smooths out again as the deformation is then carried forward to higher neutron numbers. The increase in S_{2n}-energy is present in niobium although less pronounced than in zirconium and

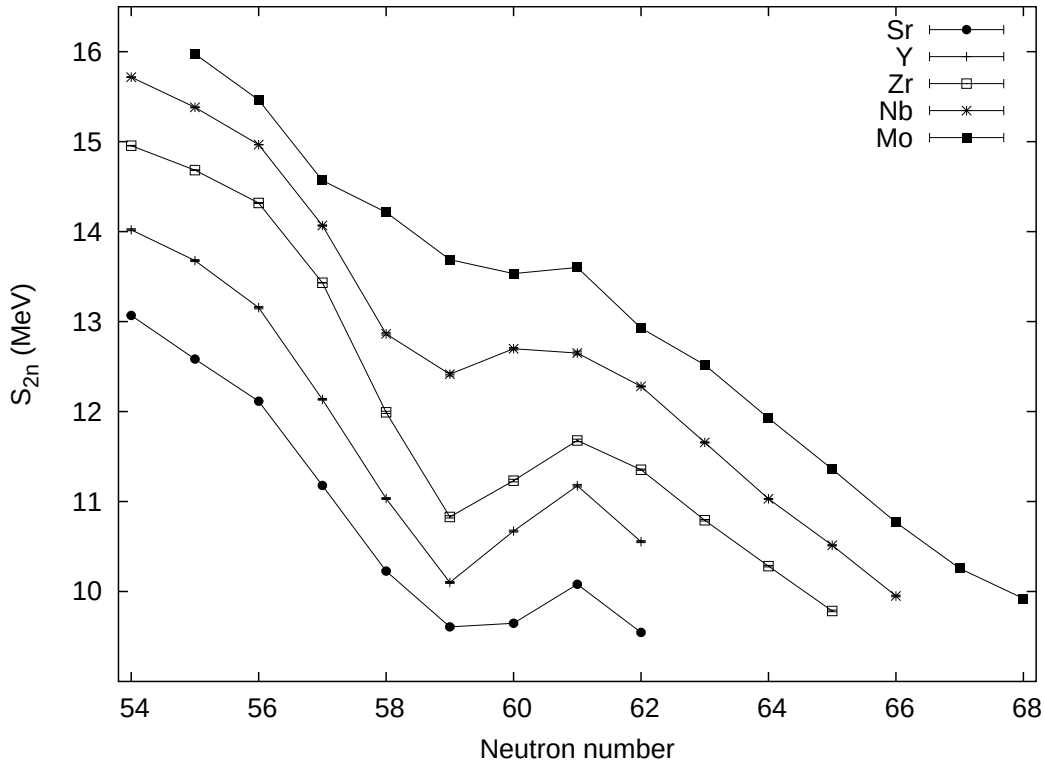

Figure 5.22: The 2-neutron-separation energies of strontium, yttrium, zirconium, niobium and molybdenum [2]

yttrium. This observation is in agreement with the findings that the onset of $\delta\langle r^2\rangle$ is less pronounced in niobium than in yttrium and zirconium indicating that the deformed shape loses its favourability in terms of energy minimisation as compared to the spherical structure at $N \leq 59$.

5.7.4 The nature of the shape change at $N = 60$

One important feature of the midshell regions is that unlike in doubly magic or singly-magic nuclei, both protons and neutrons possess valence nucleons in partly filled shells. Federman and Pittel [79] suggested that a strong interaction between valence neutrons and valence protons is the driving factor that leads to deformation in midshell nuclei. This idea was supported by Casten [80]. He explains that a p-n interaction in partly filled shells shifts the proton and neutron single-particle energies. This modifies the valence space for the protons and neutrons and leads to the evolution or even dispapearance of subshell gaps as the respective orbitals are filled. The $Z = 38, 40$ subshell, for example, is thought to be the stabilising factor for the spherical ground state nuclei at $N \leq 59$. As N approaches 60, the filling of the $\nu g_{7/2}$ orbital leads to the dispapearance of the $Z = 38, 40$ subshell gap and drives the deformation at $N \geq 60$ as the protons are now able to contribute to the collectivity.

Lhersonneau *et al* [81] provided evidence that another factor responsible for the onset of deformation at $N = 60$ is the down sloping of the $h_{11/2}$ [550]1/2 and [541]3/2 Nilsson states in that region. According to mean-field calculations, orbits with low K bend downwards on the prolate side of the Nilsson diagram (see figure (2.5) for definition of K). Lhersonneau et al [81] suggest that the occupancy of these intruder states allows the nuclei to transit into an energetically more favourable deformed shape.

In an attempt to come to an integrated approach, Verma, Dar and Devi [82] re-

evaluated the wave-functions and the limitations of earlier calculations for $^{98-102}$Sr and $^{100-104}$Zr. In their approach they use a projected shell model which provided good agreement in the rare earth region. Based on their calculation of occupation probabilities for neutron and proton shells in the zirconium region, they suggest that an interplay of different deformation driving factors were responsible for the strong onset of deformation in the Sr and Zr isotopes. These are the simultaneous occupation of low K components of the $1h_{11/2}$ and $2f_{7/2}$ neutron orbits (the latter originating from above the $N = 82$ major shell gap); the sharp increase in the $g_{9/2}$ proton occupation as one goes from ^{96}Sr to ^{98}Sr and from ^{98}Zr to ^{100}Zr; and the fact that $2d_{5/2}$ and $1g_{7/2}$ neutron subshells are less than half full. Hence the partly filled shells interact by the p-n interaction. An additional contribution is named as the polarization of the lower lying $2p_{1/2}$, $2p_{3/2}$ and $1f_{5/2}$ proton orbits [82]. Polarization of lower lying orbits is caused by valence protons that exert a non-spherically symmetric effect by orbiting around the inert "core" of filled shells.

Chapter 6

CONCLUSIONS AND FUTURE WORK

The A $\sim$ 100 region has been of longstanding interest to nuclear structure physicists, as this midshell region displays a sudden onset of deformation that cannot be explained by the single particle shell model.

Experimental data on the nature of the onset was supplied by studies of the excited states of the nuclei [83], B(E2; $2_1^+ \rightarrow 0_1^+$) transition rates [5], and by investigation of their neutron separation energies and mass measurements [2]. Laser spectroscopy provides valuable information on the change of the mean square charge radii and gives nuclear structure information through the magnetic dipole moment and the electric quadrupole moment. Laser spectroscopic measurements of rubidium [3], strontium [4], zirconium [6] and yttrium [56] have been presented and the niobium data presented in this thesis fills the gap between zirconium ($Z = 40$) and molybdenum ($Z = 42$) around the onset of deformation. As shown by Charlwood [10], a sudden onset of deformation cannot be demonstrated in molybdenum charge radii and is not expected in higher Z elements. Instead the sudden shape change is centred around yttrium ($Z = 39$) which displays the largest $\langle\beta_2\rangle$ values for $N \geq 60$ in this region. Niobium is the last element to show a sudden onset of deformation before the onset becomes very gradual in molybdenum. The molybdenum chain displays substantial differences from the trend of the $\delta\langle r^2\rangle$ even between $N = 50$ and $N = 60$. Despite missing information on the quadrupole moments of molybdenum,

it can be assumed that the mechanism that stabilises the near spherical ground states in the $Z \leq 41$ elements is no longer present in molybdenum, although it is still present in niobium. Molybdenum still shows large $\langle\beta_2^2\rangle$ values for $N \geq 60$ and it could be that the onset in collectivity that is observed in the $A \sim 100$ region is still present in molybdenum, but it develops a lot more gradually. The findings in niobium would fit well into such a picture with the observed decrease in the rate of change of deformation from $N = 58$ to $N = 60$ and the tendency towards soft nuclei in the ground states of ^{101}Nb and ^{103}Nb as opposed to the very rigid nature of the correspond isotopes in yttrium. As Luo *et al* [76] point out, niobium is also found to be at a transitional point for an onset in triaxiality which is oberved in $Z > 41$.

Spectra on ^{99}Nb, ^{101}Nb, ^{102}Nb and ^{103}Nb were obtained and evaluated for this thesis. It was possible to confirm the the spin assignnments for ^{99}Nb, ^{101}Nb and ^{103}Nb as $I = 9/2$, $I = 5/2$ and $I = 5/2$ respectively. The extracted information on $\delta\langle r^2\rangle$, μ and Q confirms a shape change of nuclei at $N = 60$ from soft and oblate (for $N < 60$) to more rigid and strongly prolate shape (for $N > 60$). The deformation is thought to be driven by a strong proton-neutron interaction as well as the strongly downward sloping $h_{11/2}[550]1/2$ component of the $\nu h_{11/2}$ Nilsson state. A prolate-oblate shape coexistence is suggested by microscopic-macroscopic calculations [32] of potential energy surfaces in even-even nuclei in that region.

The evaluation of the present data proved difficult due to the in parts very poor quality of the spectra. The poor quality was due to low production rates of the relevant isotopes and the limitations of the high voltage supply in the light collection region during the experiment. Care has been taken during the evaluation to substantiate the spectra through statistical analysis. The calibration of the electronic parameters, the field and the mass factors, was necessary to extract $\delta\langle r^2\rangle$, however this was challenging. A pre-experimental calibration on stable isotopes was impossible due to the lack of available stable isotopes. Hence, the calibration was carried

out using neighbouring elements including a statistical investigation of the underlying assumptions. By fitting the hyperfine structure it was possible to confirm the $I = 5/2$ spin assignment for both ^{101}Nb and ^{103}Nb and preliminary spin assignments of $I = (3), (4)$ or (5) for ^{102}Nb including the respective possible magnetic moments and quadrupole moments were obtained. The extracted nuclear parameters were interpreted within the droplet model and the Nilsson model.

The present data would not have been obtained without the help of a new experimental method which was optical pumping in the cooler. Through the introduction of a high powered and frequency broadened laser beam into the ion beam cooler at JYFL, it was possible to manipulate the electronic population of the low lying atomic states. The successful application of this method made it possible to extend the range of transitions suitable to spectroscopy. Ground state transitions which are usually used for spectroscopy are not available in niobium or proved to have very poor efficiency. Optical pumping in the cooler allowed spectroscopy from a low-lying metastable state. The new technique was used for the first time to confirm the spin in ^{100}Y and to obtain data on the neutron-deficient side of ^{93}Nb [11] and can now be used to extend the range of elements available for investigation at JYFL.

Potentially there is more work to be done on the neutron-rich niobium isotopes. The measurement of ^{100}Nb would allow a better understanding on the exact development of the shape transition at $N = 60$. An unambiguous determination of the ^{102}Nb spin assignment would allow a stronger conclusion on the underlying shell structure in that region. So far, many excited states in ^{102}Nb have only been assigned tentatively and knowledge of the ground state spin and parity would help understand the structure and excited states of this nucleus. There are possibilities for laser spectroscopy to obtain a better understanding of the ^{102}Nb ground state. Figure (5.15) in section 5.6 can now be used to obtain further peaks of the spectrum which would in turn improve the hyperfine structure analysis. Figure (5.15)

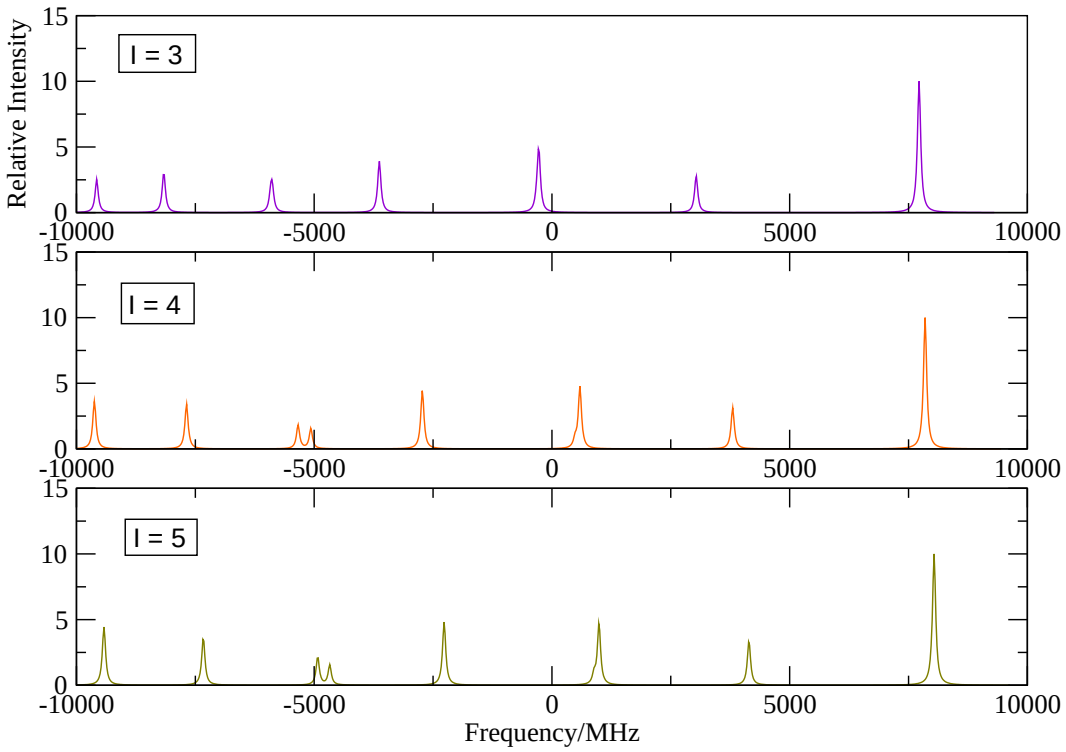

Figure 6.1: Prediction of the hyperfine structure in ^{102g}Nb for the transition at 322.5475 nm (2356.760 cm^{-1} 5s $^5F_1 \rightarrow$ 33351.000 cm^{-1} 5p $^5G^o_2$) for the spins I = 3, 4 and 5.

also shows that for all three possible spin assignments, the fitted spectra are very similar, so that it could be difficult to infer a definite spin assignment from this transition. Offline experiments (section 4.2) showed that another transition at 322.5475 nm (2356.760 cm^{-1} 5s $^5F_1 \rightarrow$ 33351.000 cm^{-1} 5p $^5G^o_2$) proved very efficient with 1 photon in 6750 ions when tried for optical pumping. Predictions for the ^{102}Nb hyperfine structure are shown in figure (6.1), with nuclear moments taken from table (5.8). If the whole structure of this transition was to be recorded in an experiment, the combination with the structure from the 290.82 nm transition should allow an unambigious assignment of the ^{102}Nb spin. One experimental difficulty is the mixture of ^{102}Nb with ^{102m}Nb components. Here, it could be tried to tag the ^{102}Nb ground state ions during the experiment by using a γ-detector at the end of the

ion-laser interaction region. A second possibility would be to increase the storage time of the ions in the ion beam cooler to decrease the fraction of 1.3 s ^{102m}Nb state. However, this is not feasible at the moment due to molecular formation in the ion beam cooler at long storage times. Under these circumstances it might be sufficient to scan the three most dominant peaks in the spectrum in figure (6.1) and investigate the relative distance between them. The same idea was used for the spin assignment of ^{100}Y where a measurement of two hyperfine structure peaks in a second transition was sufficient for an unambiguous spin assignment [11].

The re-investigation of the molybdenum chain would be of particular interest in the A $\sim$ 100 region. The data presented by Charlwood [10] was obtained using a $J = 1/2 \rightarrow J = 1/2$ atomic transition which was not sensitive to nuclear quadrupole moments. The application of optical pumping will allow the choice of transitions that allow the extraction of nuclear deformation data.

In summary, the development of the optical pumping technique opens up a whole new field of nuclear cases to be investigated that extend far beyond nuclei in the $N \sim 60$ region. For the niobium data, optical pumping proved crucial as a method to obtain nuclear structure information that allows us to deepen our understanding of this interesting region.

Appendix A

APPENDIX

A.1 Treating correlated errors

The errors on the gradients and intercepts obtained by plotting modified isotope shifts $\mu\delta\nu_i^{AA'}$ versus modified differential charge radii $\mu\delta\langle r^2\rangle_{Z'}^{AA'}$ of neighbouring elements are intrinsically correlated. Each of these King Plots (see section 5.4) are based on three data pairs $(\delta\langle r^2\rangle_{Z'}^{A_jA'},\ \delta\nu^{A_jA'})$, $j = 1..3$, with individual errors $(\sigma_{\delta\langle r^2\rangle_{Z'}^{A_jA'}},\ \sigma_{\delta\nu^{A_jA'}})$. The parameters F and $\mu_{ref}M_i$ that are calculated from the datapoints will have variances σ_F^2 and σ_M^2 respectively and are correlated by their covariance σ_{FM}^2.

Bevington [63] explains that the variance σ_F^2 of the field factor F can be defined as

$$\sigma_F^2 = \frac{1}{N}\sum_i (\bar{F} - F_i)^2 \tag{A.1}$$

where $\bar{F}$ is the mean of a distribution of individual F_i, $i = 1, .., N$. The variance σ_M^2 is similarly defined. The covariance σ_{FM}^2 is

$$\sigma_{FM}^2 = \frac{1}{N}\sum_i (\bar{F} - F_i)(\bar{M} - M_i) \tag{A.2}$$

When the variances σ_F^2, σ_M^2 and covariance σ_{FM}^2 are calculated, the individual

error $(\sigma_{\delta\langle r^2\rangle_{Z'}^{A_jA'}}, \sigma_{\delta\nu^{A_jA'}})$ on each data pair $(\delta\langle r^2\rangle_{Z'}^{A_jA'}, \delta\nu^{A_jA'})$ needs to be taken into account. This can be done by using a Monte Carlo simulation. In the Monte Carlo simulation, the measured experimental values $\delta\langle r^2\rangle_{Z'}^{A_jA'}$ and $\delta\nu^{A_jA'}$ are seen as the centroids of Gaussian distributions with standard deviations $\sigma_{\delta\langle r^2\rangle_{Z'}^{A_jA'}j}$ and $\sigma_{\delta\nu^{A_jA'}}$. The distribution is defined as [84]

$$G\left(\delta\langle r^2\rangle_{Z'k}^{A_jA'}|\delta\langle r^2\rangle_{Z'}^{A_jA'}, \sigma_{\delta\langle r^2\rangle_{Z'}^{A_jA'}}\right) = \frac{1}{\sigma_{\delta\langle r^2\rangle_{Z'}^{A_jA'}}\sqrt{2\pi}} \cdot \exp\left\{\frac{(\delta\langle r^2\rangle_{Z'k}^{A_jA'} - \delta\langle r^2\rangle_{Z'}^{A_jA'})^2}{2\sigma^2_{\delta\langle r^2\rangle_{Z'}^{A_jA'}}}\right\} \tag{A.3}$$

where $\delta\langle r^2\rangle_{Z'k}^{A_jA'}$ is the kth sample value drawn from the distribution G with mean $\delta\langle r^2\rangle_{Z'}^{A_jA'}$ and standard deviation $\sigma_{\delta\langle r^2\rangle_{Z'}^{A_jA'}}$. A similar distribution can be constructed for the isotope shifts $\delta\nu^{A_jA'}$.

For the King Plots of the elements krypton, rubidium, strontium and zirconium, these distributions were constructed and samples in form of random numbers were repeatedly drawn from these distributions. The sample data points were fitted by minimising χ^2 (see equation 5.9) and the gradient F and intercept $\mu_{ref}M$ were obtained for each sample data set. Figure (A.1) shows the distributions for the niobium $\mu\delta\nu^{AA'}$ versus zirconium $\mu\delta\langle r^2\rangle_{Z'}^{AA'}$ King plot. The obtained distributions allow calculation of the variances σ_F^2, σ_M^2 and the covariance σ_{FM}^2 from equations (A.1) and (A.2).

To obtain the error on the interpolation of the field factors and mass factors a generalized-least squares fit can be used [84]:

A set of four data points $(F_i,\ M_i)$, i = Kr, Rb, Sr, Zr, was obtained from Monte Carlo simulation with variances $\sigma_{F_i}^2$ and $\sigma_{M_i}^2$ and correlation $\sigma_{F_iM_i}^2$ between them. Two parameters $z_1 = \bar{F}$ and $z_2 = \bar{M}$ shall be found through interpolation. A Lagrange equation $\mathcal{L}$ in matrix form can be set up to solve the problem as one of a

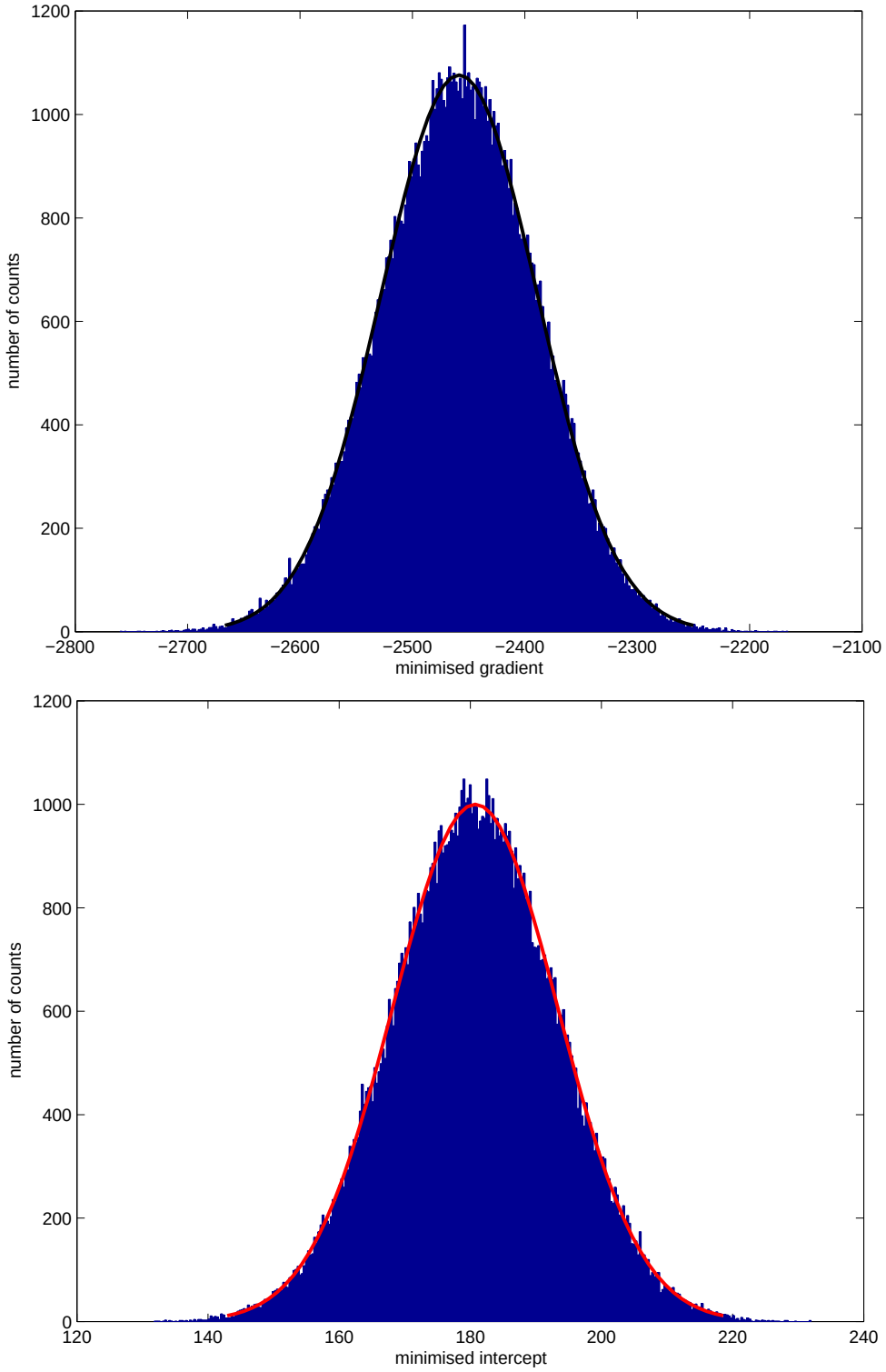

Figure A.1: The histograms of the Gaussian distributions for gradient and intercept of a King plot of modified niobium isotope shifts $\mu\delta\nu^{AA'}$ versus modified differential zirconium charge radii $\mu\delta\langle r^2\rangle_{Z'}^{AA'}$, obtained by Monte Carlo simulation. A normal distribution has been fitted to the distributions.

function with constraints [84]

$$\mathcal{L} = \frac{1}{2}\underline{v}\hat{\sigma}^{-1}\underline{v}^T + \mu\underline{G} \tag{A.4}$$

where $\underline{v}$ contains the residuals $\bar{F} - F_i$ and $\bar{M} - M_i$, $\hat{\sigma}$ contains the variances as diagonal elements and covariances as off-diagonal elements, μ contains the Lagrange multipliers and $\underline{G}$ contains a constraint for each datum point, namely $\bar{F} - F_i$ and $\bar{M} - M_i$. In the present case, the contraints are independent of the atomic numbers Z.

For an extremum point of $\mathcal{L}$ it is necessary that

$$\nabla_x\mathcal{L} = 0,\ \nabla_z\mathcal{L} = 0, \nabla_\mu\ \mathcal{L} = 0 \tag{A.5}$$

Here, ∇_i are gradients with respect to x, z and μ. By re-arranging it is possible to eliminate μ to get

$$(\nabla_z\underline{G})^T[(\nabla_x\underline{G})^T]^{-1}\hat{\sigma}^{-1}(-\underline{v}^T) = 0 \tag{A.6}$$

where $\bar{F}$ and $\bar{M}$ are the only unknowns. This equation can be solved analytically for both the correlated and the uncorrelated case. For the uncorrelated case one obtains the known expression for the weighted mean

$$\bar{F} = \frac{\sum \frac{F_i}{\sigma^2_{F_i}}}{\sum \frac{1}{\sigma^2_{F_i}}} \tag{A.7}$$

and similar for $\bar{M}$. For the correlated case

$$\begin{aligned}
\bar{F} &= \frac{(C_2 - C_4)[-C_3(-D_1) - D_3C_1] + C_3[(-D_1)(C_2 - C_4) - C_1(-D_2 + D_4)]}{C_1[-C_3(-D_1) - D_3C_1)} \\
\bar{M} &= \frac{(-D_1)(C_2 - C_4) - C_1(-D_2 + D_4)}{-C_3(-D_1) - D_3C_1}
\end{aligned} \tag{A.8}$$

Here,

$$
\begin{aligned}
C_1 &= \sum_i \frac{\sigma^2_{M_i}}{\sigma^2_{F_i}\sigma^2_{M_i} - (\sigma^2_{F_iM_i})^2} \\
C_2 &= \sum_i \frac{\sigma^2_{M_i}}{\sigma^2_{F_i}\sigma^2_{M_i} - (\sigma^2_{F_iM_i})^2} F_i \\
C_3 &= \sum_i \frac{\sigma^2_{F_iM_i}}{\sigma^2_{F_i}\sigma^2_{M_i} - (\sigma^2_{F_iM_i})^2} \\
C_4 &= \sum_i \frac{\sigma^2_{F_iM_i}}{\sigma^2_{F_i}\sigma^2_{M_i} - (\sigma^2_{F_iM_i})^2} M_i \\
D_1 &= C_3 \\
D_2 &= \sum_i \frac{\sigma^2_{F_iM_i}}{\sigma^2_{F_i}\sigma^2_{M_i} - (\sigma^2_{F_iM_i})^2} F_i \\
D_3 &= \sum_i \frac{\sigma^2_{F_i}}{\sigma^2_{F_i}\sigma^2_{M_i} - (\sigma^2_{F_iM_i})^2} \\
D_4 &\quad \sum_i \frac{\sigma^2_{F_i}}{\sigma^2_{F_i}\sigma^2_{M_i} - (\sigma^2_{F_iM_i})^2} M_i
\end{aligned}
\tag{A.9}
$$

and i = Kr, Rb, Sr, Zr.

References

[1] M Epherre *et al, Phys Rev C* **19**, 4 (1979)

[2] U Hager *et al, Nucl Phys A* **793**, 20 (2007)

[3] C Thibault *et al, Phys Rev C* **23**, 2720 (1981)

[4] F Buchinger, E B Ramsay *et al, Phys Rev C* **41**, 2883 (1990)

[5] H Mach *et al, Nucl Phys A* **523**, 197 (1991)

[6] P Campbell *et al, Phys Rev Lett* **89**, 082501 (2002)

[7] H Thayer *et al, J Phys G* **29**, 2247 (2003)

[8] B Cheal *et al, Phys Lett B* **645**, 133 (2007)

[9] R A Meyer *et al, Nucl Phys A* **439**, 510 (1985)

[10] F Charlwood *et al, Phys Lett B* **674**, 23 (2009)

[11] K A Baczynska, PhD Thesis, The University of Birmingham, 2009

[12] B Cheal *et al, Phys Rev Lett* **102**, 222501 (2009)

[13] K S Krane *Introductory Nuclear Physics*, John Wiley and Sons (1988)

[14] T Mayer-Kuckuk *Kernphysik* B.G. Teubner, Stuttgart (2002)

[15] R Eisberg, R Resnick *Quantum physics*, John Wiley & Sons, New York, 2nd Ed (1974)

[16] Th Schmidt *Z Phys* **106**, 358 (1937)

[17] A Corney *Atomic and Laser Spectoscopy*, Clarendon Press, Oxford (1977)

[18] A R Edmunds *Angular momentum in Quantum Mechanics* Princeton University Press, Princeton, New Jersey (1960)

[19] M L Bissell, PhD Thesis, University of Birmigham, 2007

[20] A Bohr and V F Weisskopf *Phys Rev* **77**, 94 (1950)

[21] F Bitter *Phys Rev* **75**, 1326 (1949)

[22] J Billowes, P Campbell, *J Phys G* **21**, 707 (1995)

[23] W H King *Isotope Shifts in Atomic Spectra*, Plenum, New York (1984)

[24] Z -C Yan, W Nörtershäuser and G W F Drake *Phys Rev Lett* **100**, 243002 (2008)

[25] D H Forest, PhD Thesis, University of Birmingham, 1999

[26] K Heilig and A Steudel *At Data Nucl Data Tables* **14**, 613 (1974)

[27] E W Otten *Nuclear radii and moments of unstable isotopes* in *Treatise on Heavy-Ion Science* D A Bromley, Editor. 517 (1989)

[28] E C Seltzer *Phys Rev* **188**, 1916 (1969)

[29] S A Blundell, P E G Baird, C W P Palmer, D N Stacey and G K Woodgate *J Phys B* **20**, 3663 (1987)

[30] G Fricke *et al, At Data Nucl Data Tables* **60**, 177 (1995)

[31] R C Barrett *Phys Lett B* **33**, 388 (1970)

[32] J Skalski, S Mizutori and W Nazarewicz, *Nucl Phys A* **617**, 282 (1997)

[33] S G Nilsson *Dan Mat -Fys Medd* **29**, 16 (1955)

[34] Ernest O. Lawrence Berkeley National Laboratory http://ie.lbl.gov/hspin.html

[35] H Stöcker *Taschenbuch der Physik*, Wissenschaftlicher Verlag Harri Deutsch 5. Auflage (2004)

[36] R Loudon, *The Quantum Theory of Light*, Oxford Science Publications, 2nd Ed (1983)

[37] W Demtröder *Experimentalphysik 3*, Springer (2004)

[38] H Haken and H C Wolf *Atomic- and Quantum Physics* Springer (1984)

[39] J Brossel, A Kastler and J Winter *J Phys Radium* **13** 668 (1952)

[40] E Hecht *Optics* Addison - Wesley (1974)

[41] J Äystö *Nucl Phys A* **693**, 477 (2001)

[42] A Nieminen *et al, Phys Rev Lett* **88**, 094801 (2002)

[43] R Moore *et al, Physics Letters B* **547**, 200 (2002)

[44] B Tordoff, PhD Thesis, University of Manchester, 2007

[45] https://www.jyu.fi/fysiikka/en/research/accelerator/igisol/separator.html, Latest update 20.1.2005, accessed 09.02.2010

[46] A Nieminen *Nucl Intrum Methods Phys Res A* **469**, 244 (2001)

[47] J Billows *Nucl Phys A* **682**, 206c (2001)

[48] Exciton Inc. - Laser Dyes *http://www.exciton.com/*

[49] *Model 380, Ring Dye Laser System, Preliminary Instruction Manual* Spectra Physics, Inc. (1978)

[50] H L Thayer, PhD Thesis, University of Birmingham, 2003

[51] S Gerstenkorn and P Luc *Atlas du Spectre d'Absorption de la molecule d'iodine 14800 - 20000* cm^{-1} (Editions du CNRS, Paris, 1978)

[52] I D Moore *et al, J Phys G* **31** 1499 (2005)

[53] C Rauth, Diplomarbeit, Johannes Gutenberg - Universität, Mainz, 2003

[54] R E Horn, Dissertation, Johannes Gutenberg - Universität, Mainz, 2003

[55] G Tungate, *private communication* The University of Birmingham

[56] M D Gardner, PhD Thesis, The University of Birmingham, 2006

[57] Kurucz Atomic Line Database *http://cfa-www.harvard.edu/amdata/ampdata/kurucz23/sekur.html*

[58] J R Boyce *Phys Rev C* **10**, 1 (1974)

[59] S Rinta-Antila *et al, Eur Phys J A* **31**, 1 (2007)

[60] Table of Nuclides *http://atom.kaeri.re.kr* Nuclear Data Evaluation Lab, Korea Atomic Energy Research Institute, 2000

[61] B Cheal, PhD Thesis, University of Birmingham, 2004

[62] G F Knoll *Radiation Detection and Measurement*, John Wiley, 3rd edition (2000)

[63] P R Bevington *Data reduction and error analysis for the physical science*, McGraw-Hill Book Company, New York (1969)

[64] H E White, A Y Eliason *Phys Rev* **44**, 753 (1933)

[65] J Eberth, R A Meyer and K Sistemich (Eds.) *Nuclear Structure of the Zirconium Region* Proceedings, Springer-Verlag Berlin Heidelberg (1988)

[66] W Fischer *et al, Z Phys A* **270**, 113 (1974)

[67] M Keim *et al, Nucl Phys A* **586**, 219 (1995)

[68] S Weisberg *Applied linear regression* Wiley, New York (1980)

[69] D D Bugg, M A Henderson, K Holden and P J Lund *Statistical Methods in the Social Sciences* North-Holland Publishing Co. Amsterdamm (1968)

[70] I Angeli *At Data Nucl Data Tables* **87**, 185 (2004)

[71] W D Myers and K-H Schmidt *Nucl Phys A* **410**, 61 (1983)

[72] W D Myers and W J Swiatecki *Annals of Physics* **84**, 186 (1974)

[73] D Berdichevsky and F Tondeur *Z Phys A* **322**, 141 (1985)

[74] H Ahrens *Phys Rev C* **14**, 211 (1976)

[75] G Audi, O Bersillon, J Blachot and A H Wapstra, *Nucl Phys A* **729**, 3 (2003)

[76] X Y Luo *et al, J Phys G* **31** 1303 (2005)

[77] S Åberg, H Flocard, W Nazarevicz *Ann Rev Nucl Part Sci* **40** 439 (1990)

[78] S Rinta-Antila *et al, Phys Rev C* **70**, 011301(R), (2004)

[79] P Federman, S Pittel *Phys Lett B* **69**, 385 (1977)

[80] R F Casten *Nuclear structure from a simple perspective*, Oxford University Press (1990)

[81] G Lhersonneau *et al, Phys Rev C* **49**, 3 (1994)

[82] S Verma, P A Dar, R Devi *Phys Rev C* **77**, 024308 (2008)

[83] E Cheifetz, R C Jared, S G Thompson and J B Wilhelmy *Phys Rev Lett* **25**, 1 (1970)

[84] S L Marshall, J G Blencoe *Am J Phys* **73**, 69 (2005)